

Politecnico di Torino



Corso di Laurea Magistrale in Ingegneria Meccanica

Tesi di Laurea Magistrale

Stretch bend limit strain of AA5182-O and AA7075-T6 aluminum alloys under warm temperature conditions

Relatore: Prof. Graziano Ubertalli

Correlatori: Prof. Giovanni Belingardi

Prof. Michael Worswick

Candidato: Davide Francesconi

A.A. 2019/2020

Contents

1	Introduction	1
1.1	Lightweighting	1
1.2	Formability of aluminum sheet	2
1.2.1	Aluminum wrought alloys designation	4
1.2.2	Forming limit diagrams	5
1.2.3	Warm forming	6
1.2.4	Stretch-bending	8
2	Objectives of this thesis	11
3	Literature review	13
3.1	Work hardening in aluminum alloys	13
3.1.1	Strain hardening model	16
3.1.2	Temperature and strain rate effect	18
3.2	Plastic instability and necking	19
3.2.1	Necking detection	21
3.3	Variables controlling formability	25
3.3.1	Temperature	26
3.3.2	Punch radius	28
3.3.3	Materials	30
3.3.4	Temperature distribution	32
3.3.5	Anisotropy	33
3.3.6	Lubricants	33
3.3.7	Punch speed	34
3.3.8	Contact pressure	35

4	Experimental work	37
4.1	Experimental methods	37
4.1.1	Variables	38
4.1.2	Specimen	41
4.1.3	Test matrix	42
4.2	Experimental equipment	43
4.2.1	Existing instruments	43
4.2.2	Adapting tools	45
4.2.3	Digital Image Correlation	48
4.3	Thermal analysis	50
4.3.1	Thermal simulation	50
4.3.2	Validation and remarks	53
4.4	Applied necking detection methods	57
5	Results	63
5.1	Temperature effects on limit strains	63
5.2	Curvature effects on limit strains	67
5.3	Temperature and curvature effects on punch displacement.	72
6	Conclusions	81
	References	83
A	Punch holder drawing	91
B	Clamping plate drawing	93
C	MATLAB scripts	95

List of Figures

1.1	Temperature-dependent forming limit curves for aluminum AA7075-T6 alloy, 2 mm thickness.	7
3.1	Measured engineering stress-strain curves for a Al-Mg alloy (5000 series) at different temperatures and strain-rates. Adapted from van den Boogaard (2002)	19
3.2	Sample ISO 12004-2:2008 parabolic fitting process.	22
3.3	Time-dependent necking detection methodology suggested by Volk and Hora.	23
3.4	Time-dependent necking detection methodology suggested by Martínez-Donaire.	25
3.5	Stretch-bending strain distributions under different stretching conditions.	29
4.1	Cylindrical punches	40
4.2	Specimen shape and main dimensions.	42
4.3	Basic layout of the existing warm forming press.	44
4.4	Existing stretch-bending dies for RT tests.	45
4.5	Existing stretch-bending punch-holder.	45
4.6	Punch holder	46
4.7	Clamping plate.	47
4.8	Final approximate assembly	48
4.9	Thermal simulation: control volume and boundaries conditions.	50
4.10	Time-dependent boundaries and contacts involved in the clamping phase.	51

4.11	Main steps of the simulation for specimen target temperature 125°C (398 K)	53
4.12	Thermocouples welded to the specimen	53
4.13	Temperature time series of the specimen for 125 °C target tem- perature.	54
4.14	Temperature time series of the specimen for 175 °C target tem- perature.	55
4.15	Temperature time series of the specimen for 225 °C target tem- perature.	56
4.16	Area for major strain and curvature data extraction.	58
4.17	Outer surface curvature as a function of major strain for AA5182- O at RT	59
4.18	Illustration of outer surface curvature.	60
4.19	Example of curvature method analysis.	61
4.20	PLC effect of AA5182-O (punch radius 15 mm, RT).	62
4.21	Example of time-dependent method analysis.	62
5.1	Temperature effects on AA7075-T6 limit strains.	64
5.2	Outer surface curvature as a function of major strain of AA7075- T6 sheet at 175° C (15 mm punch)	65
5.3	Outer surface curvature as a function of major strain of AA7075- T6 sheet at 225° C (15 mm punch)	65
5.4	Temperature effects on AA5182-O limit strains.	66
5.5	Limit strains of AA5182-O, curvature effect	67
5.6	Limit strains of AA7075-T6, curvature effect	69
5.7	Curvature effect on strain paths	70
5.8	Equivalent limit strains of AA5182-O, equivalent strains	71
5.9	Equivalent limit strains of AA7075-T6, equivalent strains	72
5.10	Temperature and curvature effects on AA5182-O punch displace- ment.	73
5.11	Line-slices surface plot AA5182-O (RT, PR: 15)	74

5.12	Line-slices surface plot AA5182-O (175 °C, PR: 15)	75
5.13	Line-slices surface plot AA5182-O (RT, PR: 2)	75
5.14	Line-slices surface plot AA5182-O (175 °C, PR: 15)	76
5.15	AA5182-O: comparison of strain distributions plots RT vs. 175 °C (punch: 2 mm)	77
5.16	AA7075-T6: comparison of strain distributions plots RT vs. 175 °C (punch: 5 mm)	78
5.17	Temperature effects on AA7075-T6 punch displacement.	79
5.18	Line-slices surface plot AA7075-T6 (RT, PR: 15)	79
5.19	Line-slices surface plot AA7075-T6 (175 °C, PR: 5 mm)	79

List of Tables

1.1	General designations of wrought aluminum alloys.	4
4.1	Main mechanical properties of AA5182-O and AA7075-T6	39
4.2	Nominal composition of aluminum AA5182-O and AA7075-T6 alloys.	39
4.3	Test matrix of aluminum AA5182-O	42
4.4	Test matrix of aluminum AA7075-T6	42
4.5	Thermal setting of the heat cartridges.	57
4.6	Summary of heating times per each target temperature.	57

Abstract

In this thesis, warm stretch bend tests are proposed to investigate the combined effect of stretching and bending on forming limits of aluminum AA5182-O and 7075-T6 under warm temperature conditions. The performed test is in between a V-bend test (usually related to fracture forming limits) and a stretch dominant test, such as Marciniak (usually related to the onset of localized necking). It has been noted that, under hybrid deformation, the sheet metal failure may be preceded by localized necking (as in a Marciniak test), or it may not (as in a V-bend test). Thus, the limit strain is the strain state immediately preceding the first failure mechanism to appear. In the current investigation, only the temperature and curvature effects on limit strains are taken into account for both AA5182-O and AA7075-T6, and limit strains are computed using two necking detection methods: the curvature approach (DiCecco *et al.*, 2016) and the time-dependent approach (Volk and Hora, 2011).

Temperature is found to have positive effects on AA5182-O limit strains, whereas results for the AA7075-T6 lead to the conclusion that an optimum forming temperature exists between 175 °C and 225 °C. Curvature benefits in delaying the localized necking confirm previous results for the AA5182-O at room temperature (Cheong, 2019). However, the relationship between punch radius and limit strains is reversed at warm temperatures, and increasing the curvature impacts negatively on formability. As regards to the AA7075-T6, curvature appears beneficial at warm temperatures, but low punch displacements prevent from getting reliable results at room temperature. Finally, a close look at punch displacements shows a possible negative aspect of warm forming. As regards to the AA5182-O, punch displacement decrease by increasing the temperature. This phenomenon may be due to the decrease of strain hardening, which reduces the uniform elongation. In contrast, the punch displacement of AA7075-T6 increase increasing the temperature until 175 °C, probably because of the smaller reduction of n -value compared to the AA5182-O.

Acknowledgements

First, I would like to thank Professor Michael Worswick for giving me the chance of working in his labs and for his guidance during the fulfillment of this work. He taught me how to carry out a research and how to present my work as clearly as possible, adding great value to my academic background. Then, I would like to express my sincere appreciation to Sante DiCecco for sharing his experience on the topics covered in this thesis. Further on, I am grateful to the research group and the support staff at the University of Waterloo Crash and Forming Lab, especially to Professor Clifford Butcher for letting me use his dies and to Eckhard Budziarek for his patience and support during the experiments. Also, I would like to thank Professors Giovanni Belingardi and Graziano Ubertalli for their assistance from the Politecnico di Torino.

Acknowledgments would be incomplete without thanking my friends for their life-long support. A special shout out to Simone and Laurent, whom I always feel close no matter where I am in the world, and to Andrea for sharing ideas and experiences during the time we spent in Canada working on our thesis. Also, I would like to express my special thanks to my brother and sister, who offered invaluable support and suggestions over the years. Finally, but profoundly, I am incredibly grateful to my parents for teaching me the value of hard work, and for their sacrifices for educating and preparing me for my future.

Chapter 1

Introduction

1.1 Lightweighting

Lightweighting plays a fundamental role in achieving current and future CO_2 emission goals. In 2016 the transport sector contributed 30% of the EU's total CO_2 emissions, of which 72% comes from road transportation¹. To prevent greenhouse gas emissions, world governments are imposing increasingly strict emission targets. Looking at the car market in the EU, from 2000 to 2015, the average CO_2 emission for the NEDC (New European Driving Cycle) dropped from 170 g/km to 145 g/km . New car CO_2 emissions, on average, must be down 15% by 2025 and 37.5% by 2030, relative to a 2021 baseline. In other words, using the current 2021 target value of 95 g/km as baseline, the reduction would translate into a target value of 59 g/km by the end of the next decade (ICCT, 2019). In the short-term, mass reduction of vehicles can significantly improve fuel efficiency. It has been estimated that lightening of 100 kg on a VW Golf VI with a 90 kW TSI engine results in a reduction of tailpipe CO_2 emission of 8.4 g/km (EAA, 2013). In the longer-term, lightweighting can improve the efficiency and performance of transportation, whatever the technology of powertrains will be. Automakers are now focusing on several materials showing relevant lightweight potential, such as aluminum, magnesium, high strength steel (HSS), advanced high strength steel (AHSS) and polymers.

¹<https://www.eea.europa.eu/data-and-maps/indicators/transport-emissions-of-greenhouse-gases> [accessed: 18.09.2019]

Aluminum is a favorable option for efficient transportation, because of its high strength to weight ratio, corrosion resistance, weldability, excellent thermal and electrical conductivity and infinite recyclability (Kurukuri, 2010). The density of aluminum (2700 kg/m^3) is one-third of that of steel. However, this weight reduction is hardly achieved since the majority of components need to be enlarged to keep the same performances. For sheet metal components, the most typical ratio of thickness is 1.5, which means that a 0.8 mm mild steel component can be replaced by a 1.2 mm aluminum component. The relationship between the stiffness of a part and its weight can be influenced by its geometry and can be very complicated; nonetheless, the advantage of aluminum alloys is substantial (EAA, 2013).

For many years, automakers have used aluminum in manufacturing of castings to design, for instance, engine blocks, transmission housings and wheel rims. Furthermore, aluminum has been widely employed in engine cooling systems because of its thermal properties. However, limited progress has been made in term of Body-In-White (BIW) parts. Thus, the BIW represents an opportunity to achieve further weight reduction (Tisza and Czinege, 2018). The biggest obstacle to the more widespread use of aluminum in BIW parts is its lower formability compared to traditional steel alloys under room temperature conditions. This behavior is usually caused by the high alloy percentages that are required for high strength (Novotny and Geiger, 2003). To expand the usage of aluminum in the automotive sector and enable complex shape forming, the sheet forming can be carried out at warm temperatures, typically in the range $150 \text{ }^\circ\text{C}$ - $300 \text{ }^\circ\text{C}$ depending on the alloy. The study of forming limits of aluminum alloys under plastic deformation at warm temperature conditions is the subject of this thesis.

1.2 Formability of aluminum sheet

The most popular sheet metal forming processes are bending, deep drawing, and stretching. In sheet metal forming, forces are applied to a metal blank to

modify its shape rather than remove any material. To perform this operation and fix the final geometry, the metal needs to be plastically deformed and, therefore, the metal needs to be stressed beyond its yield strength but without causing failure.

The formability of aluminum sheets is lower than steel under room temperature conditions. However, formability, referred to as “the ease with which a material can be formed while satisfying quality requirements” (Scallan, 2003), can be a broad term. Thus formability is not a unique and intrinsic property of the material, but it is affected by several material characteristics and process factors, and low formability can emerge in form of several defects. For example, the Young’s modulus of aluminum is about one-third of steel, which results in a greater tendency to exhibit wrinkling and springback defects. Furthermore, the elongation of aluminum is about one half of steel and its strain formability is about two-thirds of mild steel. These properties make aluminum more challenging to use in body part design since the maximum achievable strain in one process step is less than that for mild steel for the same strain path (Kurukuri, 2010). When the limit strain is reached, local necking and fractures appear. In this work, formability is referred to as the ability to resist localized necking and fracture.

Nakazima *et al.* (1968) and Marciniak and Kuczyński (1967) tests are two standardized and well-known experiments to measure the limit strains of sheet metals rigorously. The results of both tests are plotted on the Forming Limit Diagram (FLD). However, FLDs produced by the Marciniak and Nakazima methods are significantly different. These differences are mainly due to the sheet curvature, contact pressure and frictional condition during the specimen deformation (Min *et al.*, 2016). Over the years, in addition to the standard Marciniak and Nakazima tests, several experiments involving different punch shapes and forming parameters have been designed to investigate specific phenomena related to sheet metal forming. Among them, bending under tension tests have been carried out to find out the relationship between sheet curvature and formability. In addition to studying the effect of sheet curvature,

warm forming tests have been carried out to study the increase in formability of aluminum at elevated temperature. There exists a lack of published literature on stretch bending tests at high temperatures. Consequently, this thesis, the effects of temperature and punch curvature are considered jointly in bending under tension tests under warm temperature conditions.

1.2.1 Aluminum wrought alloys designation

Wrought aluminum alloys are divided into families according to a four-digit system introduced in the '50s. The first digit defines the major alloy class according to the main alloying element. The second digit defines a variation from the original alloy (0 is always the original composition, 1 is the first variation, and so forth). The third and fourth digits define a specific alloy within the series. For example, the AA7075 aluminum alloy refers to a specific alloy, which belongs to the 7000 series (main alloy element zinc). The original AA7075 alloys can be modified to increase fracture toughness by varying the iron and silicon amounts. These variations from the AA7075 alloy, for example, are identified as AA7175 and AA7475.

Table 1.1: General designations of wrought aluminum alloys. Adapted from (MacKenzie, 2016a)

Designation	Principal alloying	description
1000	unalloyed ($\geq 99.00\%$ <i>Al</i>)	Work hardening strengthening
2000	Copper	Heat treatable alloy
3000	Manganese	Solid-solution strengthening
4000	Silicon	Solid-solution strengthening (<i>Al-Si</i>) Heat treatable(<i>Al-Si-Mg</i>)
5000	Magnesium	Solid-solution strengthening
6000	Magnesium/Silicon	Heat treatable alloy
7000	Zinc/Magnesium	Heat treatable alloy
8000	Miscellaneous	Work hardening strengthening and Solid-solution strengthening

1.2.2 Forming limit diagrams

The Forming Limit Diagram (FLD), initially proposed by Keeler (1978) and Goodwin (1969), is used traditionally to describe sheet metal formability. In this plot, the vertical axis and horizontal axis correspond to the major and minor strain respectively. At any instant, during a forming process, the in-plane strain components at each location on the blank can be represented by a point on the FLD. Each data point can be identified as unnecked (safe forming), necked (critical) or fractured (fail). The line drawn between the safe forming zone and the critical forming zone is called Forming Limit Curve (FLC). The line that lies between the failure and the critical forming zone is termed the Fracture Forming Limit Curve (FFLC). The FLD is commonly determined by two methods: one is the out-of-plane method represented by Nakazima *et al.* (1968) the other is the in-plane method represented by Marciniak and Kuczyński (1967).

The Marciniak method involves stretching rectangular sheet metal specimens over a cylindrical flat-head punch (101.6 mm diameter). A carrier blank, with a central hole cut out, is placed between the specimen and the punch in order to ensure the maximum plastic deformation occurs in the central flat area of the specimen, avoiding friction effects. The Nakazima test uses a hemispherical (101.6 mm diameter) punch and does not need the blank carrier, which results in more complicated strains because of curvature and friction effects. To plot FLDs, different strain conditions are investigated by varying metal strip sizes or the interface lubricant. Traditionally, the different strain conditions are identified by the strain ratio ϵ_2/ϵ_1 . Negative strain ratios are in the left-hand region of the diagram (known as drawing region). The leftmost end of the FLC is the pure shear condition ($\epsilon_2/\epsilon_1 = -1/2$), and little interest is given to lower ratios because of the strong wrinkling trend under these strain states. The vertical axes ($\epsilon_2/\epsilon_1 = 0$) represents plane strain state, which is important since they are the weakest forming condition. Finally, the right-hand side of the diagram is known as stretching region of the FLD, and the rightmost end of the FLC corresponds to the equi-biaxial strain state ($\epsilon_2/\epsilon_1 = 1$).

According to the ISO 12004-2: 2008 standard, FLCs are plotted under linear strain path conditions ($b = d\epsilon_1/d\epsilon_2 = \text{constant}$), which result in straight lines of different slope starting from the origin on FLDs. This means that the ratio between the major and minor strain is kept constant throughout the entire load cycle. So, for example, to obtain the limit strain for plane strain conditions, the strain path on the FLD will be a vertical straight segment starting at the origin and ending in the ordinate where the onset of necking occurs. However, it has been noted that the deviation from linear strain paths can have a significant influence on the shape of FLCs. Nakazima noted this phenomenon in 1968, but the strain path effect first received significant attention when automotive manufacturers begin to apply simulations and FLDs to predict forming limits in sheet metal forming. Graf and Hosford (1993) investigated the effect of strain path by applying pre-straining to AA6111-T4 aluminum alloy. Different levels of pre-straining were applied in the uniaxial and biaxial strain directions and then specimens were tested to subsequently construct FLCs. The results demonstrated that the effect of non-linear strain paths should not be neglected.

1.2.3 Warm forming

The most widely used aluminum alloys in automotive sheet components are the medium strength 5000 (Al-Mg) and 6000 (Al-Mg-Si) series. They both exhibit excellent weight-saving capacity. However, their formability under room temperature conditions is lower than mild steels. Furthermore, the 5000 series alloys are affected by the dynamic strain aging effect, which causes stretcher strains and it degrades the surface quality. For this reason, 5000-series alloys are typically used for the inner panels, and 6000-series alloys are used for the outer panels Bolt *et al.* (2001).

7000-series alloys are already used in the aircraft industry due to their high strength-to-density ratio, but they still have seen only limited application in the automobile industry. Their high specific strength and high bend stiffness make this family of alloy an attractive alternative to steel components when high strength is required to meet crash safety standards, such as in A-pillar,

B-pillar and side-impact beam components. The greatest obstacle of more widespread use of 7000-series alloys in automotive application is their low formability at room temperature, which makes them competitive only in hot and warm forming.

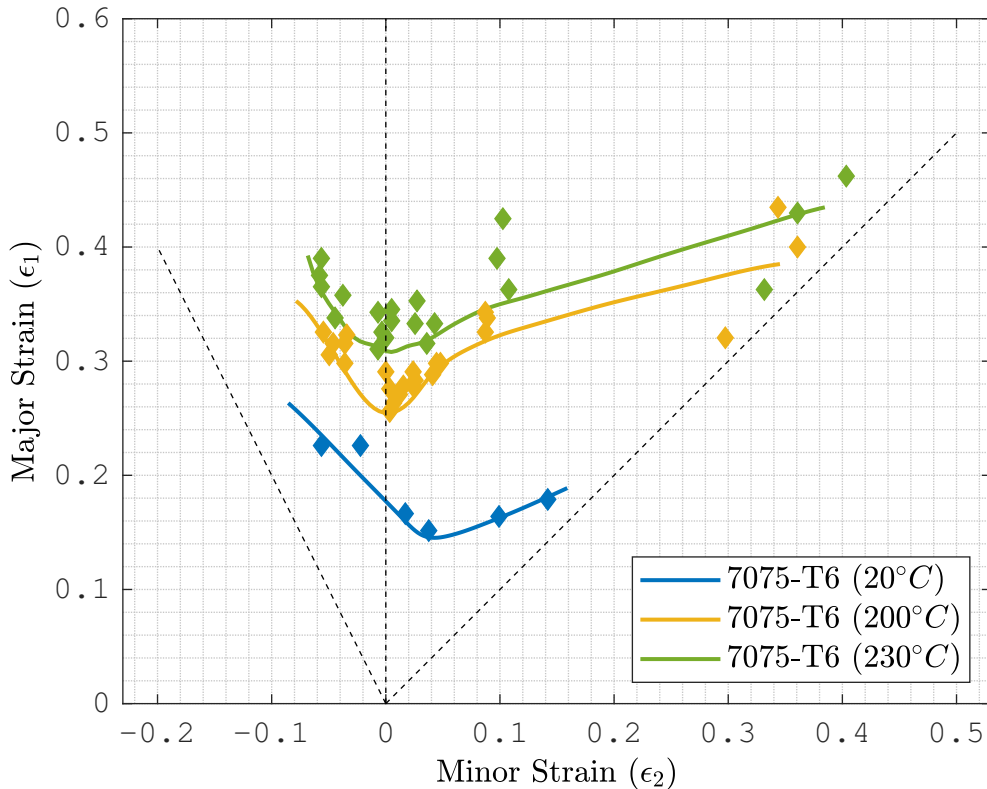


Figure 1.1: Temperature-dependent forming limit curves for aluminum AA7075-T6 alloy, 2 mm thickness. Adapted from Sotirov *et al.* (2012).

Warm forming consists of heating the aluminum blank to temperature above room temperature and below the recrystallization temperature. Bolt *et al.* (2001) performed drawing tests on AA5754-O and AA6016-T4 aluminum alloys over the temperature range of 100 °C to 250 °C. Bolt’s experiments show a significant increase in product height at elevated temperatures, but AA5754-O and AA6016-T4 display two separate behaviors. As regards the former, the maximum increase in product height is more pronounced (almost 60% at 250 °C), but the effect of temperature is only noticeable over 175 °C. For the 6016-T4, the effect of temperature is already significant at 175 °C, but the maximum

product height only increases by 30%. Hardness tests were carried out at the same time to investigate the effect of temperature on mechanical properties and warm forming was found to not have a substantial effect on the final product hardness for both alloys. In 2012, the warm formability of AA7075-T6 sheet was investigated by Hui *et al.* (2012) and Sotirov *et al.* (2012) (temperature-dependent FLD in Fig. 1.1). Both studies found a significant increase in sheet drawability at high temperatures. Specifically, in Hui's experiment, Limiting Draw Ratio (LDR) of AA7075-T6 increases from 1.6 (room temperature) to 2.0 at 180 °C and then slightly decreases to 1.9 at 260 °C. However, in his experiment the increase in LDR was combined with a significant loss of strength for temperatures over 220 °C. Furthermore, studies by Takata (2013) showed that the best results are achieved by selective and localized heating strategies, which cause a non-homogeneous temperature distribution on the blank. Finally, an extra benefit of warm forming is the enhancement of surface quality in 5000 series, since at high temperature stretcher lines no longer appear Kurukuri (2010).

1.2.4 Stretch-bending

Conventional sheet metal deformation processes usually involve both stretching and bending simultaneously, which generate non-homogeneous strain states across the sheet thickness and complex strain paths. The combined effect of bending and stretching significantly influences the onset of necking and the mechanism of failure: it shifts and changes the FLC shape (Martínez-Donaire *et al.*, 2014).

Localized necking and the ductile fracture (without noticeable necking) are the most common failure mechanisms in sheet metal forming. The experimental evidence firstly described by Hecker (1972) and Charpentier (1975) shows that bending has a beneficial effect on the FLC in delaying the onset of local necking. Therefore, FLCs plotted under stretch bending conditions lie substantially above those obtained under uniform in-plane stretching conditions. At the University of Waterloo, stretch bending tests of aluminum AA5182-O alloy were

recently carried out by Cheong (2019) under room temperature conditions. In this investigation, the combination of stretching and bending results in a non-linear strain path, hence results were adjusted accordingly to the linearization method by Min *et al.* (2016). The corrected results showed a positive correlation between the bend severity (thickness over punch radius ratio) and the material formability. Thus, limit strains do not only depend on material properties but also on geometrical factors such as punch curvature, and stretch-bending tests can provide a more accurate characterization of the relationship between punch curvature and formability.

Chapter 2

Objectives of this thesis

Warm temperatures enhance limit strains, and consequently, they expand the scope of aluminum sheet metal forming. These benefits have long been known, but they are still not exploited fully. On one hand, this can be attributed to the increased complexity and cost of production. On the other hand, difficulties exist in understanding the mechanisms of formability and objectively defining limit strains. In other words, although warm forming benefits are clear, it is not as clear how to quantify them. This is crucial to properly design the sheet forming process and to avoid overestimation or underestimation of the strain capability of the metal blank.

Furthermore, the stretching strain component is usually combined with the bending strain component in sheet metal forming. This combination results in complex strain distribution through the sheet thickness that cannot be obtained by standard tests such as the Marciniak test. In this study, changes in the punch radius are introduced in order to control the strain gradients through-thickness and to achieve intermediate strain conditions between a V-bend test (ductile fracture failure) and a standard Marciniak test (localized necking failure). The following objectives are set to pursue the aims of the thesis indicated above:

- Designing an experiment able to produce strain gradients through-thickness at the sample failure for different desired temperatures.
- Designing the required tools.
- Performing a thermal simulation to analyze the temperature gradients

of the dies and the sample surface. Then, selecting appropriate control spots for continuous temperature monitoring during the experiment.

- Implementing a MATLAB script based on two necking detection methods to determine limit strains from the data extracted by Digital Image Correlation (DIC).
- Assessing of temperature and curvature effects on limit strains and punch displacement.

Chapter 3

Literature review

This chapter highlights previous research in the fields of warm forming and stretch-bending of aluminum alloys. The results are sorted by the variables which affect the formability, as defined in Section 1.2. For each variable, a short analysis of previous researches is given. The analysis focus is to display the effect of each variable on formability in order to assist the choice of experimental variables (and their values) in Chapter 3. Section 3.2 deepens the meaning of limit strain, which is the aim of this work. However, there is not a single standard to define the limit strain of materials, and formability involves many aspects of material characteristics and process parameters. Hence, some fundamentals of work hardening and plastic instability must be examined first (Section 3.1). Then, the main methods for localized necking detection must be discussed (Section 3.2.1). Many variables control the formability of aluminum sheets (Section 3.3). Although the investigation of all variables that affect formability is beyond the scope of this thesis, knowing their impact on limit strains allows for a better design of the experiment and discussion of the results.

3.1 Work hardening in aluminum alloys

Work hardening plays a fundamental role in sheet metal forming since it highly affects the plastic deformation behavior of polycrystalline materials. Plastic deformation of a metallic microstructure usually is accomplished through the motion and production of dislocations and their interaction is the main factor

responsible for the work hardening phenomenon. Dislocations on the same plane interact with each other by generating stress fields that can impede dislocation motion by repulsive (equal Burgers vector direction) or attractive (opposite Burger vector direction) forces. As plastic strain accumulates, the total length of dislocations per unit volume of crystal increases and leads to dislocation tangles, which oppose dislocation motion. Dislocation propagation can also be affected by grain boundaries. The dislocation density within a grain determines the degree of difficulty for dislocations to traverse grain boundaries and move from one grain to the next one. Thus, changing the grain size can influence the yield strength.

Work hardening is further increased by second phase and solid solution strengthening. These two strengthening mechanisms divide aluminum wrought alloys into separate categories i.e., non-heat-treatable and heat-treatable alloys. Since the present investigation involves both AA5182-O and AA7075-T6 alloys, which belong to non-heat-treatable and heat-treatable categories, respectively, second phase and solid solution strengthening mechanisms are each discussed briefly. The basis for the wrought non-heat-treatable 5000-series is the aluminum-magnesium system. The addition of magnesium provides solid-solution strengthening and slight decreases in ductility and elongation. This alloying element leads to an elastic distortion in the alloy matrix, which inhibits the motion of dislocations and improves the strength. Increasing magnesium content significantly increases the yield and ultimate tensile strengths because of its large atomic size and low weight. However, there is a limit to the amount of solute that can be dissolved. Looking at the phase diagram, magnesium can be dissolved up to 17 *wt%* in solid solution, but in aluminum 5000-series alloys its quantity does not usually exceed 5.5 *wt%*. In fact, during the cold working process, high amounts of magnesium facilitate the precipitation of Mg_2Al_3 , which accumulates at grain-boundaries and it produces susceptibility to stress corrosion cracking. This problem can be partially solved by lowering the amount of magnesium and adding manganese to aluminum-magnesium alloys. Manganese promotes the precipitation of magnesium phases and ensures

a greater level of corrosion stability by keeping the same mechanical performances (MacKenzie, 2016b).

The heat-treatable 7000-series is characterized by alloying with zinc. Zinc confers little solid-solution strengthening to aluminum, although the addition of magnesium and/or copper to the aluminum-zinc alloy, results in attractive compositions for heat-treating and age hardening. Precipitation hardening consists of changes in solid solubility with temperature to produce clusters of solute atoms that impede dislocation motion in the aluminum matrix. Firstly, the alloy temperature is raised into the single-phase region so that all of the precipitates dissolve. Then, the alloy is rapidly quenched to produce a supersaturated solid solution and to trap excess vacancies which can later act as nucleation sites for precipitation. The precipitates can form slowly at room temperature (natural aging) or faster at warm temperatures (artificial aging). Not all alloys in which this phenomenon can be developed will be hardened by it. The solute atoms have to be collected into clusters that have the same crystal structure of the solvent matrix, which means solute clusters have to be coherent to the solvent matrix to increase the alloy strength (Banhart, 2016). As regards Al-Zn-Mg systems, immediately after quenching, spherical GP (Guinier–Preston) zones are formed. Within a day of natural aging, the high concentration of zinc in these zones helps the diffusion of magnesium through vacancies to form GP clusters with average zinc to magnesium ratio of 1:4. Continuing the aging process, the metastable transition precipitate η' appears, and finally, the equilibrium η phase is formed. The sequence of precipitates can be summed up as following (Banhart, 2016):



The GP zones are coherent, η' clusters are semicoherent and η phase incoherent. These steps assume that each metastable product generates nuclei for the subsequent phase. However, there is a strong interdependence between quenching, aging, and the resulting metallurgical microstructure of precipitates. For example, it has been observed that both η' and η phases can appear during

quenching. In particular, η nucleates at grain boundaries, whereas η' nucleates and grows on dislocations. Furthermore, high quench rates produce a fine dispersion of GP zones, and so a more uniform distribution of η' phases is obtained during aging. At aging temperature up to 100 °C both GP zones and η' clusters can be observed. The apparent solvus temperature for the formation of GP zones is approximately 135 °C, so above 130 °C up to 150 °C, GP zones rapidly dissolve to produce η' , which appears to be the first precipitate. The anomalous increase in resistivity is no longer observed, but even after a long aging period (i.e. 700 h), the effects on the strain of η' phase are still visible. The η equilibrium phase eventually forms from η' clusters, and the alloys performances decrease (MacKenzie, 2016b). The addition of more than 1 wt% of copper creates a subcategory of the Al-Zn-Mg system, that have special characteristics. Copper dissolves in the precipitates in modifying their composition and stabilizing the η' phase, resulting in an increased over-aging resistance (the AA7075 alloy belongs to this group) (Banhart, 2016).

3.1.1 Strain hardening model

From a mechanical point of view, the micromechanisms of plastic deformation lead to increased resistance to further deformation. In sheet metal forming, it is essential to quantify the stress-strain relationship in the form of flow stress (σ_f) in order to capture the material plastic behavior and to simulate the forming processes. Numerous methods exist to define flow stress in literature. These approaches can be separated into two main categories: the phenomenological models and physically-based models. Phenomenological models fit experimental results using non-physical parameters. For this reason, their application is limited to the range of fitting values. Physically-based models, such as Bergström model (Bergström, 1983) are based on physical considerations, so they can be used to predict the plastic behavior over a wider range of data than the phenomenological models. For the purpose of this study, the phenomenological models were judged sufficient due to their greater ease of use.

The most widely used phenomenological model is the Nadai model, also known

as power-law:

$$\sigma_f = C\epsilon^n \quad (3.1)$$

where σ_f is the flow stress, ϵ is the true strain, n the strain hardening coefficient (n -value) and C a material coefficient. The Nadai model (van den Boogaard *et al.*, 2001) is derived from the one-dimensional tensile test, but can still be used in two-dimensional deformations by introducing the equivalent strain. However, this model only considers the effects of strain hardening. Therefore, the model has to be extended to take into account temperature and strain rate, which have a significant influence on flow stress in aluminum warm forming processes. The strain rate sensitivity of flow stress is often described by the parameter m , which is defined as the slope in a $\log\sigma$ - $\log\dot{\epsilon}$ plot. The combination of the definition of strain rate sensitivity and the Nadai work hardening function results in:

$$\sigma_f = C(\epsilon + \epsilon_0)^n \left(\frac{\dot{\epsilon}}{\dot{\epsilon}_0} \right)^m \quad (3.2)$$

where $\dot{\epsilon}_0$ is a reference strain rate.

This equation is further extended to describe the combined effect of temperature and strain rate. The most common quantitative approach to temperature dependence is the Zener-Hollomon parameter (van den Boogaard *et al.*, 2001):

$$Z = \dot{\epsilon} \exp\left(\frac{U}{kT}\right) \quad (3.3)$$

where U is the related activation energy for a deformation process, such as cross slip and dislocation climb, k is the Boltzmann's constant, and T is the absolute temperature (measured in Kelvin).

By substituting the strain rate ($\dot{\epsilon}$) in 3.2 with Zener-Hollomon parameter (Z) in 3.3, both temperature and strain rate are taken into account. The applicability of this model is still limited, since n , m , and C are temperature dependent. The more advanced Nadai model (Eq. 3.4), known as the extended Nadai model (van den Boogaard *et al.*, 2001), is obtained by defining $n(T)$, $m(T)$, and $C(T)$ as a function of temperature. It is important to notice that this model is still completely phenomenological.

$$\sigma_f = C(T)(\epsilon + \epsilon_0)^{n(T)} \left(\frac{Z}{\dot{\epsilon}_0} \right)^{m(T)} \quad (3.4)$$

3.1.2 Temperature and strain rate effect

Temperature and strain have a significant effect on work hardening, and as a consequence, on formability. This section discusses the temperature and strain rate effects on work hardening. The implications of these effects on formability are reviewed in Section 3.3.

Temperature and strain rate generally have opposite effects on flow stress. Increasing the temperature increases the total elongation, and it decreases the strength coefficient C and the strain hardening coefficient n . By contrast, increasing the strain rate decreases the total elongation and increases both C and n values. The former has a low impact on forming limits. The latter is closely related to uniform elongation (as shown in Section 3.3.1) and plays a key role in the fracture resistance of metals (Gupta *et al.*, 2015). Increasing the temperature is beneficial in order to increase the total elongation and the strain rate sensitivity coefficient m . In particular, the m -parameter reaches a minimum at room temperature and can be negative for some alloys (5000-series). Negative values of this parameter lead to unstable flow stresses and dynamic strain aging. This phenomenon can be physically explained for 5000-series alloys by considering the interaction between the dislocations and the solute atoms of Mg . At low strain rate, solute atoms can migrate to dislocations in the interstices generated by the distorted lattice and stop further the dislocation movement. Instead, when dislocations move faster, solute atoms cannot catch up with dislocations, and lower flow stresses appear (van den Boogaard, 2002). Macroscopically, dynamic strain aging leads to the inverse relationship between strain rate and flow stress (accordingly to negative strain rate sensitivity). Since this phenomenon is related to the Mg amount, it is less significant in the 7000-series alloys (slightly positive m at RT).

Fig. 3.1 displays these effects on stress-strain curves from uniaxial tensile tests on Al-Mg alloys by van den Boogaard *et al.* (2001). At room temperature, negative strain-rate sensitivity generates serrated stress flows. In the temperature range between RT and 100 °C, stress-strain curves are strain-rate independent, and the uniform elongation nearly corresponds to the ultimate

strain because of the low value of m . Over $100\text{ }^{\circ}\text{C}$ the strain-rate dependence is more pronounced, and the decrease in uniform elongation is more than offset by the increase in post uniform elongation. These results are in accordance with the investigations reviewed in Section 3.3.1.

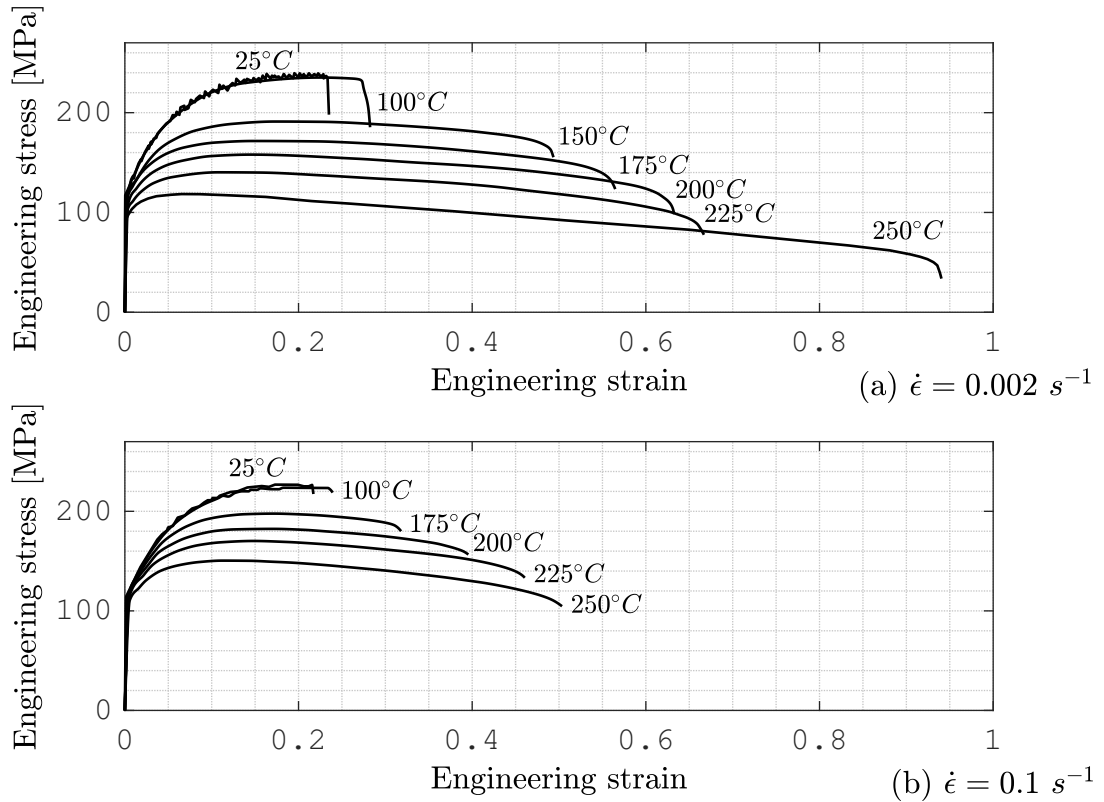


Figure 3.1: Measured engineering stress-strain curves for a Al-Mg alloy (5000 series) at different temperatures and strain-rates. Adapted from van den Boogaard (2002)

3.2 Plastic instability and necking

In sheet metal forming processes, the onset of necking instead of fracture is usually regarded as the limit strain criterion since once localized necking occurs, the deformation process becomes unstable. For simplicity, a generic uniaxial tensile test is considered. At low strains, uniform deformation occurs along the full gage section. If all specimen sections are equivalent, uniform extension results. If by chance, any region deformed more than the rest of the specimen,

increased strength by work hardening makes this anomalous deformation stop, until the rest of the specimen reaches an equivalent strain. This process results in a stable and uniform deformation. However, when the increase in stress due to the decrease in cross-sectional area becomes greater than the increase in load-carrying ability of the metal due to strain hardening, all deformation focuses within the necked section. Thus, deformation becomes unstable and the localized deformation rapidly evolves to fracture in the necked section. Numerous attempts to predict limit strains starting from physical and material considerations can be found in the literature. Some of these methods, properly calibrated, are currently used in FLD plotting in order to limit the number of test runs required to get FLCs.

In 1885, Considère defined the criterion for the onset of localized necking in tensile tests based on strain hardening. In his analysis, the instability occurs at the peak load. If the strain hardening behavior follows the Nadai model, then the limit strain coincides with the strain hardening coefficient.

$$F = \sigma A \quad (3.5)$$

When the peak load is reached, $dF = 0$, so

$$dF = \sigma dA + Ad\sigma = 0 \quad (3.6)$$

Rearranging and considering the assumption of volume conservation in plastic deformation, Eq. 3.6 gives

$$\frac{d\sigma}{\sigma} = -\frac{dA}{A} = d\epsilon \implies \frac{d\sigma}{d\epsilon} = \sigma \quad (3.7)$$

Finally, the strain at peak load ($\epsilon = n$) is obtained by replacing the Eq. 3.1 (Nadai) in Eq. 3.7. However, this result is only valid in uniaxial tension state. For this reason, it has little applicability in the investigation of limit strains in sheet metal forming due to the wide range of strain paths encountered.

Swift (1952) provides a general criterion for localized necking in thin sheets under plane stress states. Hill showed that localized necking develops in the direction of zero-elongation. Thus the strain component perpendicular

to the necking direction is only due to sheet thinning. Hill's theory is in good accordance with the experimental results in the drawing region of FLD (the left-hand part), but his equation leads to a meaningless solution in the biaxial stretching region of FLD (right-hand part). To solve this inconsistency, Marciniak and Kuczyński (1967) develop a localized necking prediction theory known as the MK model. This model is able to predict the onset of localized necking in the biaxial stretching region based on the introduction of a pre-defined inhomogeneity in the metal sheet. Usually, the defect is a small reduction in the initial thickness, but the model has been improved over the years to include other types of inhomogeneity in the material properties. A numerical algorithm can be implemented based on this theory to predict the onset of necking when the strain rate within the defect exceeds the strain rate within the surrounding homogeneous regions by a factor, usually set to 10. This makes MK analysis a powerful tool to obtain FLDs. However, MK models require previous knowledge of the experimental forming limit diagram to calibrate the imperfection parameters. Once the model is calibrated, it can be used to investigate other loading conditions, such as higher temperatures.

3.2.1 Necking detection

Principal strain pairs on the FLC need to be detected just before the onset of necking. In the original work of Keeler (1978), the surface discontinuity (neck) was detected by touch and the correspondent principal strain limit values were measured using a circle-grid printed on the specimen surface. The advent of Digital Image Correlation (DIC) enabled the standardization of necking detection, but it is worth emphasizing the importance of this operation. In the DIC method, the deformation is recorded as a series of images in a video recording, selecting a later (or earlier) frame, and using the strain level detected in that frame, would result in a higher (or lower) strain limits. This variation would result in underestimating (or overestimating) the onset of necking for a given sheet deformation, so it is crucial to choose the proper image corresponding to the onset of necking. The ISO 12004-2:2008 standard is commonly

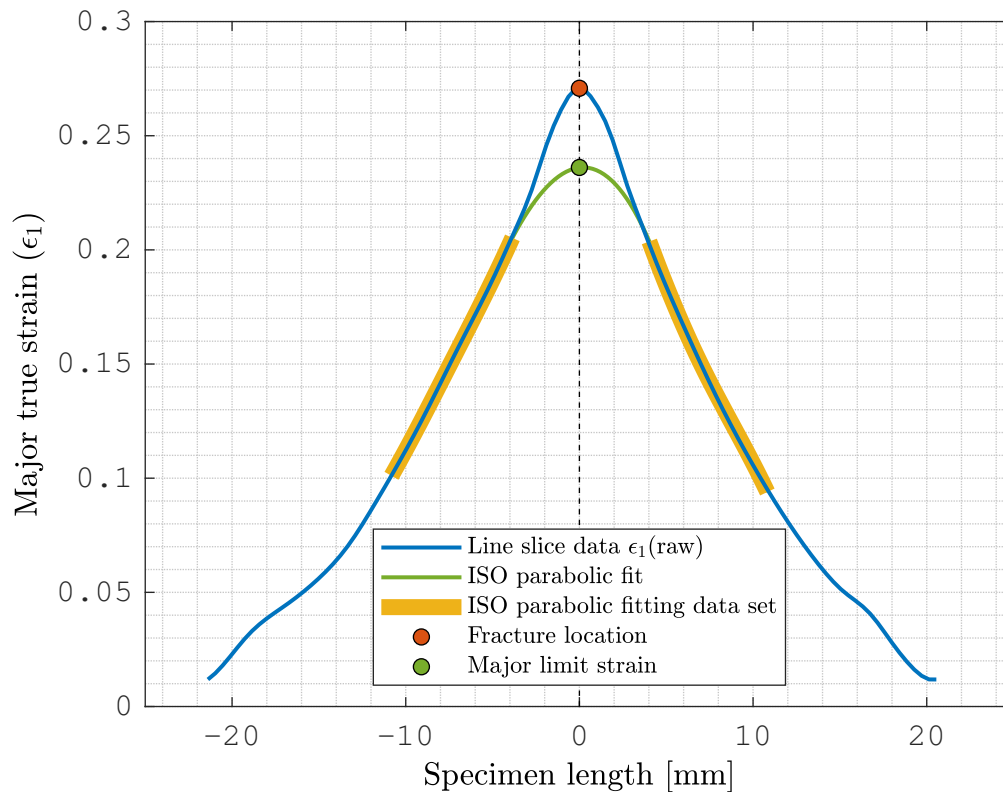


Figure 3.2: Sample ISO 12004-2:2008 parabolic fitting process. Adapted from DiCecco *et al.* (2016).

used in industry to generate FLCs. According to the standard, the strain test can be carried out using either Nakazima or Marciniak punches. Once fracture is detected, the test is stopped. The strain distribution along the line perpendicular to the fracture is measured (line slice data). A parabolic reconstruction is performed, ignoring the strain measurements directly adjacent to either side of the specimen crack. The limit strain is defined by the strain level read from the parabolic fitting curve corresponding to the crack location (Fig. 3.2). The procedure has to be repeated twice to define both the minor and major limit strains.

Despite the importance of ISO 12004-2:2008 standard in FLC generation, the method shows some limitations when there are significant strain gradients across the sheet thickness (Martínez-Donaire *et al.*, 2014). In an investigation on aluminum stretch bending tests, Martínez-Donaire *et al.* (2014) showed that

the limit strain resulting from the ISO method is affected greatly by dispersion, likely due to the size of the data window used to fit the parabola according to the standard. Consequently, new approaches have been developed to perform the strain limit detection of sheet metal.

Volk and Hora (2011) developed a local time-dependent method based on the temporal analysis of the strain rate through the sheet thickness (ϵ_3). The method computes the time derivative of strain ϵ_3 located in the failure region. Two straight lines are obtained by interpolation of data recorded at the early stages and at the late stages of the test, corresponding to the stable and unstable phases of deformation, respectively. Since an increased thinning rate is expected in the necking region, the straight lines intersect in a point (red point in Fig. 3.3). The authors state that the intersection of the straight lines well represents

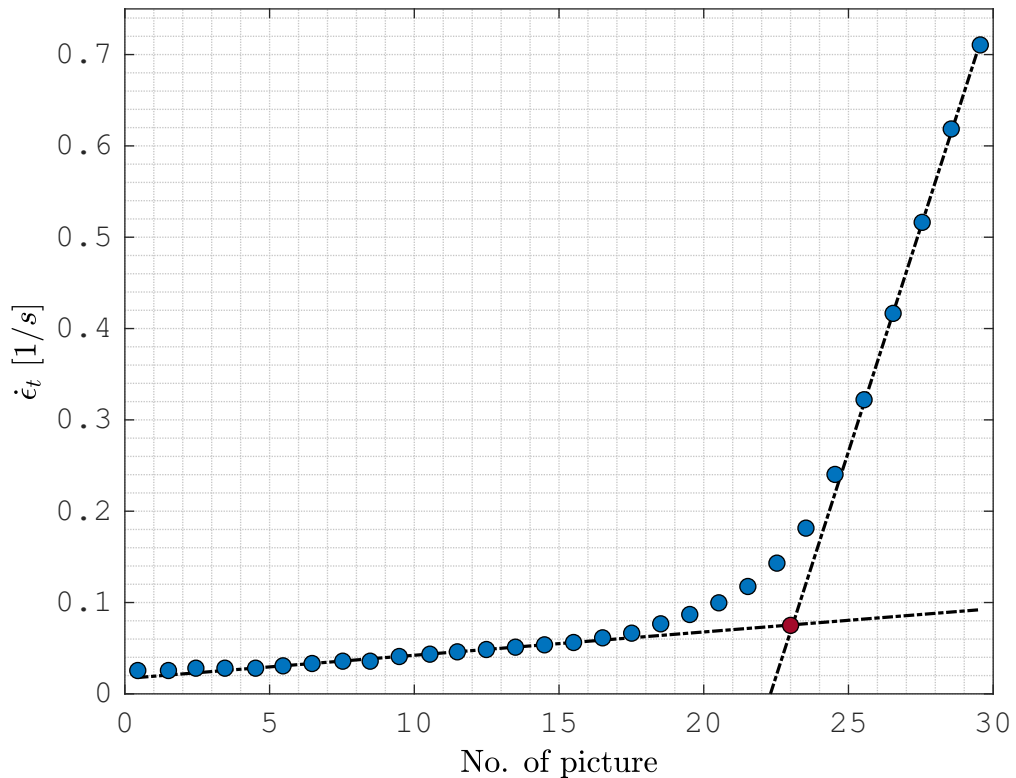


Figure 3.3: Time-dependent necking detection methodology suggested by Volk and Hora. The number of picture refers to DIC image from the experimental observation. With these results, necking occurs at 22nd image. Adapted from Volk and Hora (2011).

the time at which the onset of necking (acceleration of strain) occurs. Thus the maximum strains from the DIC image just prior to this time are taken as the safe strains. The investigation considered two steel sheet alloys, HC220YD and C260LAD, and the results from this method were found in accordance with measurements acquired using circle-analysis techniques. This methodology has been used in other papers under both room temperature and warm forming conditions (Leotoing *et al.*, 2013). The benefits of this methodology are its simplicity, the ease of its implementation in a DIC analysis. Despite the results being quite sensitive to the number of images considered in the unstable phase, the method is relatively user-independent (DiCecco *et al.*, 2016).

Martínez-Donaire *et al.* (2014) proposed a “strain rate unloading approach” for necking detection, herein referred to as the MD method. This method is based on the observation that the rate of principal strains located in the necking region increases monotonously, whereas outside the localized region, the strain rates should begin to decrease when instability occurs. This is quite logical considering the strain behavior in the unstable phase of deformation after the onset of necking. To perform the MD analysis, the time-evolution of principal strains (ϵ_1 and ϵ_2) is calculated at location of interest. These rates are computed from the changes in strain between successive DIC images.

As shown in Fig. 3.4, the decreasing strain rate at the boundary of the neck indicates that the forming limit has been reached. The MD analysis was implemented to investigate the limit strain of aluminum AA5182-O and dual-phase steel alloys and the results were in accordance with the safe strains found using the ISO standard. Furthermore, the MD analysis is attractive since it is performed on the strain distribution along the same line used in the ISO method, i.e., along the line perpendicular to fracture axis. Thus it requires no additional DIC processing with respect to the ISO standard.

The sheet curvature approach is based on a local variation in curvature associated with the onset of necking (DiCecco *et al.*, 2016). The change in curvature is computed from stereoscopic DIC measurement on the outer surface of the specimen. At the beginning of deformation, the surface of the specimen is flat

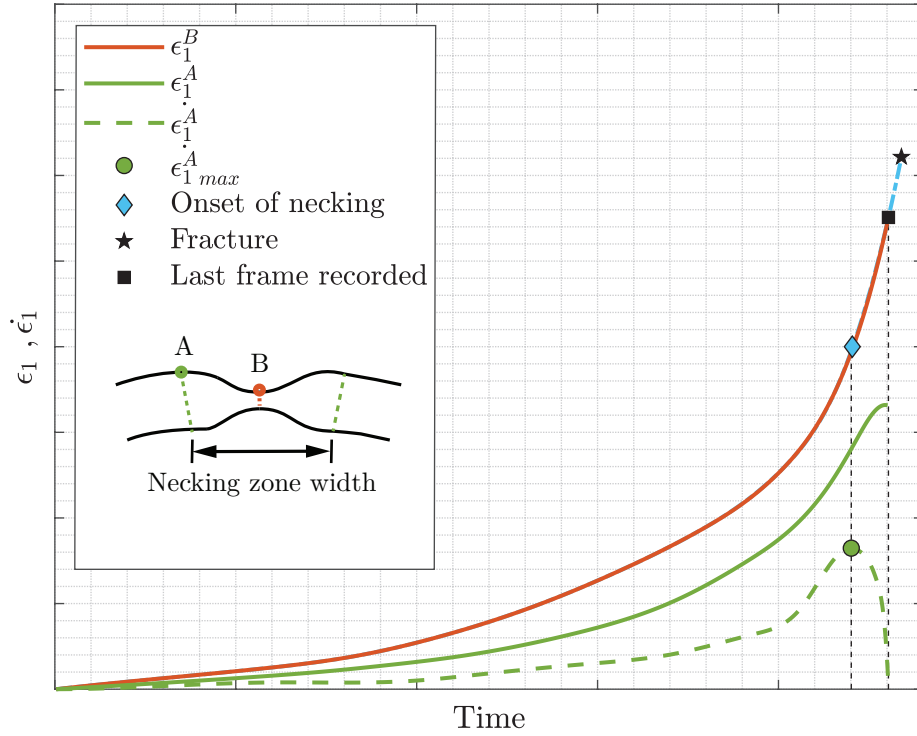


Figure 3.4: Time-dependent necking detection methodology suggested by Martínez-Donaire. Adapted from Martínez-Donaire *et al.* (2014)

and so the curvature is equal to zero (curvature radius goes to infinity). Then the curvature increases as the bending progressively increase. Once the onset of localized necking is reached, the curvature starts to decrease because of the localized flattening of the outer surface. This approach neglects the calculation of instantaneous sheet thinning. Thus, this method is beneficial especially in stretch bending tests in which the strain gradients through-thickness make the calculation of thinning using the conservation of the volume ($\epsilon_3 = -\epsilon_1 - \epsilon_2$) impossible.

3.3 Variables controlling formability

Formability is controlled by multiple variables and FLC can not be considered an intrinsic feature of the material. However, investigating the effects of the entire set of variables which affect formability explodes the number of experimental

conditions to consider. Furthermore, the effects of certain variables can be offset by varying some others, making the interpretation of the results more challenging, such as the coupled effect of temperature and strain rate. For this reason, only the temperature, punch radius, and materials are considered in this investigation as "main variables of interest".

Limit strains are affected by many variables in addition to temperature, punch tip radius, and material. In the second part of this section, a brief analysis of further variables controlling formability is given. Knowing the effects of these variables on forming limits allows a greater awareness in the design of the experiment. The main factors included are temperature distribution on specimen surface, anisotropy, lubricants, and punch speed (strain rate).

3.3.1 Temperature

Temperature is naturally a key variable in warm forming. The first studies about the benefits of elevated temperature on aluminum forming were carried out about 50 years ago. Ayres and Wenner (1979) studied the effect of temperature and strain rate on aluminum AA5182-O within a temperature range of RT to 200 °C. Under ambient temperature conditions, this alloy is affected by dynamic strain aging and, as a consequence, the Portevin–Le Chatelier effect. This phenomenon is revealed by serrated stress flow and Lüders band on the specimen. Furthermore, the elongation evolves in the uniform region (i.e., before the onset of localized necking), and the plastic deformation shows strain rate insensitivity. By raising the temperature, the microscopic mechanism of dynamic strain aging decreases, and the stress flow appears to be smooth and stable. The increase in post uniform strain more than offsets the reduction of uniform deformation, resulting in an overall increase of ductility. An important observation has to be made concerning this point. Increasing the temperature stabilizes the development of localized necking, which appears increasingly distributed on the specimen surface and less detrimental to the deformation process. In other words, higher limit strains are achieved since deformation can develop in a stable fashion in the early part of post uniform deformation. This

observation is in good accordance with the shifting from strain hardening to strain rate hardening mechanisms. The higher sensitivity of flow stress to strain rate hardening as opposed to strain hardening improves the stability of diffuse necks. A localized neck can only develop when the strain rate in the neck is higher than outside (this observation underlies some necking detection methods, such as Volk and Hora's method). However, if increasing the strain rate requires higher and higher stresses, then the strain rate difference between the necked section and the uniform deformation region is constantly counterbalanced, in the same way as the strain hardening limits the localization of necking. In other words, the increased strain rate dependence of aluminum alloys under warm forming conditions stabilizes the material by postponing localized necking until higher strains (Atzema, 2017).

More recently, warm forming research has also focused on high strength aluminum alloys, such as the AA7075-T6, in an effort to further reduce vehicle weight. Hui *et al.* (2012) indirectly investigates the forming response of AA7075-T6 basing his research on Nakazima dome-height measurements over a range of temperatures from 20 °C to 260 °C. AA7075-T6 shows the highest ultimate tensile stress and the lowest total elongation at ambient conditions. Up to 100 °C, no remarkable changes in mechanical properties are observed. From 140 °C to 220 °C, ultimate strength decreases, and maximum elongation increases. The sharp fall of mechanical properties noted at the highest temperature (260 °C) was supposed to be due to over-aging. The increased effect of strain rate hardening on flow stress is beneficial in suppressing necking instability by preventing plastic strain from concentrating in a localized neck. This behavior is entirely in line with that of AA5182-O. In magnitude, the limit drawing depth increases from 20 mm (RT) to 31 mm at 220 °C, and it stabilizes after this temperature. These results may indicate 220 °C as an optimum temperature. However, results are difficult to interpret since it is unclear if the dome height is measured at the fracture or before strain localization.

The decrease in mechanical properties caused by the overaging phenomenon was later investigated by Ivanoff *et al.* (2015). Ivanoff examined the influence

of warm forming on AA7075-T6 alloy, in particular, the process of retrogression and re-aging. This process is a multi-step heat treatment and is applied to the aluminum alloy after peak aging. In the retrogression step, the material is heated between 190 °C and 240 °C for a short time (10-200 s). After that, the material is re-aged in T6 condition (typically 24 h at 120 °C). It was found that after completing the retrogression and re-aging steps, the material gains both strength and corrosion resistance. The reason for this result is the microstructure achieved, between the T6 temper (thin and homogeneously distributed η' precipitates) and the T73 temper (η precipitate at grain boundaries).

3.3.2 Punch radius

The effect of punch curvature on the strains within the sheet metal sample and the impact of curvature on the onset of localized necking was noticed in the early studies of FLDs by Nakazima *et al.* (1968) and Hecker (1972). Looking at a pure bending deformation, the convex side of the bend (outer surface) experiences tension, and the concave side (inner surface) experiences compression. The opposing stress signs generate a neutral layer where neither tension nor compression occurs. Bending deformation is often coupled with stretching deformation in sheet metal forming operations. The addition of a membrane strain state to the pure bending deformation state moves the neutral plane through the sheet thickness forwards the inside of the blank (Fig. 3.5a). If the stretching is sufficiently high, the neutral plane is located outside the physical metal blank, but strain gradients are still present (Fig. 3.5b).

Many sheet forming practitioners adopted the intuitive idea that the strain on the middle layer of the sheet is the representative value to compare with FLCs. This approach was found to underestimate the strain limit by Tharrett and Stoughton (2003). Their experiments involved stretch bending tests of 1008 AK steel and 2000 series aluminum strips over a punch with different tip radii, ranging from 12.5 mm to 0.5 mm. Contrary to expectations, he discovered that tests stopped at the onset of localized necking showed a middle layer strain

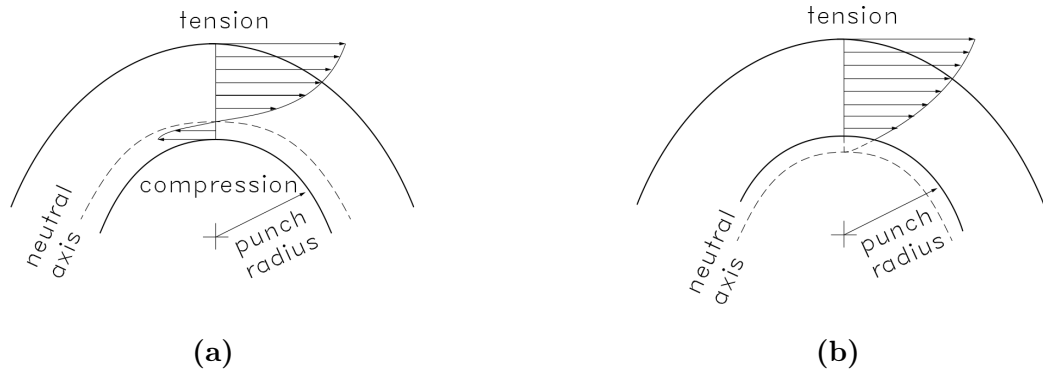


Figure 3.5: Stretch-bending strain distributions under different stretching versus bending conditions: (a) low stretching strain component, and (b) high stretching strain component.

well above the necking limit measured for in-plane tests. In fact, they found that localized necking only occurs when the strain on the concave side of the metal sheet (inner surface) exceeds the necking limit for in-plane strains.

Tharrett and Stoughton (2003) attributed this counter-intuitive result to the fact that localized necking is an instability phenomenon that simultaneously involves the movement of all material points within the thickness. Thus, necking instability requires that the in-plane limit strain is exceeded at all layers, and the onset of necking only occurs when the lowest strain through the cross-section (inner side) exceeds the strain limit. This explains why the evidence of necking is observed on both sides of the blank. On contrary, the localized necking can not occur in pure bending deformations (V-bend tests) since the inner surface always remains under the negative value of stress and always below the limit strain required to initiate necking Min *et al.* (2016). In a V-bend test, the ductile fracture (which defines the fracture forming limit curve) initiate on one side of a curved surface and propagate to the other side.

The effect of curvature is usually analyzed by considering the bend severity ratio t/R , where t is the sheet thickness and R the punch radius. This parameter is useful since the magnitude of the strain gradients is influenced by both punch radius and sheet thickness. However, further consideration is needed on the relationship between thickness effect and punch curvature effect on the limit strain. The thickness and strain gradients can also affect formability

independently. Thus, the changes in limit strain obtained by increasing the punch curvature at a constant sheet thickness differ from the changes in limit strain obtained by increasing the sheet thickness at a constant punch radius. Increasing the sheet thickness appears to be more effective since benefits of higher strain gradients are added to the benefits of “true thickness effect” (thickness effect in the absence of curvature) (Charpentier, 1975).

3.3.3 Materials

Aluminum 5000-series and 7000-series are important alloy groups used in structural applications for the BIW in the automotive industry. Two alloys have been selected for the current investigation within these categories, namely aluminum alloys AA5185-O and AA7075-T6.

Aluminum AA5182-O

Al-Mg-Mn alloys provide a good compromise between formability and strength, achieved by solid solution and strain hardening. In the automotive industry, the AA5182 alloy is used especially for the inner panels of BIW, because of its good weldability and its high specific strength. Further improvements in properties, such as corrosion resistance and surface quality, are achieved by small additions of other alloying elements and specific processing routes.

The combination of a high amount of magnesium and cold working significantly accelerates the precipitation of Mg_2Al_3 in wrought alloys. This compound precipitates at the grain boundaries, and it forms a continuous grain-boundary network, which reacts with the aluminum-magnesium matrix and produces susceptibility to stress corrosion cracking (SCC). This phenomenon is highly affected by temperatures and is restricted to alloys in which the amount of magnesium exceeds 3 wt%, such as aluminum AA5182 alloy. The addition of manganese to the solid solution promotes more general precipitation of phases within the structure and improve the resistance to SCC. Furthermore, the exposure at temperatures over 180 °C results in coarsening of the metal microstructures, producing a discontinuous boundary precipitate structure and

reducing SCC (MacKenzie, 2016b).

The intense interaction between Mg atoms and dislocations significantly increases the strength of AA5182 alloy, but on the other hand leads to Lüder lines formation. In forming of mild steels, the unstable stress flow affect the transition between elastic and plastic deformation. Thus, the stretcher lines can be avoided by a final slight rolling pass to move permanently the strain states on the sheet surface in the plastic deformation field. This solution cannot be adopted for aluminum alloys since the unstable stress flow affect the whole flow curve. Therefore, other treatments have been developed. Increasing the grain size limits Lüder lines defects, so metal sheets can be annealed after cold rolling to achieve partial recrystallization. As regards the alluminum AA5182-O in discussion, the “O” temper condition means "annealed wrought product". Thus, the ductility and the surface finishing are improved at the expense of maximum strength. It is important to emphasise that grain size growth must be carefully controlled, since too large grains ($> 100 \mu m$) cause a detrimental surface finish known as “orange peel effect”. (Hirsch, 1997).

Aluminum AA7075-T6

The AA7075 shows one of the highest specific strength among the aluminum alloys. For this reason, it is widely used in the aircraft industry. Automakers are looking at this alloy as a substitute for steel in high-strength demanding applications, such us B pillars safety requirements. The AA7075 alloy belongs to the heat-treatable alloys, which means its properties are highly affected by temperature. Thus, several temper conditions are available on the market depending on the characteristics needed by the designer. The T-temper designation is the most widely used to specify the different heat-treatments. In accordance with this classification, the “T” is always followed by digits that specify the main steps (first digit) and the specific treatment (following digits) applied to the material. The following gives a description of the main processings (MacKenzie, 2016a).

- T3: solution heat-treated at elevated temperature following hot forming,

quenched, cold worked, and naturally aged to a stable condition. The solution heat treatment must allow the main alloying elements to go into solution before quenching, and the cold working must provide a specific strain hardening. This temper is widely used in 2000 series alloys, such as AA2024, which benefit from cold working.

- T4: solution heat-treated, quenched, and naturally aged to a stable condition without being previously cold worked.
- T6: solution heat-treated, quenched, and artificially aged to achieve precipitation hardening to peak strength. This temper does not involve any significant cold working process, which means that if a cold rolling process is performed, the mechanical properties do not benefit from it.
- T7: solution heat-treated, quenched, and artificially overaged (i.e., beyond the peak strength). This temper is widely used in 7000 series to increase the corrosion resistance. T73 and T76 are commonly used to improve stress corrosion cracking and exfoliation corrosion, respectively.

Given the influence of temperature on heat-treatable alloys, warm forming operations must be carefully controlled. If exposed to high temperatures, the aluminum blank can easily overage, resulting in loss of mechanical properties. Bolt *et al.* (2001) measure the Brinell hardness on the wall of a box-shaped AA6016-T4 blank, and they found a decrease of hardening from 77 (RT condition) to 70 (175 °C). However, the warm temperatures can be targeted to the enhancement of corrosion resistance by controlling the over-aging in the warm forming and paint bake cycles. In line with this reasoning, it is possible to start forming aluminum blanks in T6 temper conditions and to get the T73 or T76 condition at the end of the vehicle production.

3.3.4 Temperature distribution

The experiment can be carried out both isothermal and non-isothermal. In the isothermal way, the specimen and the punch are both heated at the same

temperature. In the non-isothermal way, the specimen is heated by the dies, whereas the punch is cooled by water. Because of the heat removal by the punch, temperature gradients exist in the specimen during the forming process. Temperature differences cause properties differences in the metal blank, and they can affect formability. Specifically, temperature gradients (by cooling the punch) enhance the deep drawability of the AA5182 alloy (Takata, 2013).

3.3.5 Anisotropy

Due to their crystallographic structure and the characteristics of the rolling process, sheet metals generally exhibit a significant anisotropy of mechanical properties. Anisotropy is commonly described by two parameters: the normal anisotropy (R -value), and the planar anisotropy (ΔR). The normal anisotropy is also known as Lankford parameter, and it shows the different behavior between the in-plane deformation and the through-thickness deformation. If the R -value changes depending on the in-plane direction (calculated with reference to rolling direction) the material displays planar anisotropy. If the Lankford parameter is greater than unity, it indicates that the width strain is greater than the thickness strain. This behavior generally means a higher resistance in the through-thickness deformation and an improved sheet drawability. These parameters are usually helpful in predicting formability defects in the uniaxial strain field, such as wrinkling. However, they become meaningless in predicting limit strains under plane strain conditions, and fracture. For this purpose, the FLCs are required, or in the absence of data, the total elongation is more indicative than R -values.

3.3.6 Lubricants

Lubricants play a significant role in sheet metal forming, by providing a better distribution of strains on the blank surface and decreasing the friction between the blank and the punch surfaces. In manufacturing, these effects improve the drawability, the surface finishing, and the tool life. In this experiment, lubricants are used to control the strain distribution on the specimen surface. Lubricants

facilitate the sliding of the sheet metal over the punch surface; therefore, they make the localized necking to appear at the punch tip. This behavior is important because the investigation focuses on plane strain conditions, which can only occur at the punch tip. In fact, plane strain conditions ($\epsilon_2 = 0$) are obtained thanks to the specimen geometry (4.1.2) and the friction forces, which prevent the shrinking along the punch axis. Hence, friction conditions can influence the location of instability and the degree of nonlinearity in the strain path, but they do not affect the necking limit. It is important to note that plane strain is the weakest forming condition. Thus, localized necking occurs more easily under plane strain conditions, making the detection of localized necking easier in this experiment.

3.3.7 Punch speed

The most straightforward way to change the strain-rate of forming process is by adjusting the punch speed. Naka *et al.* (2001) investigated the limit strains of aluminum alloy AA5083 in a wide range of temperatures and strain-rates. In Naka's experiment, temperatures vary between 293 K and 573 K. Punch speeds vary between 0.2 and 200 mm/min, and as a consequence, strain rate increase from 10^{-4} to 10^{-1} s^{-1} , respectively. Limit strains are obtained for different strain states with Marciniak tests. After that, the full FLCs are computed through the M-K method.

The experiment shows that increasing the punch speed decreases the limit strains. Thus, high strain rates have a negative impact on formability, and increasing the deformation speed decreases the ductility of the aluminum blank. However, the effects of strain rate are not uniform all over the temperature range. Under room temperature conditions, the punch speed does not affect the limit strain. By contrast, the highest strain rate (10^{-1} s^{-1}) entirely offset the benefits of warm forming at the highest temperature (573 K), and limit strains at the highest temperature and speed are nearly the same as those at RT. Accordingly to Naka, these results are due to the rise of m -value and the decrease of n -value with increasing temperature. Under RT conditions, the

m -value is low and rather insensitive to the strain-rate, whereas n -value varies from 0.05 to 0.20 in the strain-rate range of 10^{-1} to 10^{-4} . On contrary, at 573 K, n -value is small ($n = 0.02$ - 0.05), and it is almost constant over the entire strain-rate range. In other words, the formability is strongly affected by the strain hardening (n) instead of the strain rate hardening (m) at low temperature.

These results confirm Naka's previous investigation on the same alloy. In this test, the limiting drawing ratio considerably decreases with the increase of punch speed because of the higher stress of the blank in the flange part. The drawbacks of strain-rate have been later outlined for the aluminum alloys AA5182, AA5754 and AA6111-T4 by Li and Ghosh (2003) and for AA5086 by Zhang *et al.* (2014).

3.3.8 Contact pressure

In stretch-bending (or Nakazima) tests, the out-of-plane deformation produces non-plane-stress forming conditions because of the contact pressure between the punch and the blank. It is widely accepted that the through-thickness pressure influences the limit strains. Min *et al.* (2016) investigated this phenomenon running some Nakazima and Marciniak tests, and taking into account previous results obtained by Stoughton and Yoon (2011). First of all, the radius of the hemispherical punch was reduced to amplify the pressure effects. Then, the results from the Nakazima tests were aligned with the results from Marciniak tests using a compensation process to quantify the effect of contact pressure. In fact, Marciniak tests do not suffer from contact pressure effect since the blank and the punch are separate by the blank carrier.

The principle behind Stoughton's compensation process is that plastic deformation occurs at constant volume. For this reason, the hydrostatic pressure does not affect the plasticity equations (there is no plastic dilatancy). Therefore, hydrostatic pressure has no influence on limit strains and the MK analysis. Following this reasoning, it is possible to think of a triaxial stress state as the sum of a biaxial stress state under hydrostatic pressure conditions. The

equivalent plane stress state $(\sigma_1^{eq}, \sigma_2^{eq}, 0)$ to a triaxial stress state is obtained by subtracting the σ_3 (contact pressure) to the remaining components (Eq. 3.8).

$$\begin{aligned} (\sigma_1, \sigma_2, \sigma_3) &= (\sigma_1^{eq} + \sigma_3, \sigma_2^{eq} + \sigma_3, \sigma_3) \implies \\ \implies (\sigma_1^{eq}, \sigma_2^{eq}, 0) &= (\sigma_1 - \sigma_3, \sigma_2 - \sigma_3, \sigma_3 - \sigma_3) \end{aligned} \quad (3.8)$$

This means that the limit strain is achieved at higher stresses in an out-of-plane deformation than in an in-plane deformation. In other words, the contact pressure is beneficial in delaying the onset of localized necking. Min confirmed the accuracy of Stoughton's compensation process on high-stress steel.

Noder and Butcher (2019) use this approach to compensate for the effect of contact pressure on a Nakazima test of AA5182. The AA5182 was found to be more sensitive than steel to the choice of strain hardening law in the pressure correction process. In particular, the lower the hardening coefficient, the larger the effect of contact pressure in delaying the the onset of necking. Under biaxial stretching conditions, the compensation process appears to over-compensate the pressure effect since strains (thus the equivalent strain) are higher in the right-hand side of the FLD and the strain hardening capacity decrease with increasing the strain. This phenomenon might be significant at warm temperatures (increasing the temperature decreases the hardening coefficient), even though this investigation only regards plane strain conditions.

Chapter 4

Experimental work

This chapter outlines the experimental work. Section 4.1 gives the project set up, the variables of the experiment, the specimen shape, and the test matrix. The development of this analysis must take into account the previous results from the literature review in Chapter 3, and it must focus on the scope of the experiment without exploding the number of runs. Thus, only the effects of temperature, punch radius, and material are considered. Section (4.1.3) displays the test matrix and summarizes the dependent variable ranges, the experimental conditions, and the number of repeats for each condition. Then, Section 4.2 describes the hardware tools used in the experiment. In this section, the design details of the adapters purpose made are displayed, and before that, Section 4.2.1 gives an overview of existing tools used in the experiment. In Section 4.2.3, some basics of Digital Image Correlation technique (DIC) are introduced. Finally, given the fundamental role of temperature in the experiment, Section 4.3 shows the thermal simulation implemented to assist the thermal analysis in the experiment.

4.1 Experimental methods

The experiment consists in firmly clamping the specimen between the binder and the die, heating it at the desired temperature, and then bending it with a cylindrical punch. The strain magnitude is recorded on the outer surface of the sheet metal using Digital Image Correlation technique.

The amount of “bending-strain component” is controlled by changing the punch tip radius, whereas the “stretching-strain component” depends on the punch displacement, since the experiment does not involve drawing (sliding between the sheet metal and the dies). All painted specimens are painted before the heating phase and tested within the same day to avoid the paint prematurely cracks before fracture occurs, by compromising the strain record. Two thermocouples clamped to the outer surface of the dies check the temperature for the whole duration of the experiment, more details about the temperature control are given in Section 4.3.

4.1.1 Variables

Dependent variable

The aim of the study is the limit strain under plane strain conditions, which is the dependent variable of the experiment. Limit strain means either the strain at the onset of necking or the strain just before ductile fracture. In fact, in a metal blank under stretch-bending load, the fracture (so limit strain) can occur because of both ductile fracture and localised necking mechanisms. Which of the two ductile fracture mechanisms appears at first depends on the geometry (punch radius) and the material properties, and cannot be defined a priori.

Independent variables

This analysis focus on the effect of three main independent variables: materials, punch radius, and temperatures.

Materials. The analysis involves two material: the non-heat-treatable 5182-O alloy (1.5 thickness), and the heat treatable 7075-T6 alloy (2.0mm thickness). Tables 4.1 and 4.2 give their main mechanical properties and their compositions, respectively.

Table 4.1: Main mechanical properties of AA5182-O and AA7075-T6 alloys (Sante DiCecco, private communication).

	Yield stress [<i>Mpa</i>]	UTS [<i>Mpa</i>]	Uniform elongation [-]	Total elongation [-]
5182-O	144	305	0.205	0.265
7075-T6	523	574	0.112	0.146

Table 4.2: Nominal composition of aluminum AA5182-O and AA7075-T6 alloys¹.

	5182-O	7075-T6
Aluminum, Al	93.2 - 95.8 %	87.1 - 91.4 %
Chromium, Cr	0 - 0.10 %	0.18 - 0.28 %
Copper, Cu	0 - 0.15 %	1.2 - 2.0 %
Iron, Fe	0 - 0.35 %	0 - 0.50 %
Magnesium, Mg	4.0 - 5.0 %	2.1 - 2.9 %
Manganese, Mn	0.20 - 0.50 %	0 - 0.30 %
Silicon, Si	0 - 0.20 %	0 - 0.40 %
Titanium, Ti	0 - 0.10 %	0 - 0.20 %
Zinc, Zn	0 - 0.25 %	5.1 - 6.1 %
Other, each	0 - 0.05 %	0 - 0.05 %
Other, total	0 - 0.15 %	0 - 0.15 %

Temperatures. As regards both AA5182-O and AA7075-T6, the temperature must be higher than 100°C to make the temperature benefits noticeable. As shown in Section 3.3.1, the AA5182-O does not undergo overaging and appears to show an optimum forming temperature at 220°C, whereas the optimum forming temperature of A7075-T6 was found at 200°C. Then, both alloys are tested at RT, 175°C and 225°C. As regards to the AA7075-T6 alloy, a further testing condition is set at 125°C. In fact, temperature sharply decreases the mechanical properties of this alloy, and it may be attractive evaluating the formability at temperatures lower than 150°C.

Punch radius. The magnitude of strain gradients through-thickness is affected by punch radius and sheet gauge. In this investigation, the sheet thickness is

¹<http://www.matweb.com/index.aspx> [accessed: 17.12.2019]

constant, and the curvature effect has been evaluated only by changing the punch tip radius. At the University of Waterloo, room temperature tests were carried out by Cheong (2019) with different punch radii ranging from 0.4 mm to 15 mm. Punch with smaller than 2.0 mm radius results in a cutting type operation instead of forming because of the large clearance between the punch and the binder. Therefore, punch radii of 2, 5, and 15 mm (Fig. 4.1) are selected for this work.

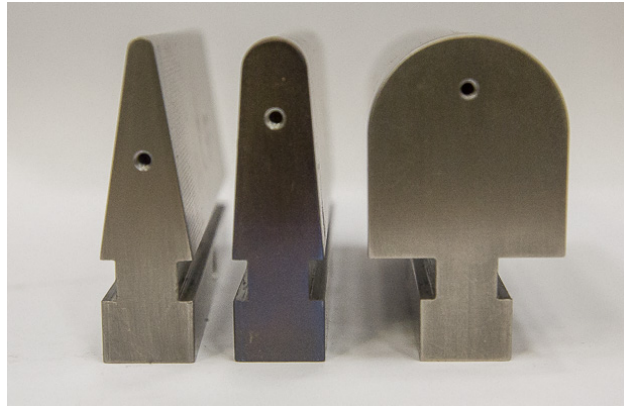


Figure 4.1: Cylindrical punches used in the experiment (2, 5, and 15 mm radius from left to right). The threaded holes allow to fasten the thermocouple to the punch wall.

Control variables

The remaining variables discussed in section 3.3 are the control variables of the experiment.

Non-isothermal conditions. This work takes into account isothermal conditions (both punch and dies are heated to the same temperature). An imbalance of temperature between the die and the punch produces temperature gradients on the specimen surface, and it can enhance the forming limit of the sheet metal (Section 3.3). In this experiment, the isothermal conditions are assessed by a direct measurement of temperatures in two significant spot on the specimen surface. More details about temperature control are given in Section 4.3.2.

Anisotropy. The effect of anisotropy is controlled by cutting all specimens in the same direction. In aluminum metal forming, the rolling direction is usually

considered the weakest, which is the most attractive in the research activity and suggested by the standard. For this reason, and the absence of available data, all AA5182-O specimens have been cut along the rolling direction. However, previous investigations conducted at the University of Waterloo found the transversal to rolling direction (90°) to be the weakest of AA7075-T6 alloy. The resistance to localized necking along the transverse direction is 16% lower than along the rolling direction at RT. This difference decreases to 7% at 150°C (Sante DiCecco private communication, 2019). For this reason, AA7075-T6 specimens have been cut in the transverse direction to obtain the actual lower bound of stretch-bending limits for this alloy.

Punch speed. The punch velocity is set to 1 mm/s accordingly to the standard. However, this value affects the period of time between the beginning of deformation and the reaching of limit strain. Thus, the number of DIC pictures recorded for each repeat (fixed frame rate). In the preliminary test under RT conditions, the punch speed was decreased to 0.25 mm/s to get closer to the target value (400 images per repeat) because of little punch stroke and the slow speed cameras used (7 fps). The impact on the final result is marginal, given that the effect of strain rate increase with increasing the temperatures, and it is negligible at RT.

4.1.2 Specimen

All tests use the same specimen shape (Fig. 4.2), whereas the thickness depends on the material: 2 mm for AA7075-T6 and 1.5 mm for AA5182-O. The outer diameter simplifies the alignment with the dies. The narrow section in the middle and the fillet radii are adequately designed to obtain, as much as possible, plain-strain conditions during the deformation. The narrower the specimen section, the less friction between the punch and the specimen because of the smaller contact surface and pressure. The challenge is to find the neck size that ensures enough friction forces along the punch axis to prevent the narrowing, and as a consequence, it keeps null the minor strain. The dimensions are based on the experience of previous tests conducted at the University of Waterloo.

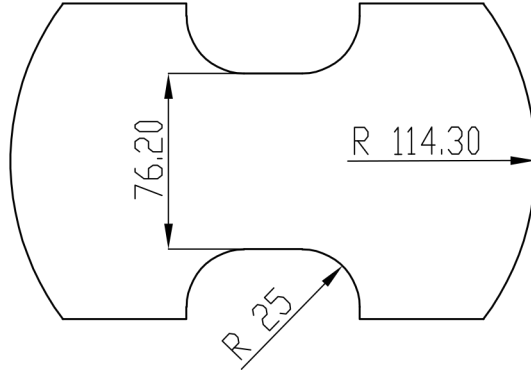


Figure 4.2: Specimen shape and main dimensions ($[mm]$).

4.1.3 Test matrix

Tables 4.4 and 4.3 give the test matrix of the experiment of AA7075-T6 and AA5182-O, respectively. Four repeats are run for each experimental condition.

Table 4.3: Test matrix of aluminum AA5182-O

P.R. [mm]	2	5	15
T [$^{\circ}C$]			
RT	4	4	4
175	4	4	4
225	4	4	4

Table 4.4: Test matrix of aluminum AA7075-T6

P.R. [mm]	2	5	15
T [$^{\circ}C$]			
RT	4	4	4
125	4	4	4
175	4	4	4
225	4	4	4

4.2 Experimental equipment

The experiment needs two main equipment to perform the stretch-bending deformation under warm temperature conditions and in the meanwhile record the outer surface strains. The first apparatus is a stretch bending machine capable of running high temperature forming. The second is a Digital Image Correlation (DIC) camera.

At the University of Waterloo crash and forming labs, stretch bending tests under room temperature conditions and warm forming experiments are run on separate testing machines. Thus, some adapter tools are required to perform stretch bending tests on the warm forming press. First of all, an adapter has been designed to fit the stretch bending punches on the punch extender of the warm forming press. Then, two clamping plates have been made to fix the existing stretch bending dies on the heated plates of the warm forming press.

4.2.1 Existing instruments

Figure 4.3 shows the rough dies layout used for warm Marciniak and Nakazima tests. The dome punch (6) is fitted on the punch extender (2) thanks to the stud bolt (7). Four external holes (6a) around the punch base circumference enable to tighten the punch to the extender. Four heat cartridges (1) heat the punch extender and the punch. Thermocouples placed next to the heat cartridges control the heat output to get the target temperature thanks to a closed control-loop. The specimen is clamped in between the die and the binder (5) and heated to the required temperature by the heat cartridges (9) in the heating plates (4). The overall assembly is heat insulated from the rest of the press by the insulation plates (3). Although four thermocouples are located in the thermal plates, their distance from the specimen prevents an accurate detection of the blank temperature. For this reason, the thermocouple (8) is added to get temperature measurements close to the punch tip. Finally, the hole in the lower part of the assembly makes it possible to install the DIC camera to record surface strain data.

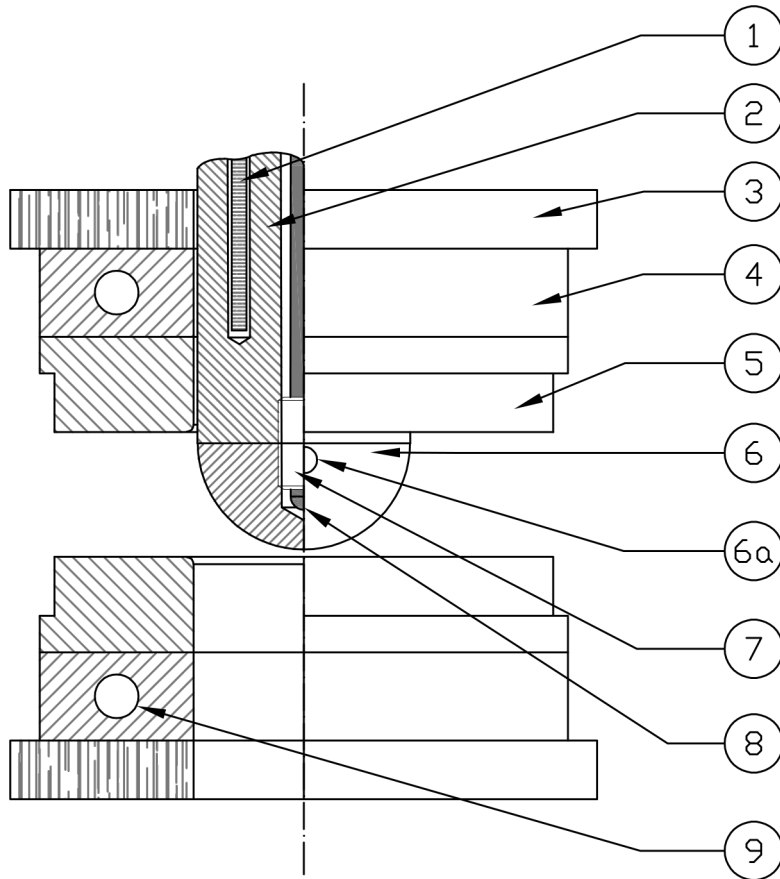


Figure 4.3: Basic layout of the existing warm forming press.

Fig 4.4 shows the die and the binder used for stretch bending experiments. The rectangular shape keeps strains as uniform as possible along the transverse direction of the specimen. In fact, circular dies produce the opening distance changing depending on the "transverse location". Thus, different strain values are obtained along the axis of the cylindrical punch. Furthermore, the hole dimension can be adjusted by changing the die insert (1). This provides better control of bending strain components. Finally, the surface of the die is covered by knurling to fix the metal blank and prevent deep-drawing.

Fig. 4.5 gives the stretch bending punch used in stretch bending tests at room temperature (5 mm tip radius). The adjustable base (4) holds different radius tools (3) thanks to a T-shaped rail. Once tools are in place, they are retained by the bolt (2). Then, since the tool axis always needs to be perpendicular to the specimen axis, two slots (1) were designed. These slots allow adjusting the perpendicularity by rotating the base around the centering hole (5) up to 60°.

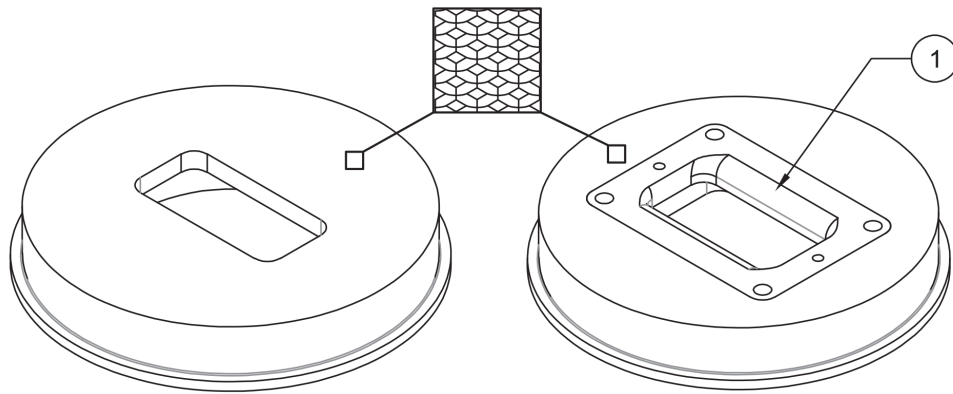


Figure 4.4: Existing stretch-bending dies for RT tests (insert gap: 52 mm).

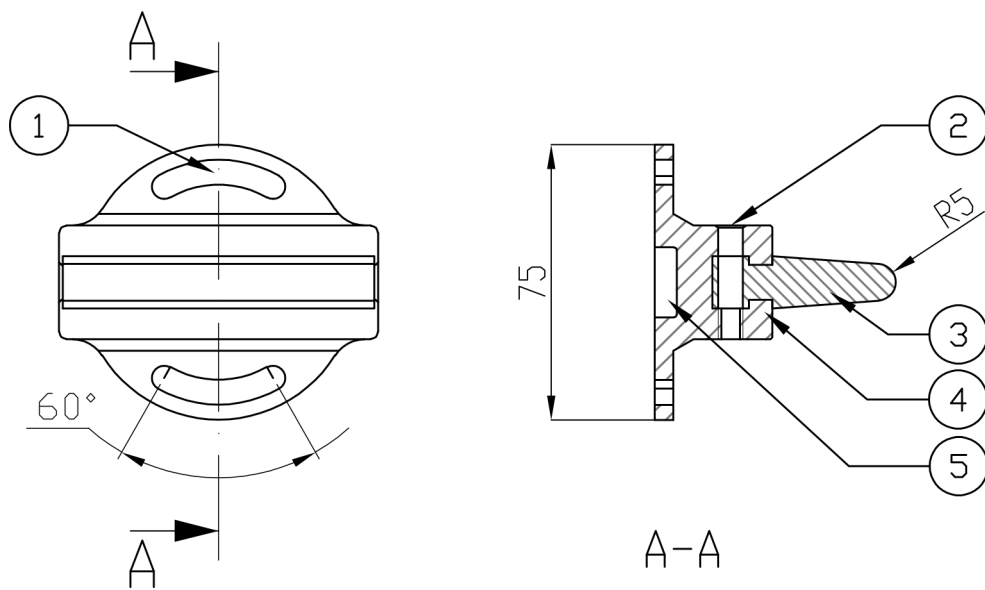


Figure 4.5: Existing stretch-bending punch-holder.

4.2.2 Adapting tools

Punch holder

The design of the adapter must take into consideration geometrical and thermal aspects besides the apparent feature of interfacing different bending punches with the punch extender.

The axis of the cylindrical punch must always be perpendicular to the specimen axis since the geometry of the experiment is not axisymmetric. The original solution to adjust the punch needs two holes in the extender to fix the slot bolts. Instead of drilling the extender, the stud bolt of the Nakazima punch is used. This solution does not require to operate on the punch extender but

prevents the alignment between the punch and the specimen (this feature is not necessary for Nakazima's test). The punch adapter is screwed to the extender in any position, then the perpendicularity is ensured by rotating the dies. As regards the thermal aspects, the design should reduce the exchanging heat by convection with the external air. For this reason, the distance between the punch tip and the base of the adapter is expected to decrease. However, this dimension establishes the maximum punch stroke (unknown). In a similar test under room temperature condition, Cheong (2019) obtained nearly 25 mm of maximum punch depth at the onset of necking. Under warm forming conditions, this distance should increase, and considering the high heat output from the heat cartridges, the tip to base distance has been increased from 45 mm to 68 mm. In Nakazima dome tests, the tip temperature is measured by a thermocouple inside the punch. This solution is difficult to implement on the stretch bending punches because of the small tip radii. For this reason and considering the punch temperature distribution, the thermocouple is fixed to the sidewall of the punch. The slot shown in Fig. 4.6 was machined to enable the thermocouple wire to get the surface without any additional operations on punches.

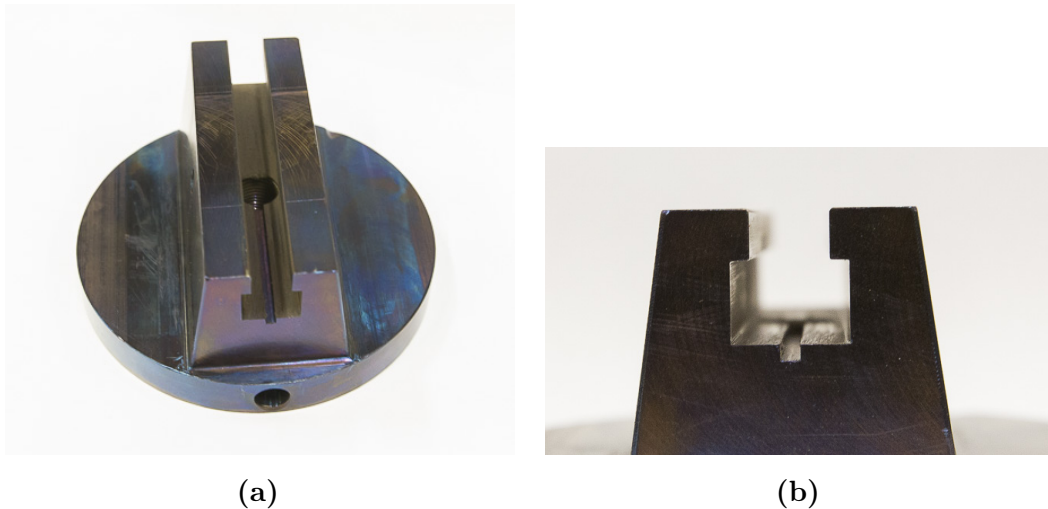


Figure 4.6: (a) Punch holder. (b) Detail of the slot machined to let passing the thermocouple wire.

Finally, the geometry of the T-rail was maintained from the original adapter. This design needs tight tolerances between the carriage and guide profiles to ensure heat exchange. Appendix AA provides the full drawing of the adapter.

Clamping plates

The role of clamping plates is to fasten the rectangular shape dies from the stretch bending machine on the warm forming press, and to enable the alignment between the die holes and the punch. This is possible by making a circular guide using the shoulder at the base of both die and binder. The dies can rotate until the punch is aligned, and then the clamping plates are fixed by tightening the four bolts to the heating plates. The sliding fit is only guaranteed between the dies cylindrical surfaces and the circular hole to not over-constraint the centering (no contact on the circular shoulder). Furthermore, the height of the shoulder is designed to get the interference fit once the plates are tighten. Some drawbacks of this simple solution are the increased distance between the specimen and heat cartridges and the die centering, which relies on the bolts at the edges of the plates. Appendix BB provides the full drawings of the clamping plates sent to the machine shop.



Figure 4.7: Clamping plate

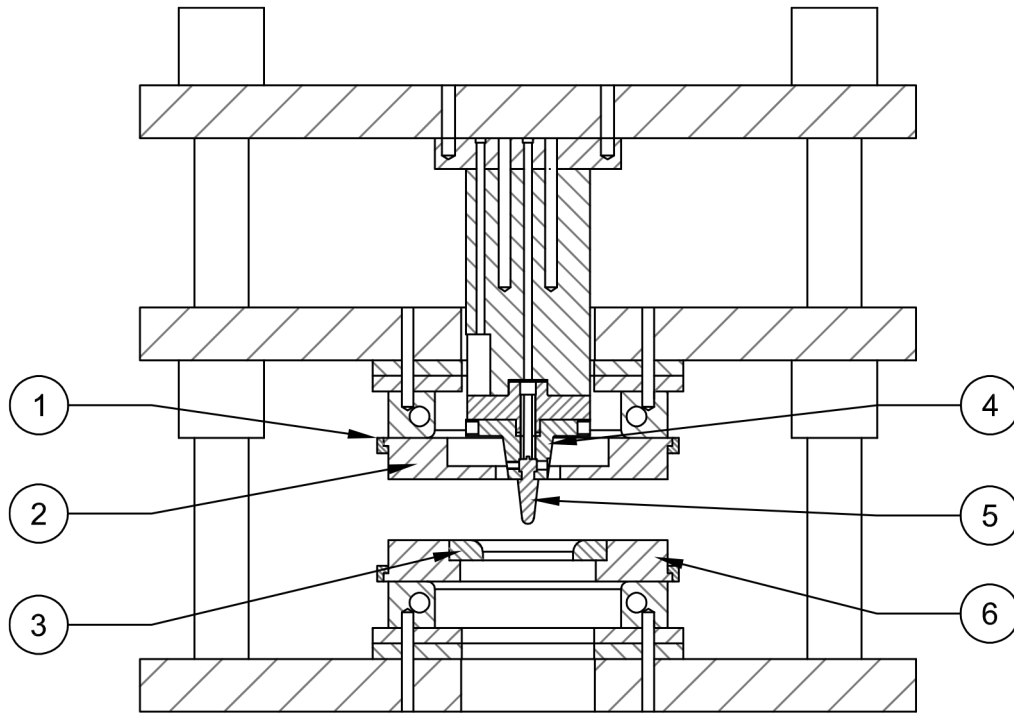


Figure 4.8: Final assembly (approximate) of the warm forming press: (1) clamping rings, (2) top die, (3) rectangular shape insert, (4) punch holder, (5) punch, (6) bottom die.

4.2.3 Digital Image Correlation

Strain measurements were carried out by a Digital Image Correlation (DIC) camera. DIC is a surface displacement measurement technique that can capture motion, deformation, and shape of solid objects. The use of DIC has become widespread in forming limit characterization because of the ability to record any deformation path over the entire area of interest. The technique is based on the successive comparison of two images. The first corresponds to the reference state, and the second corresponds to a strained state. In order to detect deformations, the surface of the specimen must display a random pattern, which is obtained (in this case) by spraying black speckles over a white paint background. Given that out-of-plane strains need to be detected in this investigation, all experiments employed a stereoscopic DIC system to capture 3D deformation images. The stereoscopic system needs to know the distance and the angle between the two cameras to obtain the third-dimension measurements.

These parameters are computed via software during the calibration process, which involves moving, imaging, and analyzing a rigid calibration target in front of the stereo camera pair. It is just as valid to calibrate after a test as before. The order is unimportant as long as the cameras do not move between calibration and test. During the experimental work, the system has been calibrated at the beginning of each test session, and whenever the position of the cameras changed or the projection error increased over the threshold value of 0.1. In fact, given a point in the camera 1 image, it is possible to predict a line along which it must lie in the camera 2 image accordingly to the calibration (epipolar line). The distance between the actual point position and its predicted epipolar line is called the projection error, and Vic-3D reports this distance in terms of pixels. Usually, this value is on the same order of magnitude of the calibration score (less than 0.1 on the advice of the manufacturer), and high values may indicate a disturbed calibration. However, stretch bending tests can experience high projection errors because of the sharp edges on the blank. If necessary, this issue has been solved by using the auto-correction tool on Vic-3D based on a image displaying a partial level of deformation (half of the total punch stroke).

Camera settings aim to get the higher sharpness and contrast of black and white pattern over the full period of the test. The main parameters are time of exposure and aperture. A long time of exposure lets more light hit the sensor, which means brighter and higher contrast images. However, it can result in blurred images. Ideally, the selected exposure time has to keep motions below approximately 0.01 pixels during the exposure. A wide aperture increases the light captured by the camera, but it decreases the depth of field, which has to be larger enough to cover the entire punch stroke during the test. If this does not happen, blurred and low contrast images result. This issue has to be also considered in focusing, which makes it possible to control the position of the focal plane (so the position of the depth of field).

4.3 Thermal analysis

The thermal analysis of the parts involved in the tests is crucial to achieving valid results. For this reason, this analysis is assisted by a thermal simulation. Section 4.3.2 gives the real thermal cycles of the specimen and some observations on the temperature analysis.

4.3.1 Thermal simulation

The simulation is carried out with LS-Dyna. The purpose of the simulation is to assist the setting of thermal parameters on the warm forming press. Figure 4.9a shows the control volume of the simulation, which includes the die, the binder, the punch, the specimen, and the punch holder. The boundaries conditions of the problem are the known temperature values at the base of the dies and punch holder (1, 2, 3 in Fig. 4.9b) and the convection boundary condition on the surfaces that exchange heat with the surrounding environment ($T_{inf} = 295 K$).

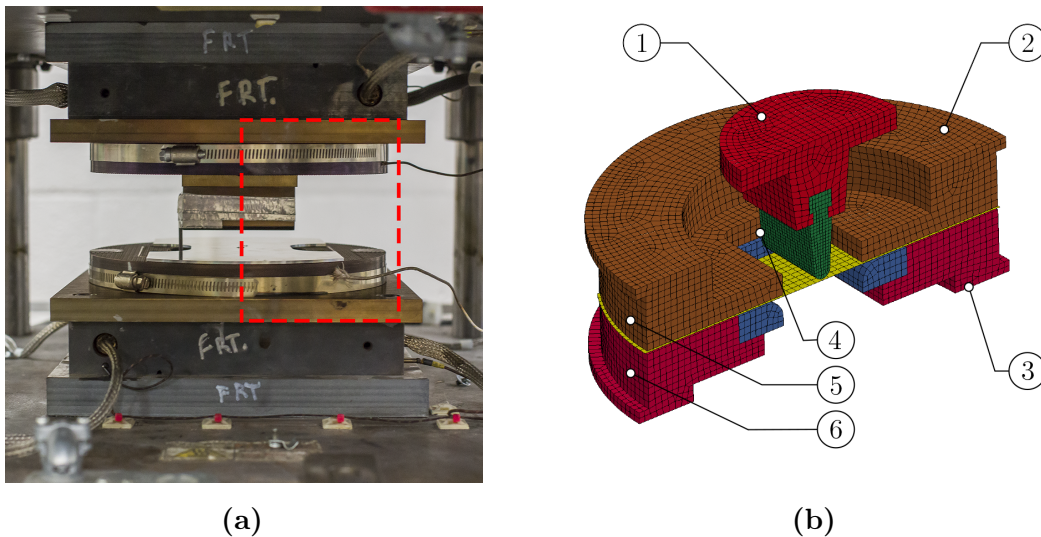


Figure 4.9: (a) control volume of the simulation. (b) known temperature boundary conditions: (1) punch holder base, (2) top die base, and (3) bottom die base. Validation spots: (4) punch, (5) top die, and (6) bottom die.

This choice is reasonable since the heat output of the heat cartridges is self-adjusted by a closed control loop to get the target temperature set on the

temperature controller. Therefore, thermocouples at the base of the dies and the punch holder continuously monitor the temperature evolution.

Only half of the assembly is considered to decrease the computational time. The heat flow on the cutting surface is set to zero by using the symmetry of the problem, which means there is no heat exchange from the right-hand side of the die to the left-hand side and vice versa.

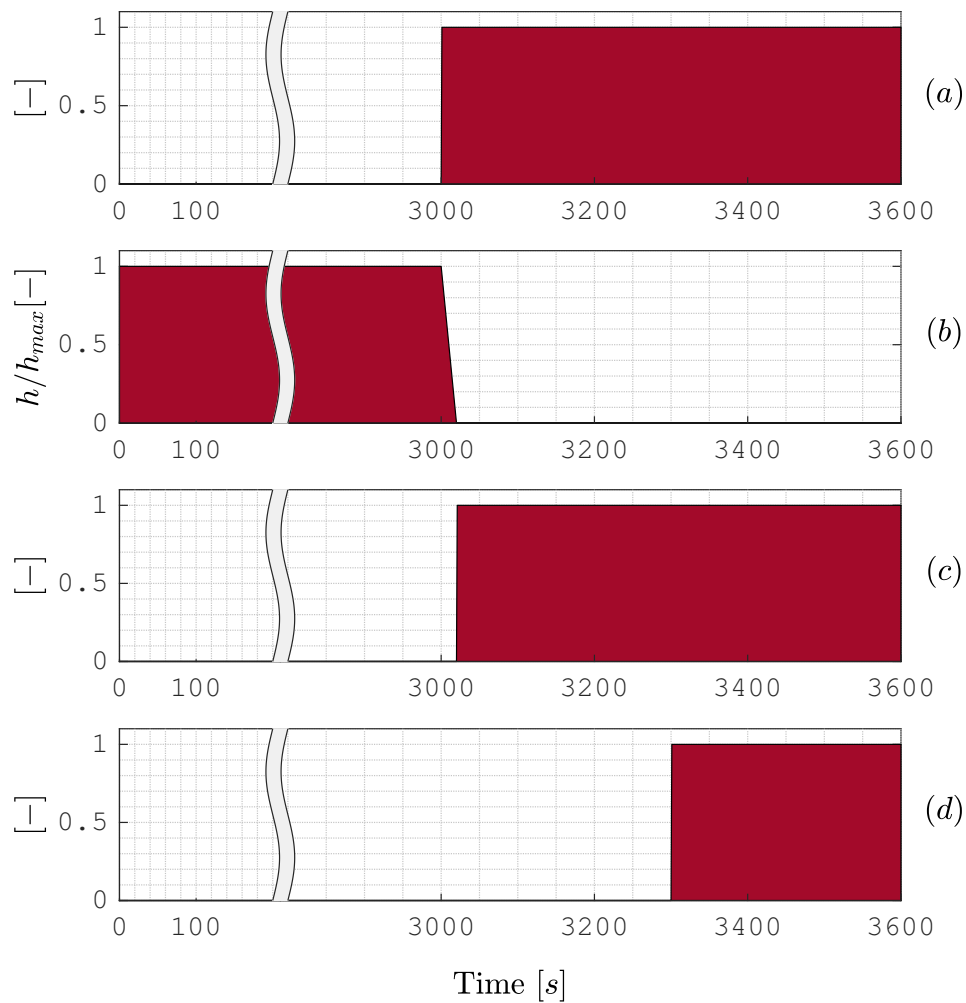


Figure 4.10: Time-dependent boundaries and contacts involved in the clamping phase: (a) bottom die-specimen contact, (b) convection coefficient dies top surfaces, (c) top die-specimen contact, (d) punch tip-specimen contact.

The thermal simulation on LS-Dyna allows simulating the first test repeat, which includes the transient analysis of the heating of the dies, the placement of

the specimen on the bottom die, the clamping phase, and the contact between the punch tip and the blank (starting of the forming operation). As regards the second repeat, only the second part of the simulation is needed (the analysis starts from the contact between the specimen and the bottom die). Since the part movements require a thermo-mechanical simulation, which increases the complexity and the computational time, all parts are stopped in their final position, and their movements are simulated by properly activating the contacts, and by varying the boundaries conditions during the simulation.

Fig. 4.10 shows the evolution of the boundary conditions and contacts during the simulation. At the beginning of the simulation ($t = 0$), the binder is in the upper position, and the top surfaces of the dies exchange heat with the surrounding environment ($h_{conv} = max$). The temperature at the boundary conditions 1, 2, and 3 (Fig. 4.9b) increases accordingly to the temperature measured by the thermocouples next to the heat cartridges. In the warm-up phase, the specimen is not in the forming position. Thus, the specimen-die contact is not activated yet. At the end of the die warm-up, the specimen is placed on the lower die (die-specimen contact on) and then clamped. During the clamping phase, the top surfaces of the dies and the binder are in contact by neglecting the specimen thickness. The clamping movement is approximately represented by progressively reducing to zero the convection coefficient of top surfaces of both die and binder. At the end of the clamping phase, the contact between the binder and the specimen is activated. Then, the contact between the punch tip and the specimen is turned on.

Fig. 4.11 gives the result of the simulation for the lowest specimen target temperature, $125^{\circ}C$ ($398 K$). The contact between the specimen and the dies is enabled at 3000 s, before that the specimen is not placed on the bottom die yet, and it keeps the constant room temperature level. Then, the specimen is placed on the bottom die and it is clamped accordingly to Fig. 4.10.

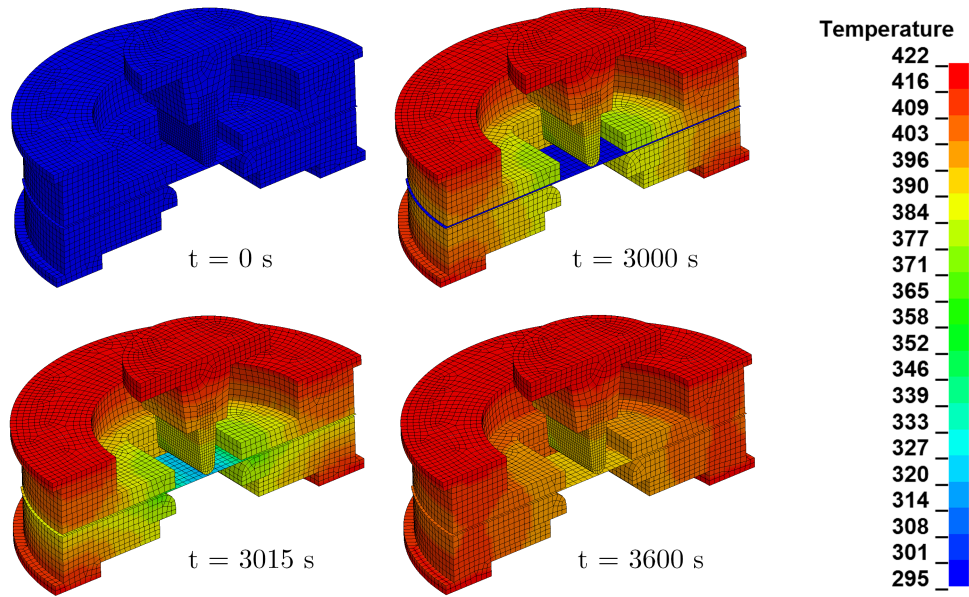


Figure 4.11: Main steps of the simulation for specimen target temperature 125°C (398 K). Temperature scale in Kelvin.

4.3.2 Validation and remarks

The simulation is validated by running entire heating cycles and by recording the temperature in three significant spots ((4), (5), (6), in Fig. 4.9b). (5) and (6) monitor the temperature of the upper and lower die, respectively, whereas (4) monitor the punch temperature.

These results have been used to set up the second round of thermal tests. In this stage, two thermocouples welded to the specimen (Fig. 4.12) directly record the temperature distribution.

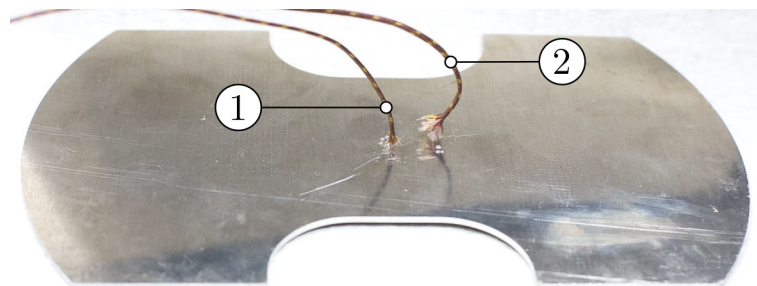


Figure 4.12: Two thermocouples welded to the specimen: (1) middle temperature (punch tip location), and (2) mid distance between the punch tip location and the die wall.

The plot in Fig. 4.13, Fig. 4.13, and Fig. 4.13 display the thermal cycle of the specimen for the target temperatures of 125, 175, and 225 °C, respectively (mean values and intervals of confidence are computed from 4 repeats). These curves allow to define the heating times and to estimate the highest temperature variation of the specimen expected during the deformation.

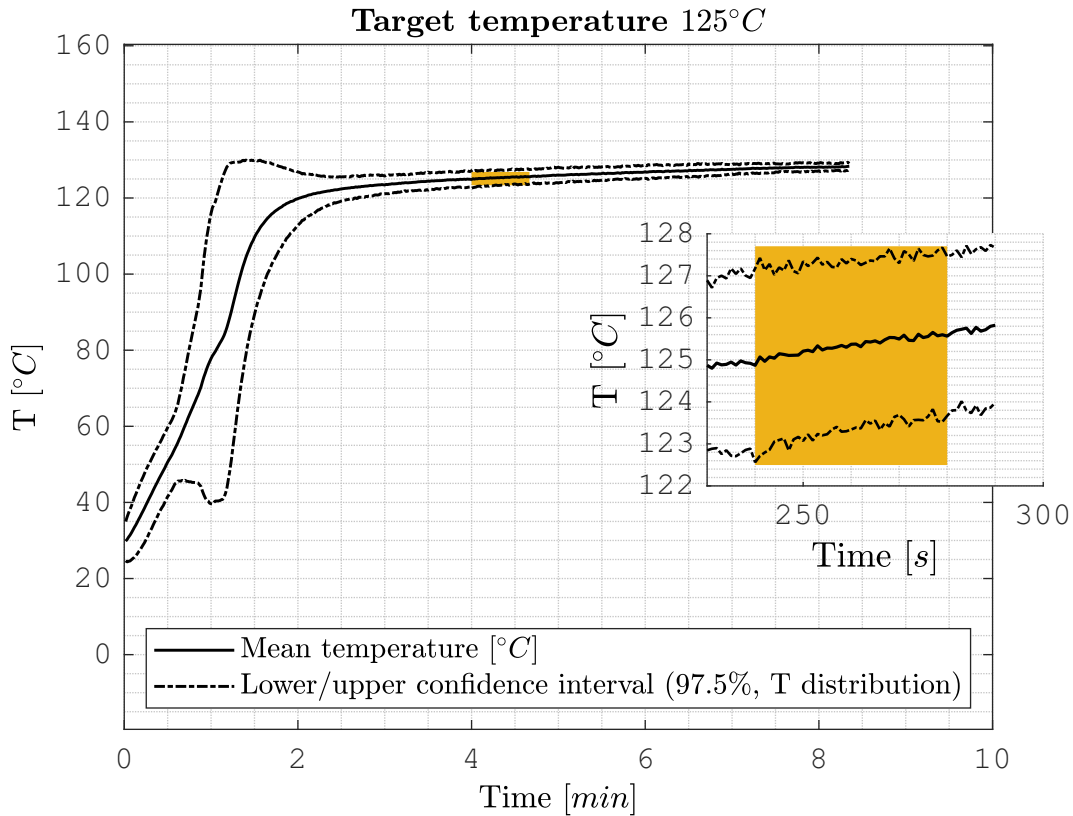


Figure 4.13: Temperature time series of the specimen for 125 °C target temperature. Confidence interval is computed with Student’s t-distribution after 4 repeats. The high variance in the first part of the curve is due to the manual control of the binder during the thermal analysis. In fact the clamping pressure affects the thermal resistance between the specimen and the die, so the temperatures in the initial part of the clamping highly depends on the pressure manually set on the press controller. Once the maximum clamping force is reached ($P_{max} = 295 \text{ kN}$), the temperature stabilizes.

The total deformation time ranges from 5 s to 40 s accordingly to the punch displacement (punch velocity 1 mm/s). The punch displacement, in turn, depends on temperatures, materials, and punch tip radii, so it depends on the variables of the experiments. The worst-case scenario (the highest temperature

variation) is obtained for the highest time of deformation, which means 40 s. This time turns in a temperature variation below 1°C for each target temperature. This temperature variation is not the temperature variability between each repeat. Given that the specimen temperature cannot be monitored during the deformation, the maximum variability between each test is achieved by computing the confidence interval from 4 temperature measurements with the specimen in Fig. 4.12 at the beginning of the experimentation.

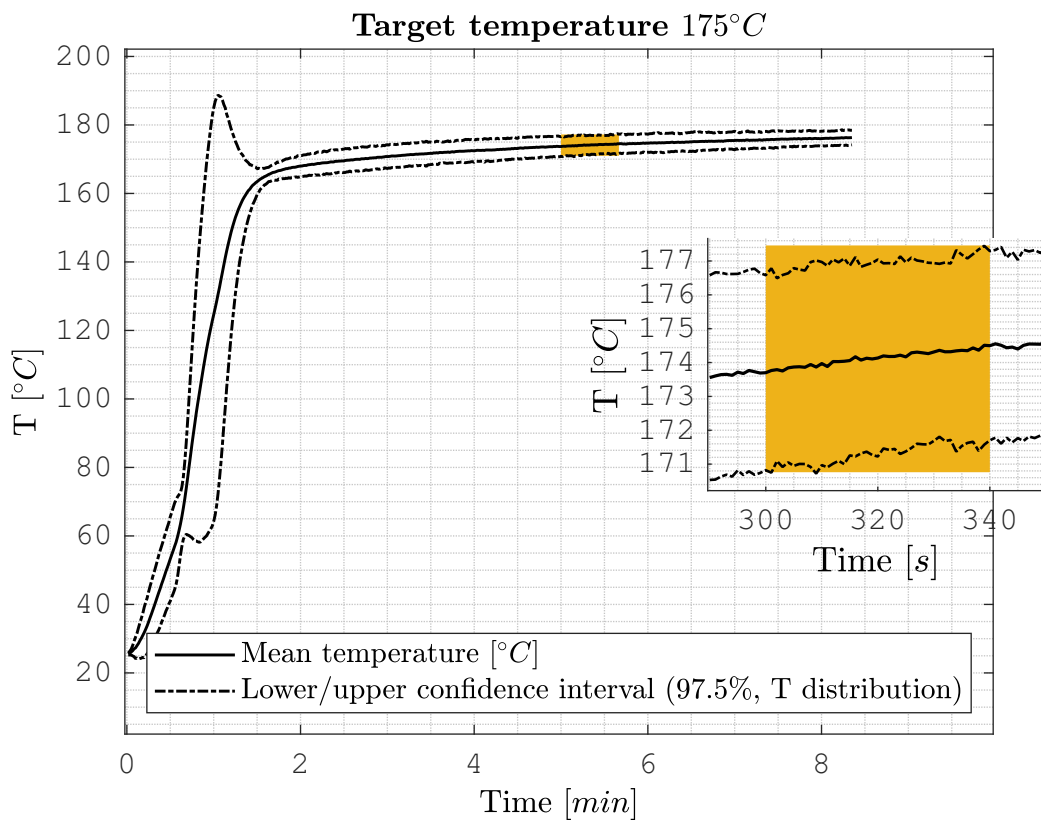


Figure 4.14: Temperature time series of the specimen for 175°C target temperature.

One last consideration about these plot relates to the temperature difference between the dies and the specimen. The temperature variation (between the beginning and the end of the deformation) does not only depend on the deformation period but also on the temperature increasing rate, which depends on the temperature drop between the die and the specimen. Increasing the dies temperature decreases the time needed to reach the target temperature, but it

makes more challenging the temperature control, since the deformation must start far from the equilibrium condition. If that were the case, the temperature variation during the deformation (height of yellow rectangles) and the error caused by missing the beginning of deformation (position of yellow rectangles) would be greater. After 120 s from the beginning of clamping, the plot shows almost flat temperature-time curves, which limit the temperature variation. Then, it is important to notice that if the punch tip temperature is lower (or higher) than the specimen temperature, a little bump down (or up) will result when the punch tip touches the specimen. This phenomenon is not noticeable. Finally, table 4.5 gives the thermal setting of the heat cartridges, and the temperature measured in the control spot accordingly to Fig. 4.9b. Table 4.6, shows the significant results extracted from the curves in Fig. 4.15 and Fig. 4.15 and 4.15.

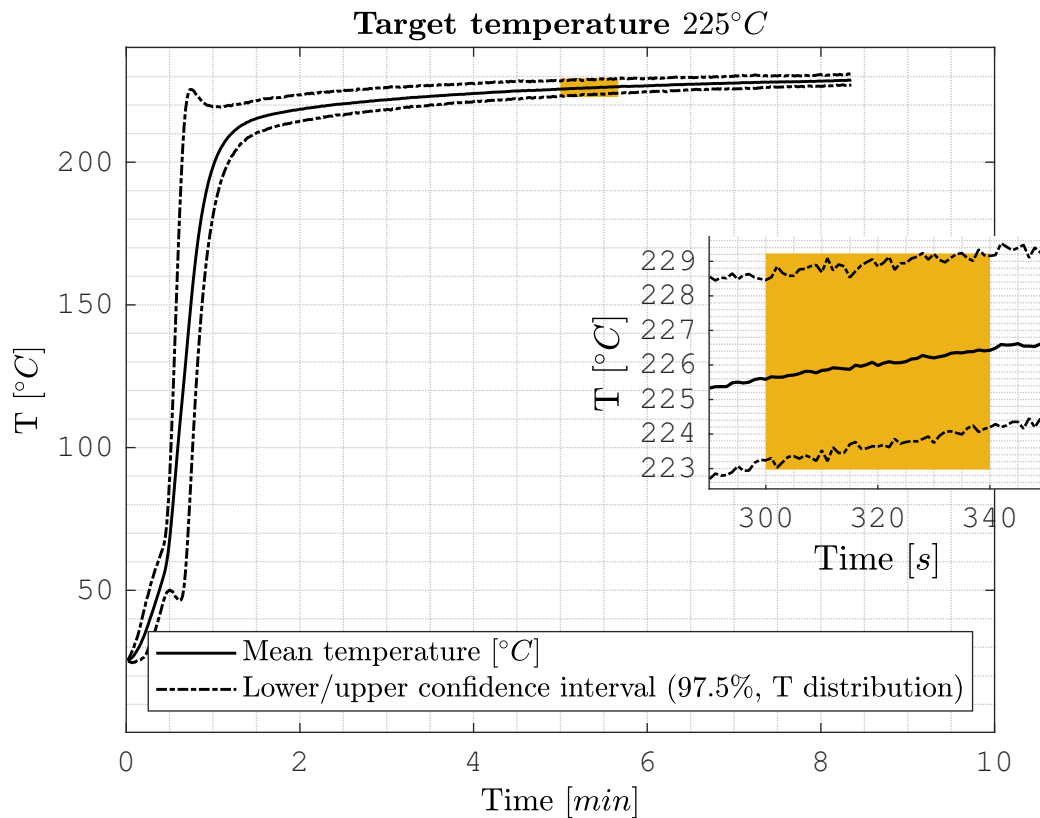


Figure 4.15: Temperature time series of the specimen for 225 °C target temperature.

Table 4.5: Thermal setting of the heat cartridges per each target temperature (TT). Dies and punch temperature refer to the temperature set on the controller. The subscripts of remaining temperatures refer to the checking spots according to Fig. 4.9b (T_4 = punch, T_5 = top die, T_6 = bottom die).

	TT 125 °C	TT 175 °C	TT 225 °C
Punch T [°C]	145	200	255
Top die T [°C]	132	185	235
Bottom die T [°C]	132	185	235
T_4 [°C]	124	169	219
T_5 [°C]	123	165	215
T_6 [°C]	122	175	221

Table 4.6: The maximum temperature variation (T_{mv}) represents the maximum temperature increase during deformation. The temperature range (T_r) is computed as the height of the yellow rectangles in Fig. 4.13, Fig. 4.14, and Fig. 4.15 and it represents the temperature range covered by the 97,5% of tests. The pre-heating time is computed after the clamping pressure reach the maximum value ($P_{max} = 295$ kN).

	TT 125 °C	TT 175 °C	TT 225 °C
Pre-heating time [s]	120	180	180
T_{mv} [°C]	0.8	0.6	0.8
T_r [°C]	+2.6/ - 2.4	+2.4/ - 4.1	+4.1/ - 2.0

4.4 Applied necking detection methods

Section 3.2.1 reviews the main necking detection methods. Among them, the curvature method is selected for this investigation at first since it does not require to compute the localized thinning rate due to necking. Furthermore, most of the methods (in contrast to the curvature approach) assume the presence of localized necking, which may not exist in stretch bending tests. Consider the time-dependent method by Volk and Hora (2011), for instance. The straight lines, which interpolate the first part and the end part of the thinning rate curve can always be drawn, regardless of the presence of necking or not. Thus, this method always produces an intersection point (that represents the onset of localized necking) even if the specimen fails without necking. These reasons

make the curvature method the most suitable approach at first. Then, once the onset of necking is observed, the time-dependent method can be applied to give further information on the limit strains.

Data extraction

At this point the images are already acquired, and they are post-processed by Vic-3D. The main post-processing parameters are the strain filter size (*pixel*), the step size, and the image resolution (*mm/pixel*) which give the virtual strain gage length (*mm*) by combining them together. The virtual strain gage length (VSGL) reflects the effective gage length over which the strains are averaged (similarly to a physical strain gage). The VSGL can affect the magnitude of strain data achieved, in this analysis the value of 0.5 *mm* is selected as a compromise between accuracy and computational efficiency (Cheong *et al.*, 2018). The output of post-processing is the spatial-distribution of logarithmic strain per each frame. At this stage, the strain time series (the development of strains at a fixed location by scrolling the images) can be extracted. The strain data are extracted as the average of strains within a circular area centered in the point showing the highest strain value in the last frame (Fig. 4.16). In turn, the last frame is the one preceding the frame which first shows visible fracture. According to this process, the fracture strain is the strain value averaged within the extraction area at the last frame.

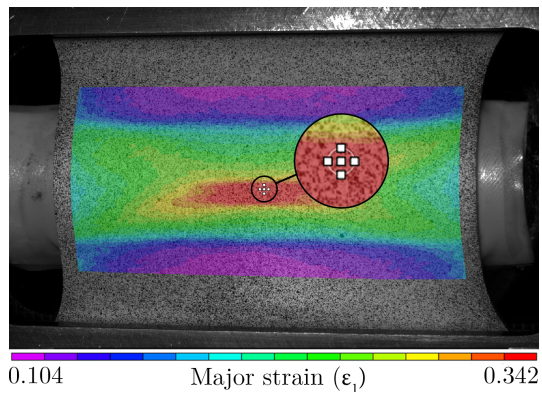


Figure 4.16: Area for major strain and curvature data extraction.

Limit strains are obtained by analyzing the curvature and the major strain time-series. To make this process as much user-independent as possible, all data are processed by a MATLAB script. The raw data are interpolated by a spline-fit curve using the SLM toolbox by John D’Errico².

Curvature method

Fig. 4.17 displays the typical trend of curvature as a function of major strain for the minimum and maximum punch.

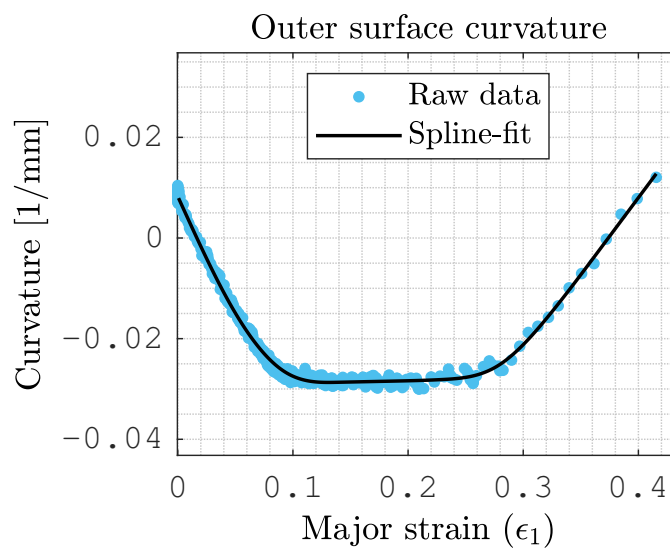


Figure 4.17: Outer surface curvature as a function of major strain for AA5182-O at RT.

In the initial part, the absolute value of outer surface curvature increases until the curvature radius of inner surface is equal to the punch tip radius. Then, the curvature is plateauing as the deformation proceeds by stretching. In the final part, the absolute value of curvature decreases as the onset of localized necking appears. By considering the physical process (Fig. 4.18), the curve fitting is improved by forcing the second derivative to be positive over the entire deformation, i. e., the function is forced to have a “concave up” shape (the first derivative ever-increasing), specifying the '`concaveUp`' shape prescription. If this were not, the outer surface curvature could decrease as bending process moves forward, or it could increase during the necking phase; both of the behaviors are unrealistic.

²<https://www.mathworks.com/matlabcentral/fileexchange/24443-slm-shape-language-modeling> [accessed: 01.13.2020]

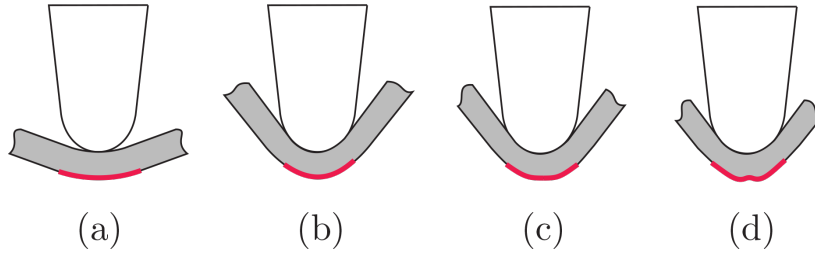


Figure 4.18: Illustration of outer surface curvature (highlighted in red) from the beginning of deformation (a) to severe necking (d). Localized necking appears when the outer surface at the punch tip starts to flatten (c).

Firstly, the script looks for the end of bending phase, which is the minimum of curvature function (always unique for the “concave up” assumption). Then, it fits the steady part of the curve with a straight line, and it computes the onset of localized necking by analyzing the deviation of the curvature function from the interpolated straight line. The deviation from the straight line is indicated with three layers of intensity (green, yellow, red) depending on the severity of necking (Fig. 4.19). This solution allows keeping records of three separate levels of deviation from the predicted trend (no localization \implies straight line). Localization is known to appear between the maximum curvature and the reversing of curvature sign (curvature equal to zero), but the exact location is unknown. The green level of necking corresponds to a decreasing of curvature of 0.005, the yellow level corresponds to a decreasing of curvature of 0.01, and the red level corresponds to a decreasing of curvature of 0.015. The correspondent increase in the curvature radius of outer surface depends on the punch radius. As regards to the 15 *mm* punch, the increase is 2.2 *mm*, 5.0 *mm*, and 8.5 *mm* for the green, yellow, and red necking levels, respectively. The interpolation range of the steady part of the curve plays a significant role in necking detection. The range is defined as the set of points with a *y*-value between the minimum curvature and the minimum plus a “threshold value” (TV). This value is about 10%-15% of the minimum value and is set to 0.001 (Sante DiCecco, private communication). The range is bounded in Fig. 4.19 by the black circles.

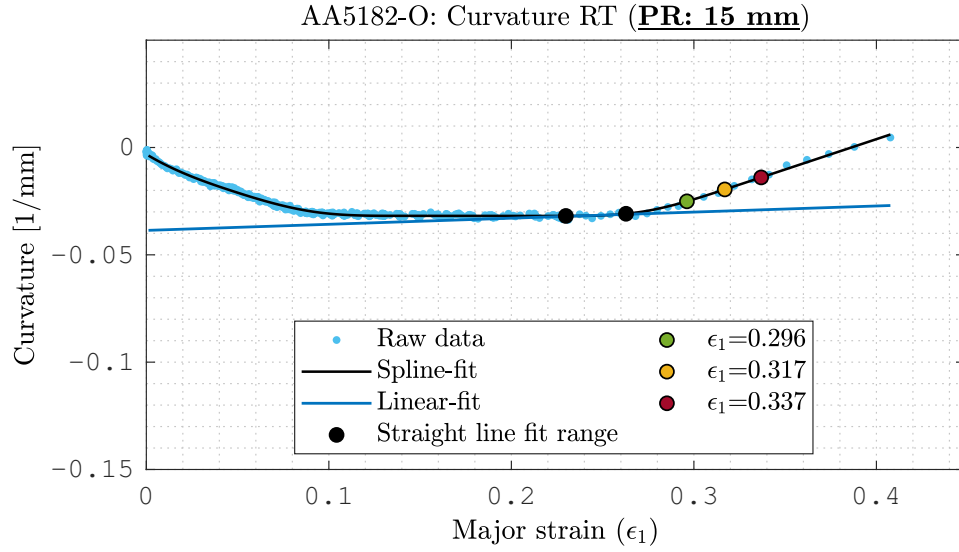


Figure 4.19: Example of curvature method analysis (AA5182-O, RT, 15 mm punch). Green level: 0.005 ()

Time-dependent method

The implemented time dependent method basically follows the Volk and Hora approach displayed in section 3.2.1. However, here the method is applied to major strains instead of the through thickness strains. The raw strain data are fitted by forcing the strain to increase monotonically (the magnitude of strains increase as deformation proceeds). Also the velocity should constantly increase in the location where data are extracted as a consequence of localization of strain (necking). However, the aluminum AA5182-O is affected by PLC effect, which produces serrated stress-strain curves and “oscillating” strain rates (Fig. 4.20). This phenomenon can significantly affect the slope of the straight line which fits the early stage of deformations, and as a results it can modify the limit strain. For this reason the second derivative of the strain rate function is forced to be constantly positive by one additional spline fit with the 'concaveUp' prescription.

Finally, the early stage and the late stage of deformation (corresponding to the first 5% and last 5% of the curve, respectively) are interpolated by two straight lines. Then, the intersection between the straight lines is computed.

Figure 4.20: PLC effect of AA5182-O (punch radius 15 mm, RT). The contour plot show the localisation of strain rate in the tilted bands (blue), and steady deformation ($\dot{\epsilon}_1 = 0$) in the remaining purple surface.

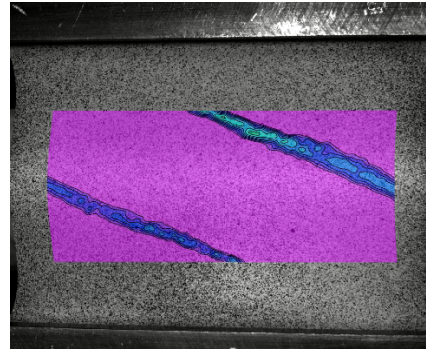


Fig. 4.21 illustrate the results of this process. The scripts used for both curvature and time-dependent methods are provided in appendix C.

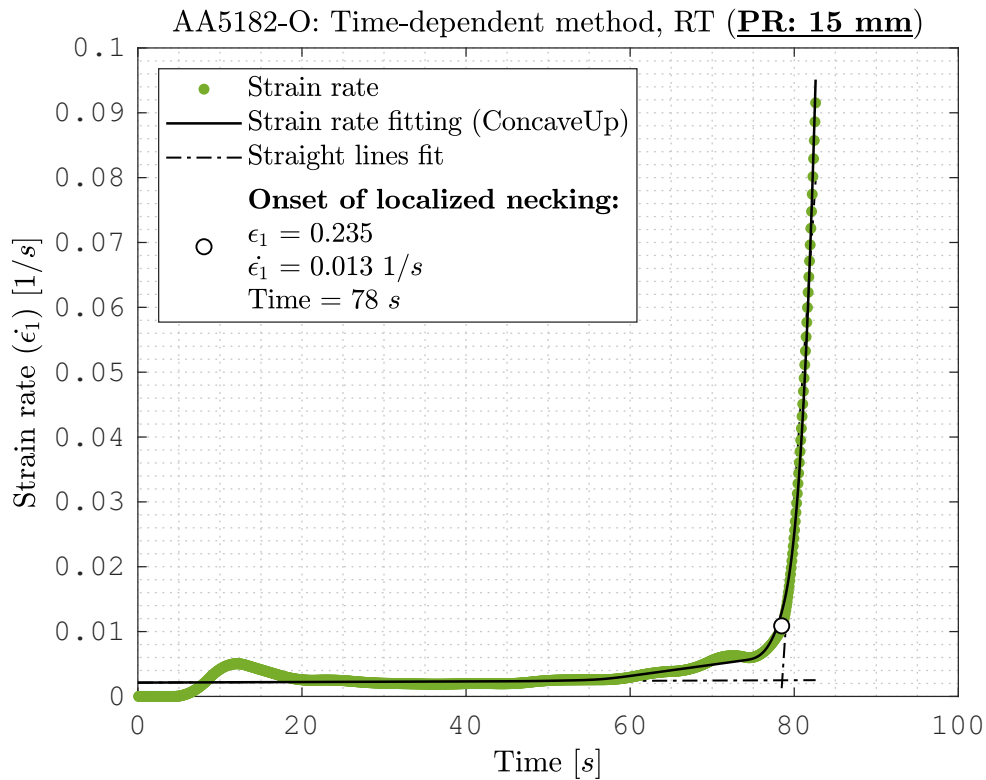


Figure 4.21: Example of time-dependent method analysis (AA5182-O, RT, 15 mm punch).

Chapter 5

Results

In this chapter the results of the experiment are given. In Section 5.1 and 5.2, the effects of temperature and curvature on limit strains of both alloys are discussed. In these sections, missing necking data mean that failure occurs without localized necking, unless otherwise specified. Subsequently, in Section 5.3 the effects of experimental variables on punch displacement are analysed. All results displayed in this chapter are the outcome of the average of four repeats, and repeatability is not shown to better highlights the trend. More details about repeatability can be found in Chapter 6 (Conclusions).

5.1 Temperature effects on limit strains

The AA7075-T6 shows increasing limit strains by raising the temperature from RT to 175 °C. At room temperature, failure appears without localization for both the 15 mm punch and the 5 mm punch, which means the failure mechanism is probably the ductile fracture under these conditions. The limit strain for the 15 mm punch increases of 16.2% in the range between 22 °C and 175 °C, considering the intermediate level of localization as limit strain (“yellow” necking). In the same range, the limit strain for the 5 mm punch increases of 57%, probably because of the curvature benefits in delaying the localization. However, both radii show a decreasing trend between 175 °C and 225 °C. Thus, an optimum temperature will be in this range.

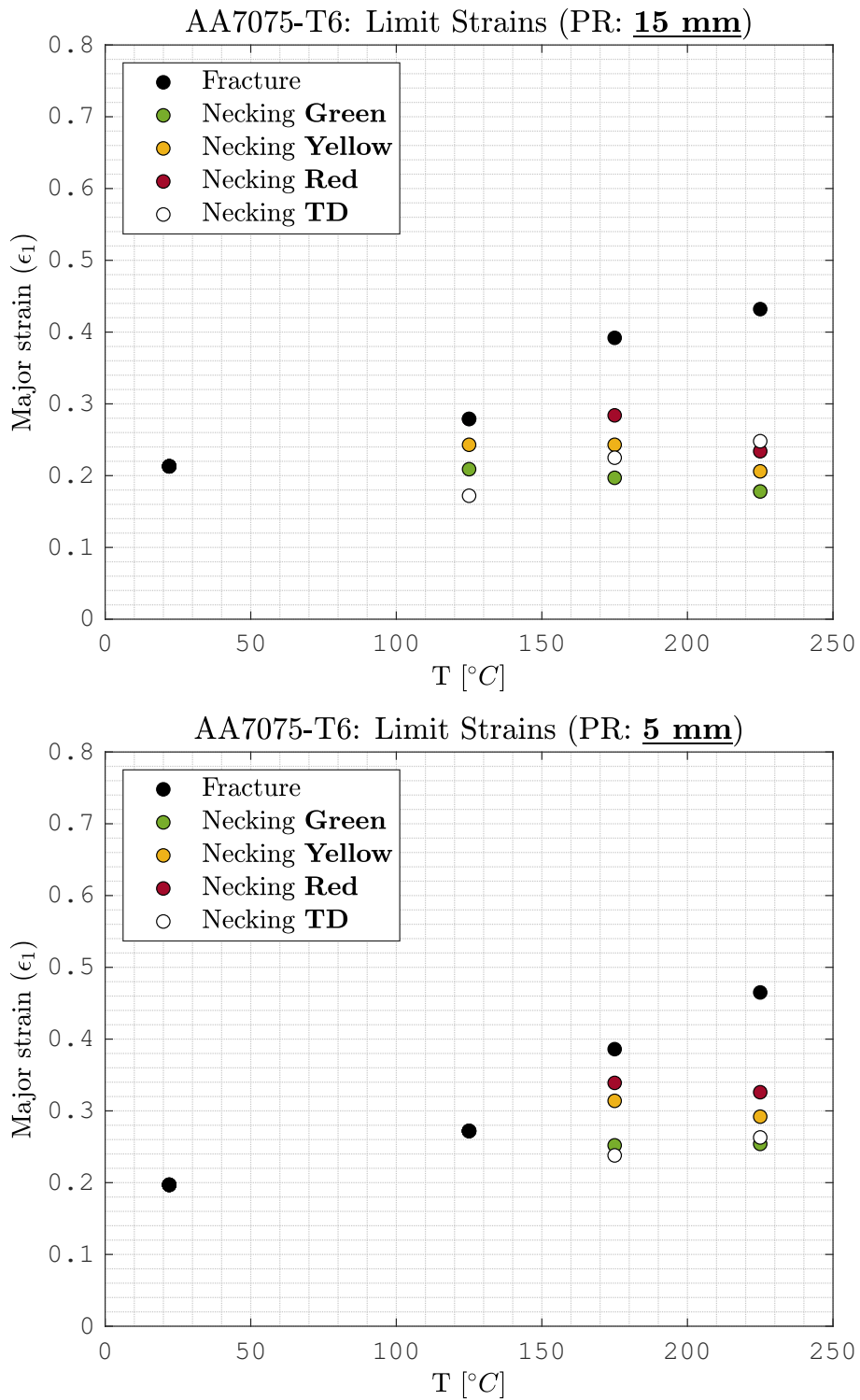


Figure 5.1: Temperature effects on AA7075-T6 limit strains; *top*: 15 mm punch radius, *bottom*: 5 mm punch radius. The levels of necking refer to the localization magnitude in accordance to the curvature method, from mild (green) to severe (red). "TD" refer to the time dependent method.

From a mechanical point of view, the negative effects of temperature over $175\text{ }^{\circ}\text{C}$ are justified by the decrease in strain rate sensitivity from 0.040 ($175\text{ }^{\circ}\text{C}$) to 0.032 ($175\text{ }^{\circ}\text{C}$) (Hui *et al.*, 2012). The drop of m -value is confirmed by the greater decline of the severe necking compared to the mild one. In other words, once the onset of necking appears, it gets worse more rapidly, as shown in Fig. 5.2 and Fig. 5.2. Furthermore, Huo *et al.* (2016) investigated the microstructure of AA7075-T6 after warm forming at $200\text{ }^{\circ}\text{C}$ using TEM microscopy and found a significant precipitate coarsening. This phenomenon facilitates the dislocation motion, and it decreases the work hardening capacity. Finally, the dynamic recovery becomes more pronounced at temperature over $200\text{ }^{\circ}\text{C}$, and Huo *et al.* (2016) observed a sharp strength reduction, accompanied by decreased uniform elongation and work hardening coefficient.

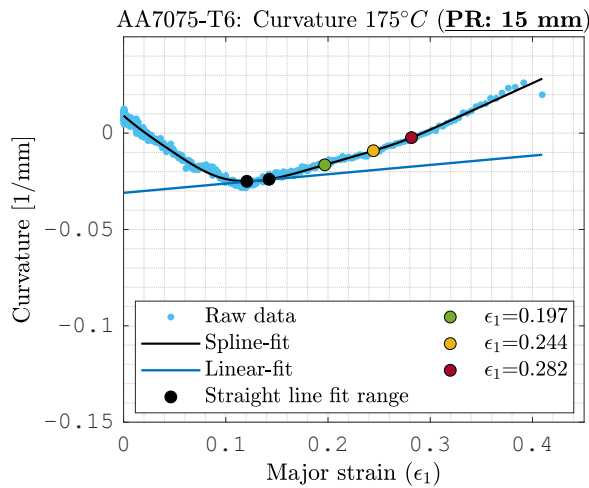


Figure 5.2: Outer surface curvature as a function of major strain of AA7075-T6 sheet at 175°C (15 mm punch)

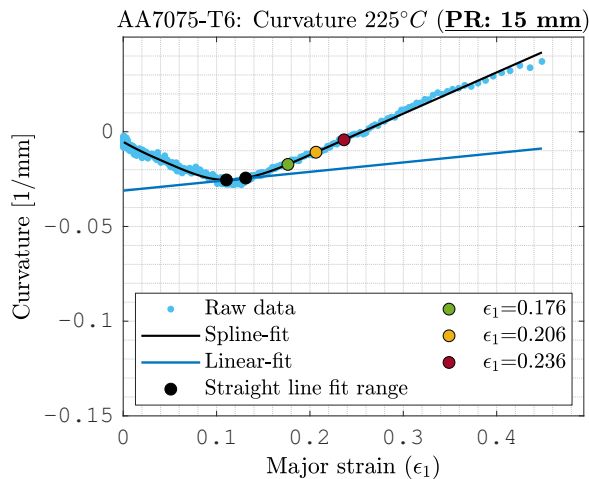


Figure 5.3: Outer surface curvature as a function of major strain of AA7075-T6 sheet at 225°C (15 mm punch)

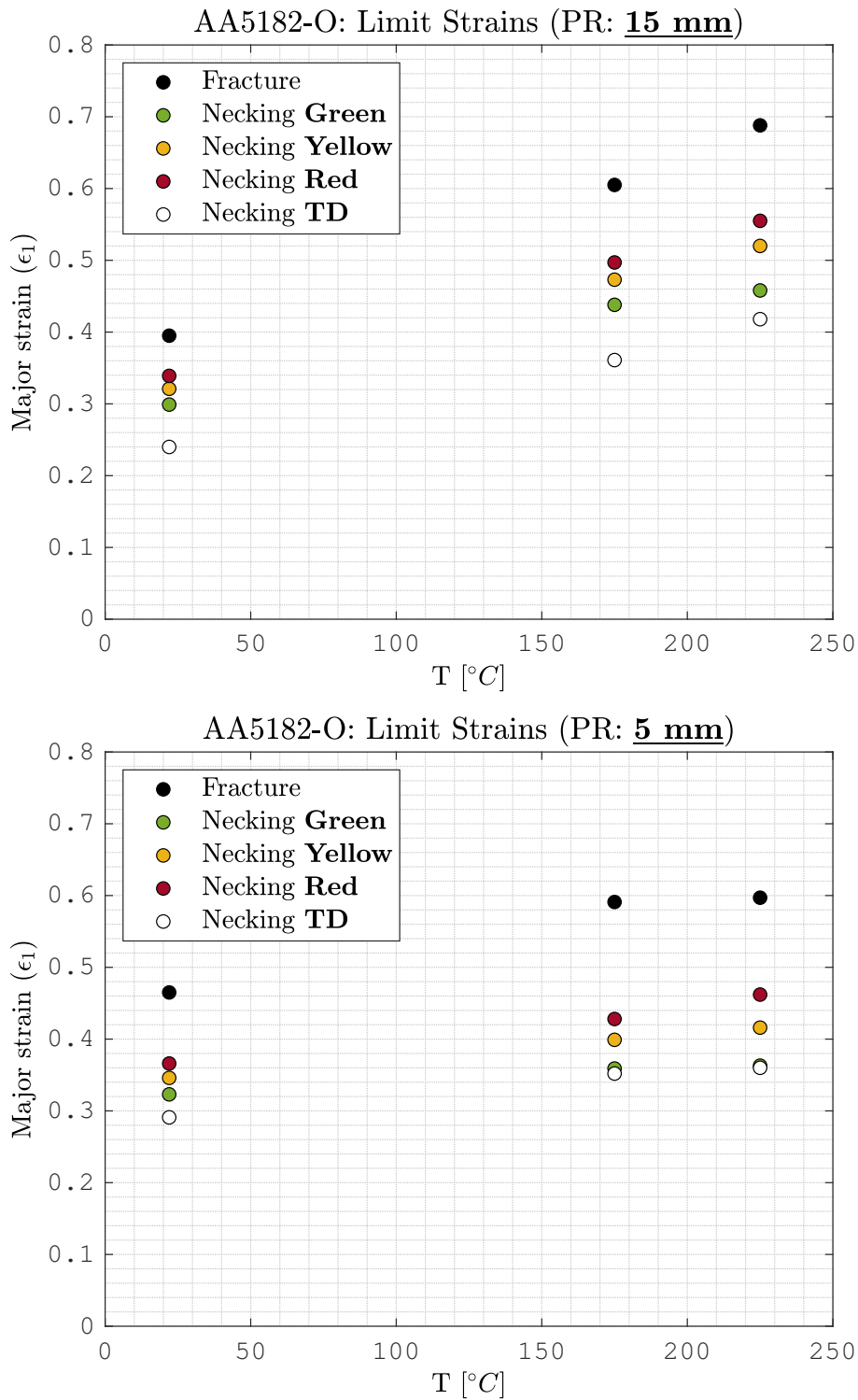


Figure 5.4: Temperature effects on AA5182-O limit strains; *top*: 15 mm punch radius, *bottom*: 5 mm punch radius. The levels of necking refer to the localization magnitude in accordance to the curvature method, from mild (green) to severe (red). "TD" refer to the time dependent method.

The AA5182-O shows increasing limit strains over the entire range of temperature, and the localized necking (assessed by the curvature method) appears at all temperatures tested. The resistance to localization improves in accordance with the raising of m -value from -0.020 at room temperature to 0.045 at 225° C. However, in the same temperature range, the n -value drops from 0.28 to 0.15¹. This change of properties makes the temperature more beneficial for severe levels of necking ("red dots") than the light levels ("green dots") since the n -value mostly affects the uniform elongation.

5.2 Curvature effects on limit strains

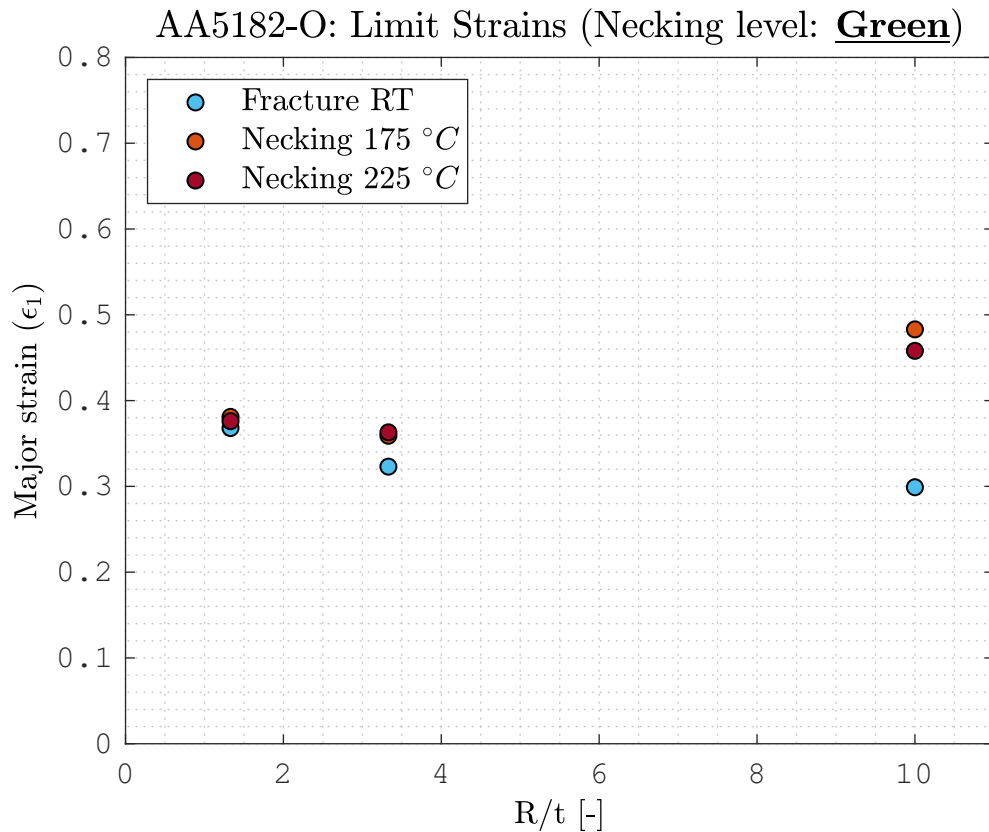


Figure 5.5: Limit strains of AA5182-O (curvature method) as a function of bend severity (R/t).

¹Strain hardening and strain rate hardening coefficients are computed from engineering stress-strain curves in 3.1.2 (van den Boogaard, 2002) after being converted to true stress-strain curves

Fig. 5.5 displays the limits strain of AA5182-O as a function of the nondimensional parameter “bend severity” R/t (thickness over ratio). The results achieved at room temperature for the AA5182-O are comparable with the results obtained by Cheong (2019). Both experiments involve the same material (same alloy, thickness and forming direction) and identical punches. The only differences are the die set and the necking detection method: Volk and Hora (time-dependent) versus curvature method. Either result shows the positive impact of curvature. In the current research, the outer surface strain at necking (green level) increases from 0.30 to 0.37 (23%) by decreasing the punch radius from 15 mm to 2 mm. Furthermore, by assuming a linear strain distribution through-thickness and applying the formula proposed by Yoshida *et al.* (2005), it is possible to compute the inner surface strain at the onset of localized necking. As regards to the 15 m, the inner strain is 0.19 (outer surface strain 0.30), which is slightly higher than the Marciniak limit strain 0.16 (Cheong, 2019). Thus, the curvature method detects with reasonable precision the onset of necking once the inner strain reaches the in-plane limit strain as predicted by the inner surface rule (Stoughton and Zhu, 2004). However, the smaller radii (2 and 5 mm) do not follow this rule. For instance, as regards to the 2 mm punch radius, the outer strain is well under the limit strain achieved by a "V-bend" test (0.37 vs. 0.55) at the sample failure, and the curvature method detects the localization before fracture. These observations should lead to localized necking as failure mechanism, but the inner surface strain never reaches the in-plane limit strain. This inconsistency may be caused by the high nonlinearity and friction effects due to low R/t ratios, as initially noticed by Stoughton and Zhu (2004). Finally, increasing the temperature appears to reverse the curvature benefits displayed at room temperature. This trend may be due to the increase of in-plane strain gradients by decreasing the punch radius, which promote the non-uniform deformation and emphasize the negative impact of the reduction of n -value at warm temperatures.

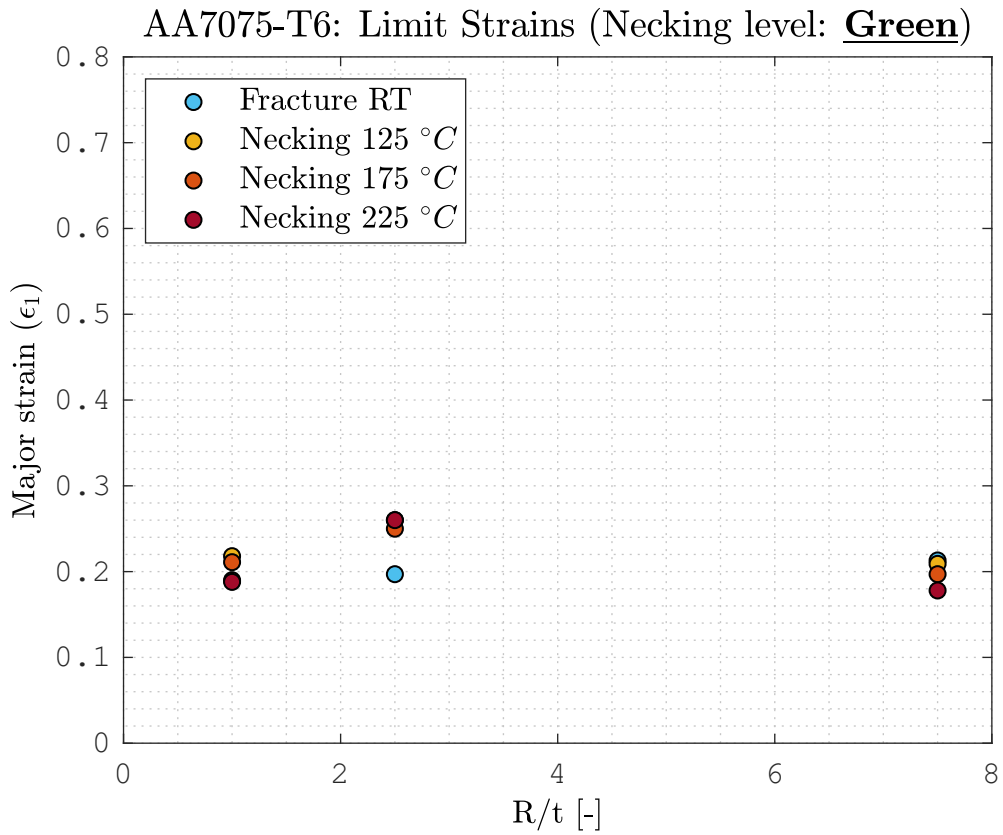


Figure 5.6: Limit strains of AA7075-T6 (curvature method) as a function of bend severity (R/t). Room temperature data refer to fracture strain since no localized necking appears.

Fig. 5.6 displays the limits strain of 7075-T6 as a function of the nondimensional parameter bend severity R/t (thickness over ratio). The room temperature data displayed in Fig. 5.6 refer to the limit strain at fracture since no necking occurs at this temperature, and they fall into a range between 0.19 and 0.21. This range is similar to the standard deviation for these measurements (0.015). Thus, the AA7075-T6 appears to be insensitive to the curvature at room temperature. However, under these conditions, the outer surface curvature increase by increasing the punch radius. This trend can be reasonable only if the specimen never fully wrap around the punch tip (the inner surface curvature never reach the punch curvature) because of the small punch displacements. In this case, the experiment fails to control the curvature. The curvature benefits can be found at warm temperatures by neglecting the 2 mm punch. Using this punch, the Teflon sheets used as lubricants result cut at the end of the repeat,

and different conditions of lubrication may affect the results.

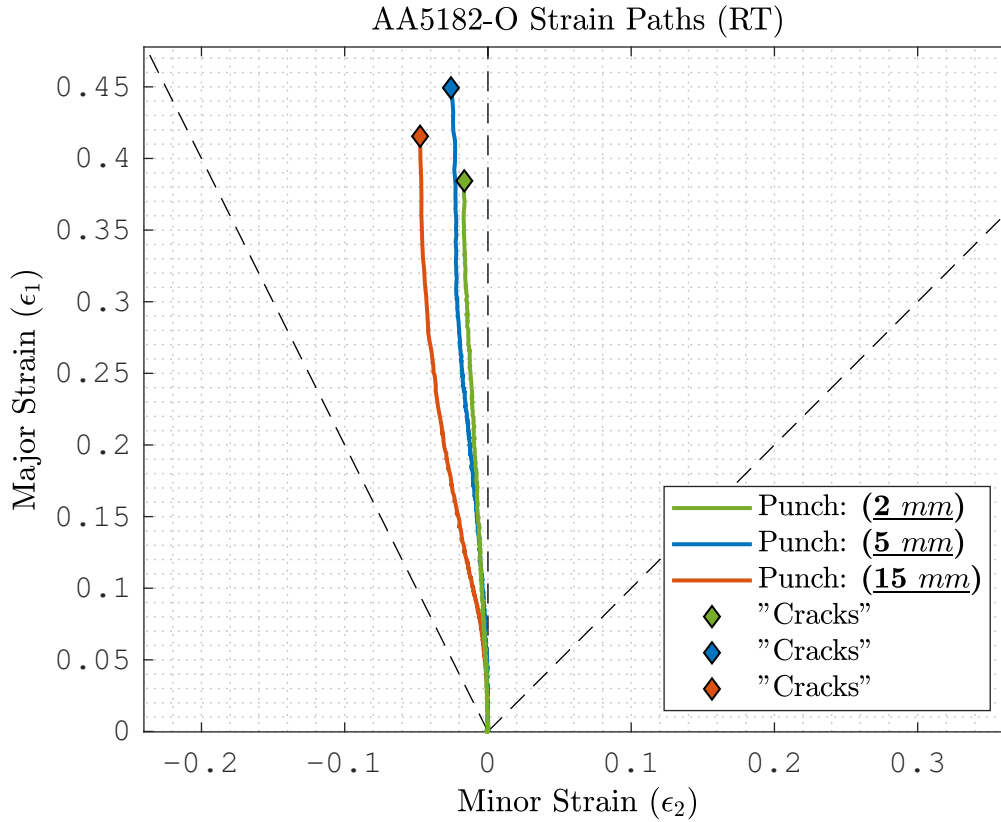


Figure 5.7: Limit strains of AA7075-T6 (curvature method) as a function of bend severity (R/t). Room temperature data refer to fracture strain since no localized necking appears.

In contrast to the temperature, the punch radius affects the strain paths, and, in turn, it affects the limit strains. Fig. 5.7 shows the comparison between strain paths under different curvature conditions, and it allows to evaluate this phenomenon. As already noticed by Cheong (2019), the bigger the radius (and the smaller the sample width), the higher the nonlinearity. This phenomenon is due to the increase of stretching component compared to bending component, which produces negative ϵ_2 (compression strains along the punch axis); thus, it moves the strain path in the drawing region.

The effects of strain paths are neglected. However, the equivalent strains are computed using the Eq. 5.1 in order to compare the limit strains with different

ϵ_2/ϵ_1 ratios.

$$\epsilon_{eq} = \frac{2}{\sqrt{3}} \cdot \sqrt{\epsilon_1^2 + \epsilon_2^2 + 2\epsilon_1\epsilon_2} \quad (5.1)$$

The equivalent strain lowers the strain states in the drawing region, and it makes the results more comparable with the plane strain condition (weakest forming condition). The results of this analysis are displayed in Fig. 5.8 and Fig. 5.9. The trend previously described are confirmed for both alloys.

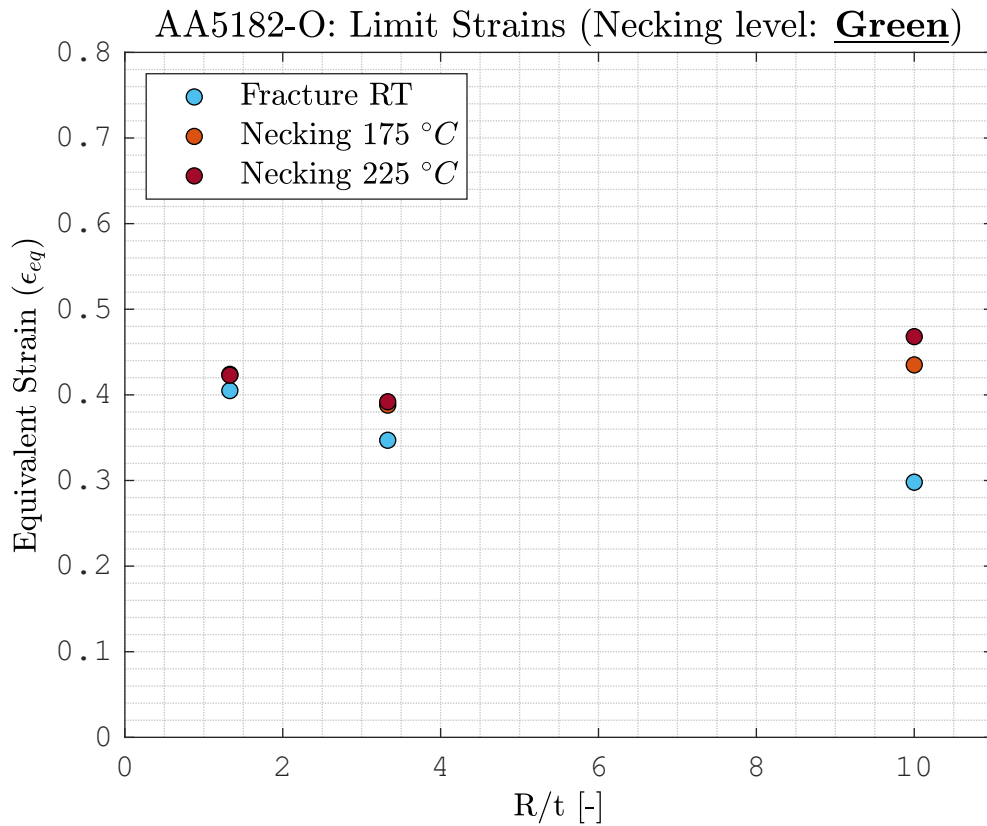


Figure 5.8: Equivalent limit strains of AA5182-O (curvature method) as a function of bend severity (R/t).

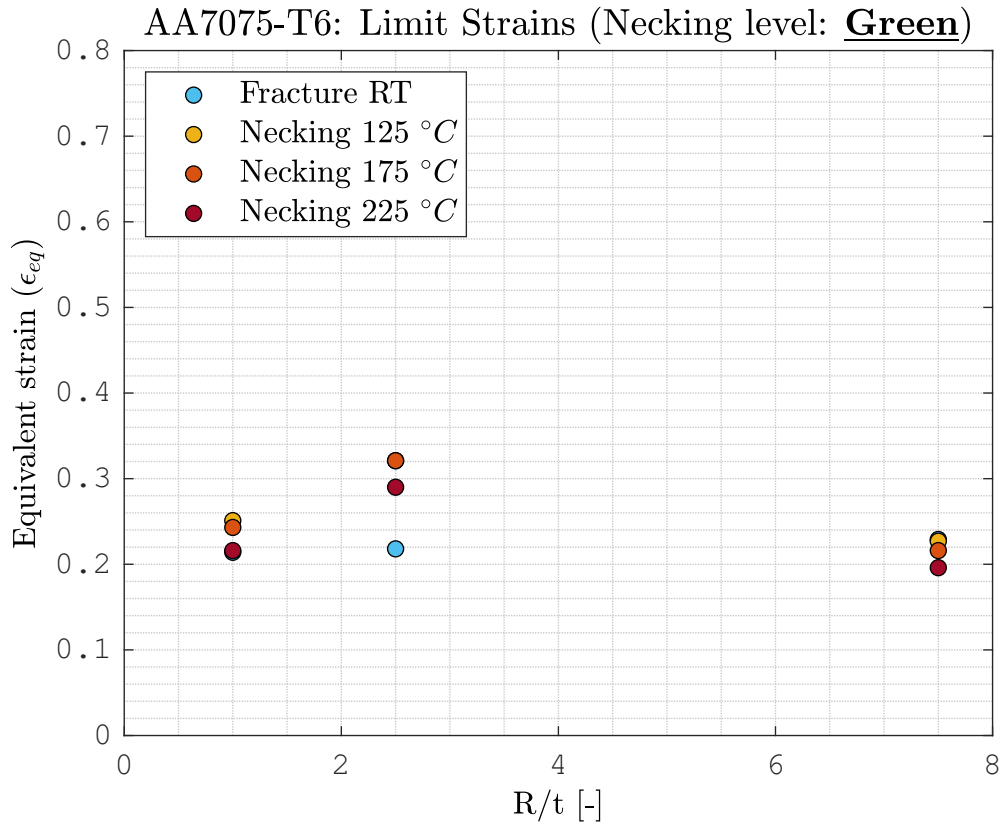


Figure 5.9: Equivalent limit strains of AA7075-T6 (curvature method) as a function of bend severity (R/t).

5.3 Temperature and curvature effects on punch displacement.

The limit strains analyzed so far are extracted from a circle of diameter around 1 mm; thus, they are a local observation of sample deformation. On contrary punch displacement depends more on the sum of strains recorded on the sample surface, rather than the maximum strain. So, punch displacement is closely related to the overall deformation of the blank. Fig. 5.10 displays the results for the AA5182-O as a function of temperature (top) and curvature (bottom). The resulting displacements values are extracted from the DIC measurements.

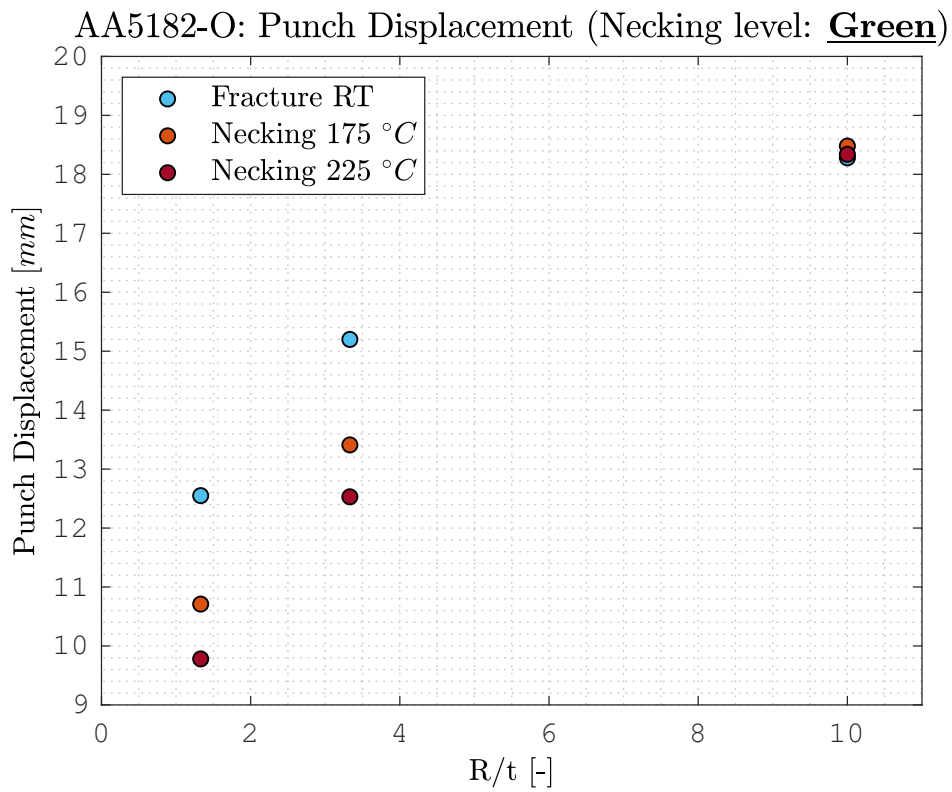
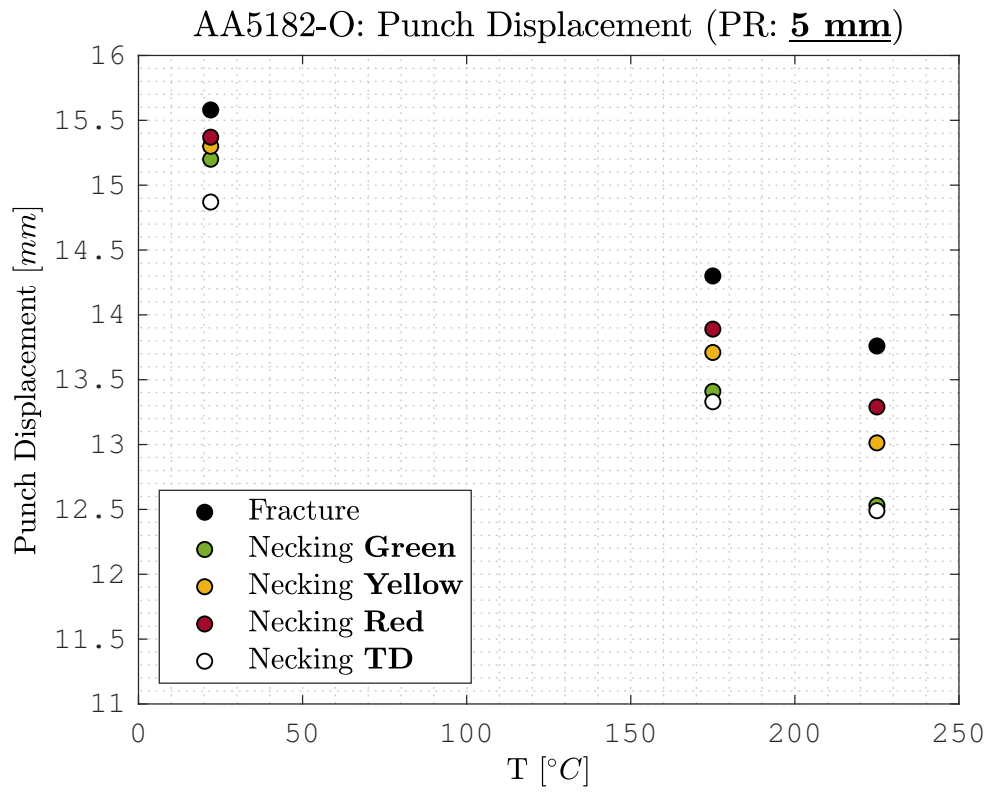


Figure 5.10: Temperature (*top*) and curvature (*bottom*) effects on AA5182-O punch displacement.

The punch displacement decreases by increasing the curvature as a result of a higher localization of deformation at the punch tip. Mostly, the punch displacement decrease by increasing the temperature at small radius (2 mm and 5 mm). This trend may result from a willingness to strain localization caused by temperature. This localization may occur at low radii when the strain gradients on the sample surface are higher because of the higher friction forces between the punch and the specimen. Despite the temperature positively affects the limit strain, under these conditions (low radius, high temperature), the average strain on the sample surface decrease, reducing the displacement. This phenomenon may be due to the sharp drop of n -value at warm temperatures, which anticipates the onset of localized necking and promotes the localization. In the post uniform elongation, the improvements in strain rate sensitivity (m -value) begin, delaying the development of necking and achieving higher strain states in the necked section.

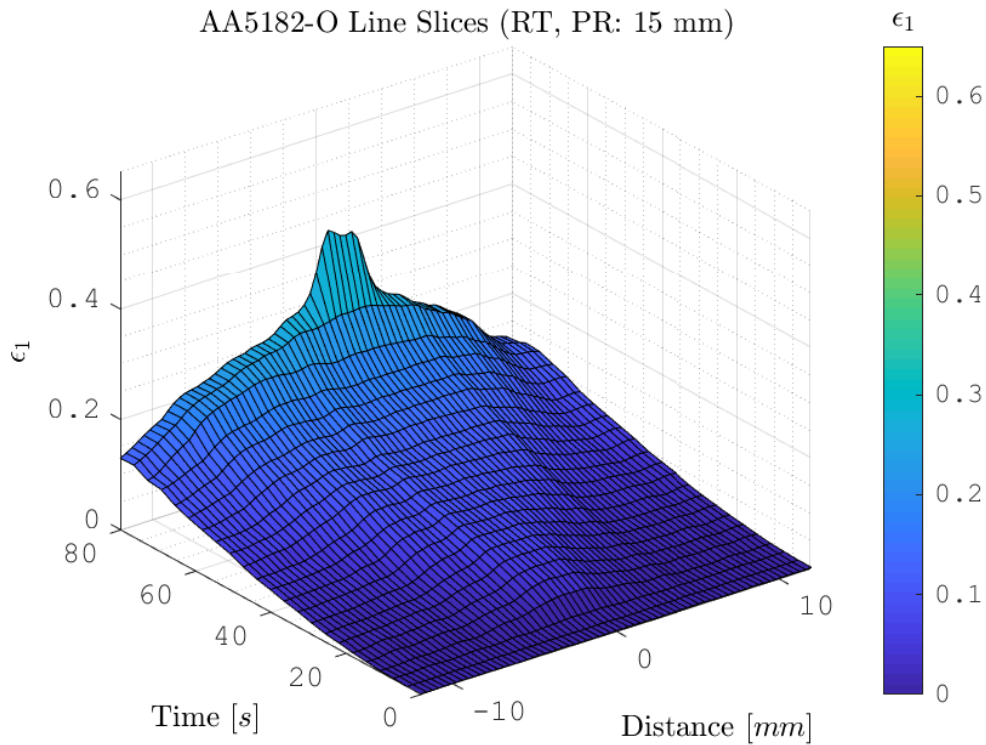


Figure 5.11: Line-slices surface plot AA5182-O (RT, PR: 15 mm)

In an attempt to further investigate the punch displacement results, the “line-slice” strain data are analyzed. In Fig. 5.11, the surface plot represents the strain data extracted over a line perpendicular to ϵ_1 and 24 mm long (x -axis) centered at the highest strain value recorded at failure ($x = 0$, $y = \max \implies \epsilon_1$ at "fracture"). Then, the development of strains is observed in time (y -axis). At $y = 0$ (time=0 s), the sample is undeformed, and the strains are equal to zero over the entire line-slice. Strains increase and gradually concentrate in $x = 0$ as deformation proceeds, indicating the phenomenon of localization. The same considerations can be done on Fig. 5.12, Fig. 5.13 and Fig. 5.14, for different testing conditions. In these surface plots, the peak is the limit strain at failure, the volume subtended by the surface is related to the punch displacement.

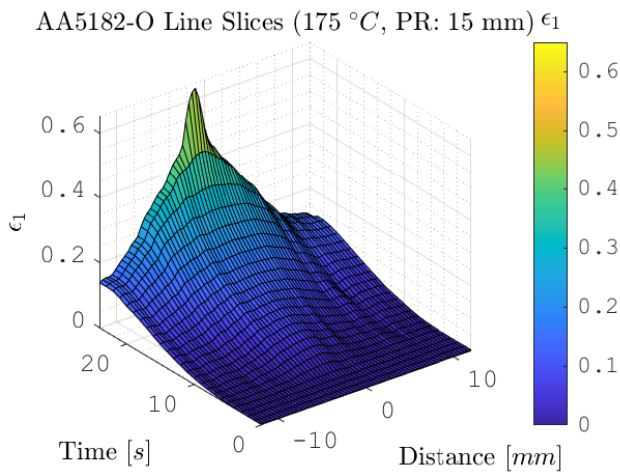


Figure 5.12: Line-slices surface plot AA5182-O (175 °C, PR: 15 mm)

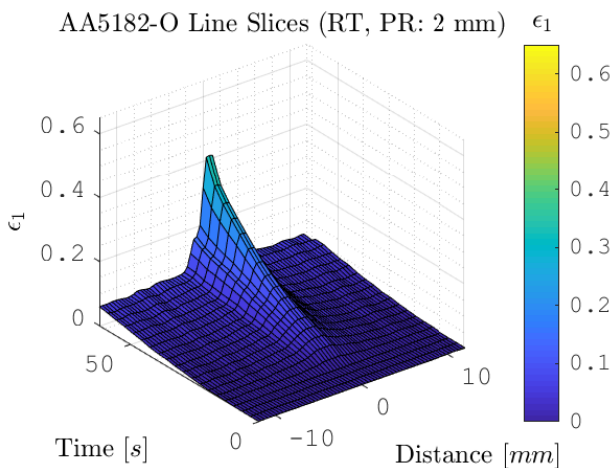


Figure 5.13: Line-slices surface plot AA5182-O (RT, PR: 2 mm)

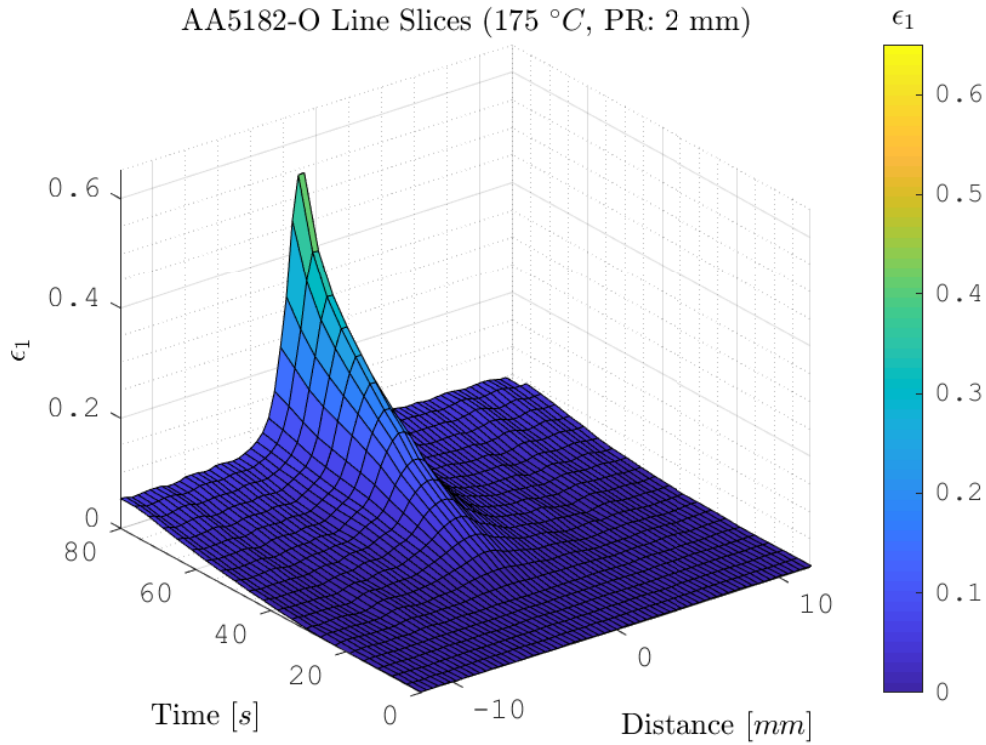


Figure 5.14: Line-slices surface plot AA5182-O (175 °C, PR: 2 mm)

The curvature effect on strain distribution is apparent by considering Fig. 5.11 and Fig. 5.13. The peaks are similar in both surfaces (they are not the limit strains at the onset of localized necking shown in Section 5.2, but the highest strains recorded on the sample surface before fracture). However, the strain distribution in the final stage of deformation is different. Using the 2 mm punch, strains focus in the necked section ($x = 0$), and the bottom of the surface is significantly lower. Thus, the 2 mm punch produces a lower volume below the "strain surface."

Temperature appears to have similar impacts on limit strains, but less pronounced. A more accurate way of highlighting this phenomenon is to subtract the surface of Fig. 5.13 to the surface of Fig. 5.14 (before performing the subtraction, the surfaces need to be aligned, by making the peaks coincident). In other words, the temperature effect is more visible by considering the distributions of $\Delta\epsilon_1$ (delta of major strains) at constant punch radius.

Fig. 5.15 shows the result of this operation for AA5182-O. The peak strain is higher at 175 °C than RT since $\Delta\epsilon_1$ is positive ($\Delta\epsilon_1 = 0.12$). However, the benefit of temperature affects a small portion of the sample surface within the necked section. In most of the remaining parts of the specimen, $\Delta\epsilon_1$ is negative (dark blue). Although this analysis does not take into account the entire specimen surface, a negative impact on the strain distribution appears clear. The volume below the surface may decrease by increasing the temperature, resulting in a lower punch displacement.

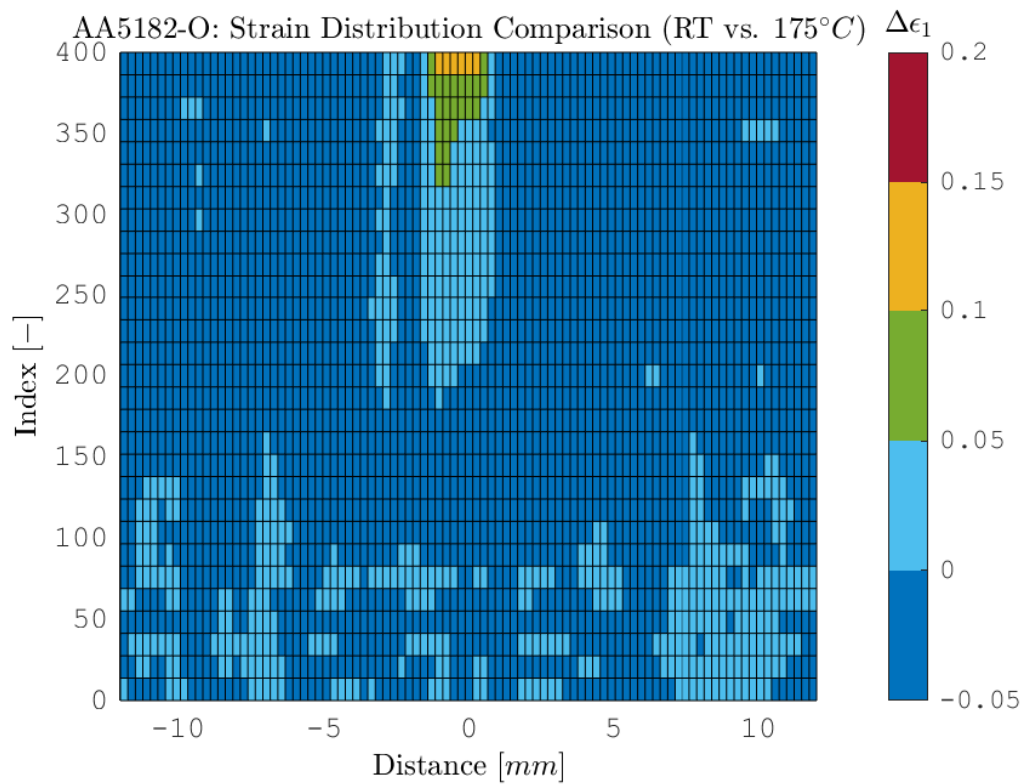


Figure 5.15: Comparison of strain distributions recorded on sample surface: RT vs. 175 °C (AA5182-O, punch: 2 mm). Index is for better readability ($Index = 0 \implies$ test begins, $Index = 400 \implies$ test ends) since testing times depend on testing conditions and they lose meaning during the alignment of surfaces.

The same procedure is repeated on AA7075-T6 data obtained using the 5 mm punch, and Fig. 5.16 displays the results. The reduction of dark blue areas (negative $\Delta\epsilon_1$) is apparent. In contrast to AA5182-O, the temperature benefits appear to involve both the necked ($\Delta\epsilon_1 = 0.2$) and surrounding areas.

This result may indicate an increase in punch displacement by raising the temperature from RT to 175 °C. Fig. 5.17 confirms this assumption.

The opposite trend to AA5182-O may be due to the low n -value at RT of AA7075-T6. This property makes the deformation of AA7075-T6 more dependent on strain rate hardening than strain hardening, and it makes less apparent the reduction of uniform deformation (n -value) at warm temperatures. In other words, strains are focused in the mid section of the sample even at RT (Fig. 5.18); therefore, the punch displacement is mostly related to the behavior of the necked section, and in turn to m -value. Increasing the temperature from RT to 175 °C increases the peak of strain surface (Fig. 5.19), and the punch displacement. Above 175 °C, the punch displacement decreases as a consequence of the loss of mechanical properties (Section 5.1), which in turn, lower limit strains.

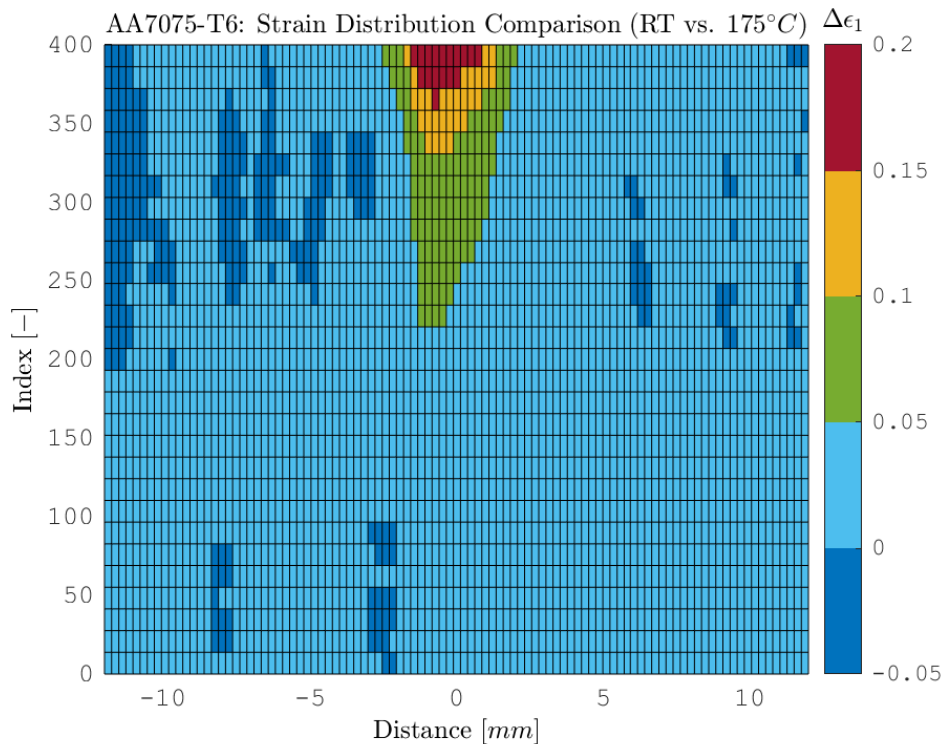


Figure 5.16: Comparison of strain distributions recorded on sample surface: RT vs. 175 °C (AA7075-T6, punch: 5 mm). Index is for better readability ($Index = 0 \implies$ test begins, $Index = 400 \implies$ test ends) since testing times depend on testing conditions and they lose meaning during the alignment of surfaces.

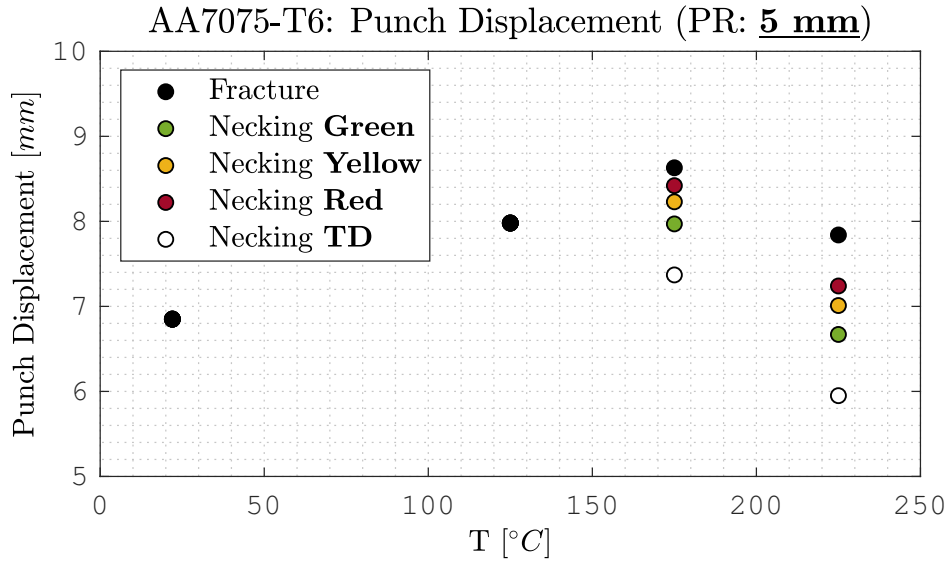


Figure 5.17: Temperature effects on AA7075-T6 punch displacement.

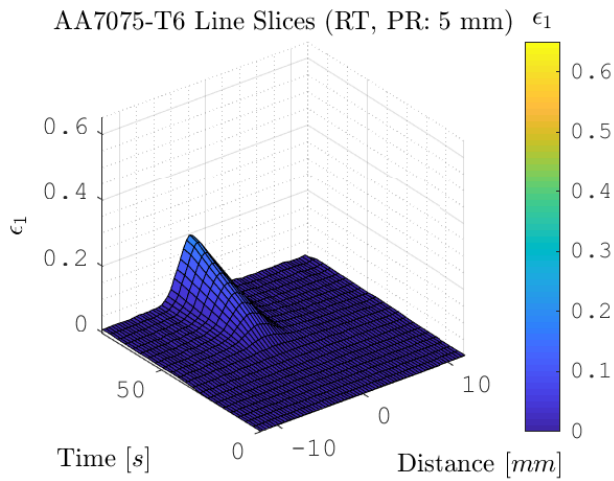


Figure 5.18: Line-slices surface plot 7075-T6 (RT, PR: 5 mm)

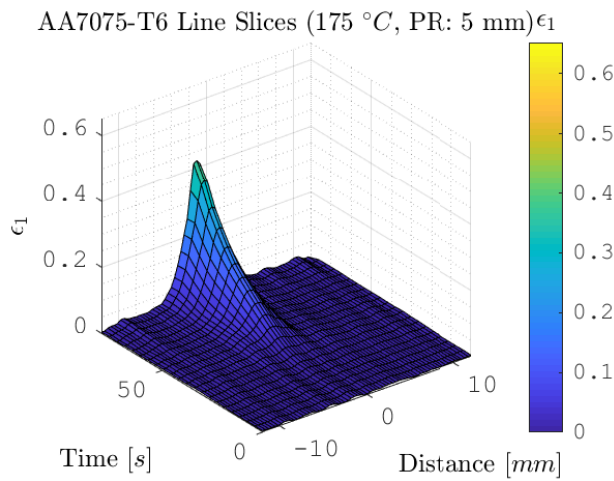


Figure 5.19: Line-slices surface plot AA7075-T6 (175 °C, PR: 5 mm)

Chapter 6

Conclusions

Throughout the thesis, several aspects related to a new stretch-bending experiment at warm temperatures have been investigated.

- The experiment met the main requirements successfully: the room temperature dies produced the sample failure at the punch tip (where the stretch bending states occur), and the heating system produced uniform temperatures on the sample surface. Furthermore, the standard deviation resulted lower than 0.015 in 65% of the conditions tested. This repeatability produced an average interval of confidence (95% of reliability, T-student distribution) of ± 0.02 as regards limit strains. Finally, no evidence of buckling due to thermal dilatancy were noticed during the pre-heating phase of the sample. However, some issues (which may have affected both results and repeatability) were encountered under some testing conditions. All tests are carried out under the same condition of lubrication except for the AA7075-T6 at RT and 125 °C using the 2 mm punch. Under these conditions, the Teflon placed in between the punch and the specimen turn out broken after the test. A little bump in the load-displacement curve also highlights this phenomenon, and it means that these tests are carried out without lubricants, which may have affected the results. As regards the AA7075-T6 at low temperatures, the sudden fracture prevented the onset of fracture from being detected. For this reason, it is challenging to state safely if fracture starts in the

middle (plane strain conditions) or the edge (uniaxial strain conditions). Finally, as regards the AA5182-O under high stretch bend strains (high temperature and 2 *mm* punch), the failure frame is challenging to detect. The unambiguous fracture appears many images later the appearance of the first “shining lines.” These lines may not indicate the failure of the sample, but the fracture of the paint which exposes the shiny metal. If this were the case, assuming the fracture strain as the strain recorded at the frame, which precedes the first appearance of “shining lines,” would be too conservative. However, strains recorded in the following frames are less reliable since the reflections affect the DIC analysis. For these tests, fracture strains are obtained, looking at the strain paths. In particular, the fracture strain is the last strain recorded before “anomalous” variations of ϵ_1 and ϵ_2 from the path. This method is more user-dependent than selecting the maximum strain in the frame, which precedes the fracture.

- The designed tools work correctly, and no thermal paste was needed to improve thermal conductivity. The DIC measurements showed a recurrent slight inclination of punch axis, which may be caused by the punch holder (one end of the punch appears 0.1 *mm* higher than the opposite one). However, this defect does not affect the failure location.
- The thermal simulation successfully predicted the uniform temperature of sample surface. The thermal gradients in the punch confirm the sidewall as a right control spot for temperatures. The most significant temperature drop was recorded between the bottom and the tip of the punch. Temperature is almost uniform along the punch axis.
- The curvature method highly depends on the threshold values used to define the necking severity. The values used in this thesis appeared to overestimate the limit strains compared to the time-dependent method in most of the testing conditions.
- Temperature is found to have positive effects on AA5182-O limit strains,

whereas results for the AA7075-T6 lead to the conclusion that an optimum forming temperature exists between 175 °C and 225 °C. Curvature benefits in delaying the localized necking confirm previous results for the AA5182-O at room temperature. However, the relationship between punch radius and limit strains is reversed at warm temperatures, and increasing the curvature impacts negatively on limit strains. As regards to the AA7075-T6, curvature appears beneficial at warm temperatures, but low punch displacements prevent from getting reliable results at room temperature. Finally, a close look at punch displacements shows a possible negative aspect of warm forming. As regards to the AA5182-O, punch displacement decrease by increasing the temperature. This phenomenon may be due to the decrease of strain hardening, which reduces the uniform elongation. In contrast, the punch displacement of AA7075-T6 increase increasing the temperature until 175 °C, probably because of the smaller reduction of n -value compared to the AA5182-O.

Bibliography

- Atzema, E. (2017). Formability of auto components. In *Automotive Steels*, chapter 3.5.1. Elsevier.
- Ayres, R. A. and Wenner, M. L. (1979). Strain and strain-rate hardening effects in punch stretching of 5182-0 aluminum at elevated temperatures. *Metallurgical Transactions A*, **10**(1), 41–46.
- Banhart, J. (2016). Metallurgy of heat treatable aluminum alloys. In *ASM Handbook*, volume 4E, Heat Treating of Nonferrous Alloys, pages 214–239. ASM International.
- Bergström, Y. (1983). The plastic deformation of metals—a dislocation model and its applicability. *Rev. Powder Metall. Phys. Ceram.*, **2**(2), 79–265.
- Bolt, P., Lamboo, N., and Rozier, P. (2001). Feasibility of warm drawing of aluminium products. *Journal of Materials Processing Technology*, **115**(1), 118–121.
- Charpentier, P. L. (1975). Influence of punch curvature on the stretching limits of sheet steel. *Metallurgical and Materials Transactions A*, **6**(8), 1665–1669.
- Cheong, D.-W. K. (2019). *On the Influence of the Through-Thickness Strain Gradients for Characterization of Formability and Fracture of Sheet Metal Alloys*. Master’s thesis, University of Waterloo.
- Cheong, K., Butcher, C., and Dykeman, J. (2018). The influence of the through-thickness strain gradients on the fracture characterization of advanced high-strength steels. *SAE International Journal of Materials and Manufacturing*, **11**(2018-01-0627), 541–552.

- DiCecco, S., Butcher, C., Worswick, M., Boettcher, E., Chu, E., and Shi, C. (2016). Determination of forming limit diagrams of aa6013-t6 aluminum alloy sheet using a time and position dependent localized necking criterion. In *IOP Conference Series: Materials Science and Engineering*, volume 159, page 012009. IOP Publishing.
- EAA (2013). Aluminium in cars. unlocking the light-weight potential. *European Aluminium Association*.
- Graf, A. and Hosford, W. (1993). Effect of changing strain paths on. *Metallurgical transactions A*, **24**(11), 2503.
- Gupta, R., Mathew, C., and Ramkumar, P. (2015). Strain hardening in aerospace alloys. *Frontiers in Aerospace Engineering*, **4**(1), 1–13.
- Hecker, S. S. (1972). A simple forming-limit curve technique and results on aluminum alloys. In *Int. Deep Drawing Res. Group, 7 th Biennial Congress, Amsterdam. 1972*, 35.
- Hirsch, J. (1997). Aluminium alloys for automotive application. In *Materials Science Forum*, volume 242, pages 33–50. Trans Tech Publ.
- Hui, W., LUO, Y.-b., Friedman, P., CHEN, M.-h., and Lin, G. (2012). Warm forming behavior of high strength aluminum alloy aa7075. *Transactions of Nonferrous Metals Society of China*, **22**(1), 1–7.
- Huo, W., Hou, L., Zhang, Y., and Zhang, J. (2016). Warm formability and post-forming microstructure/property of high-strength aa 7075-t6 al alloy. *Materials Science and Engineering: A*, **675**, 44–54.
- ICCT (2019). Emission standards for passenger cars and light-commercial vehicles in the european union. *International Council on Clean Transportation*.
- Ivanoff, T. A., Taleff, E. M., and Hector, L. G. (2015). Warm forming of aa7075-t6 with direct electrical resistance heating. In *Light Metals 2015*, pages 223–227. Springer.

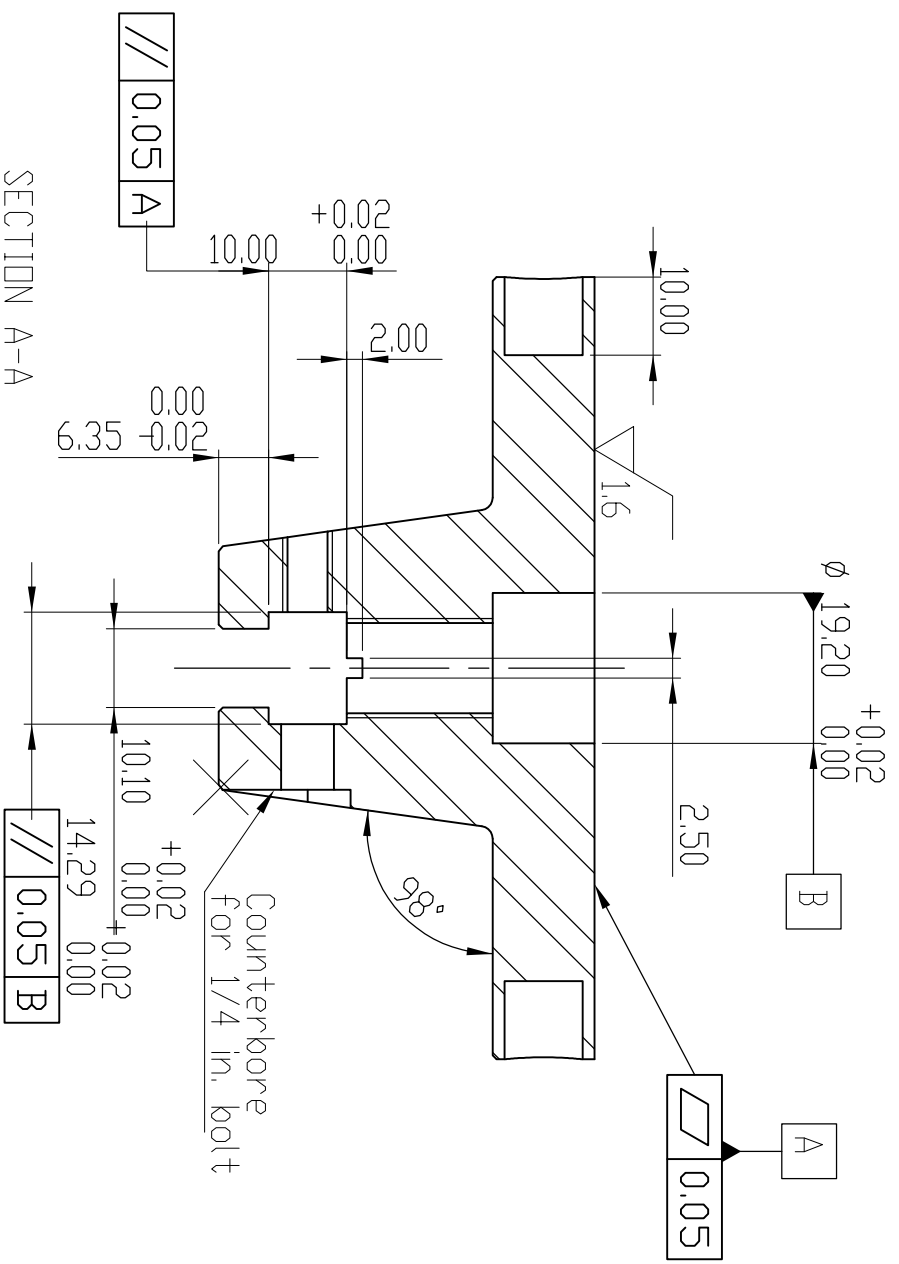
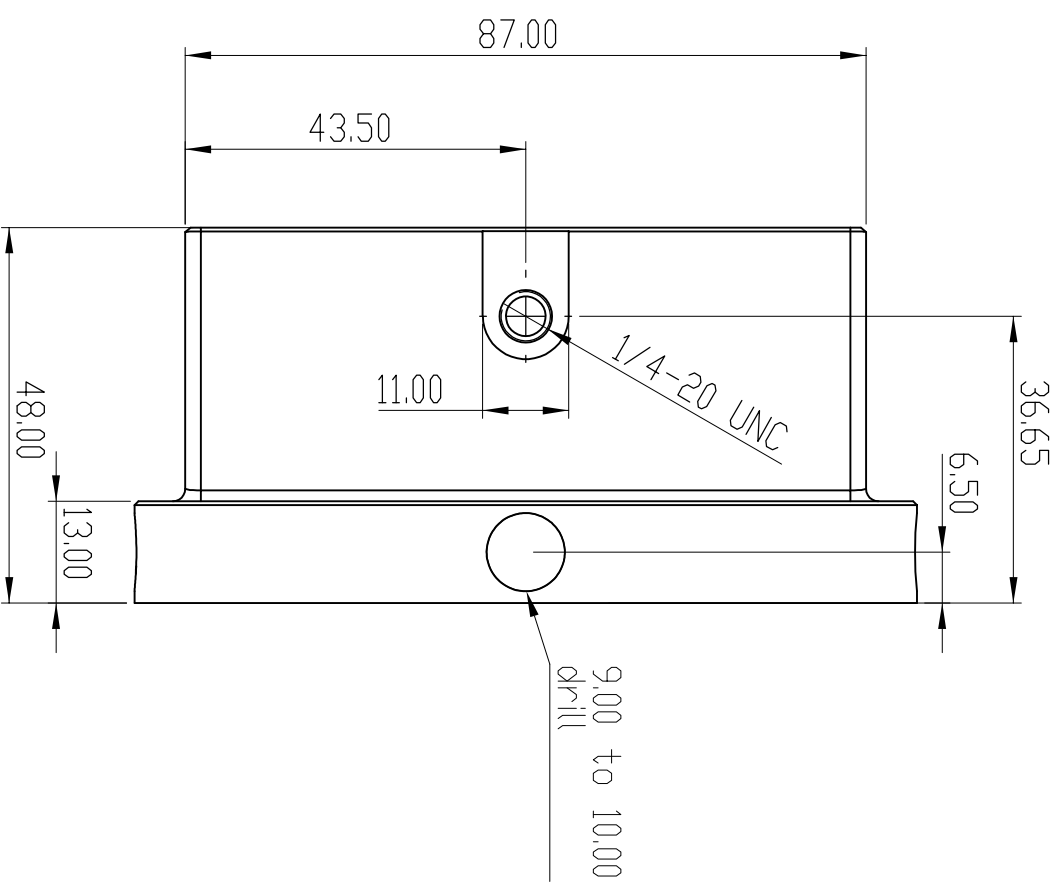
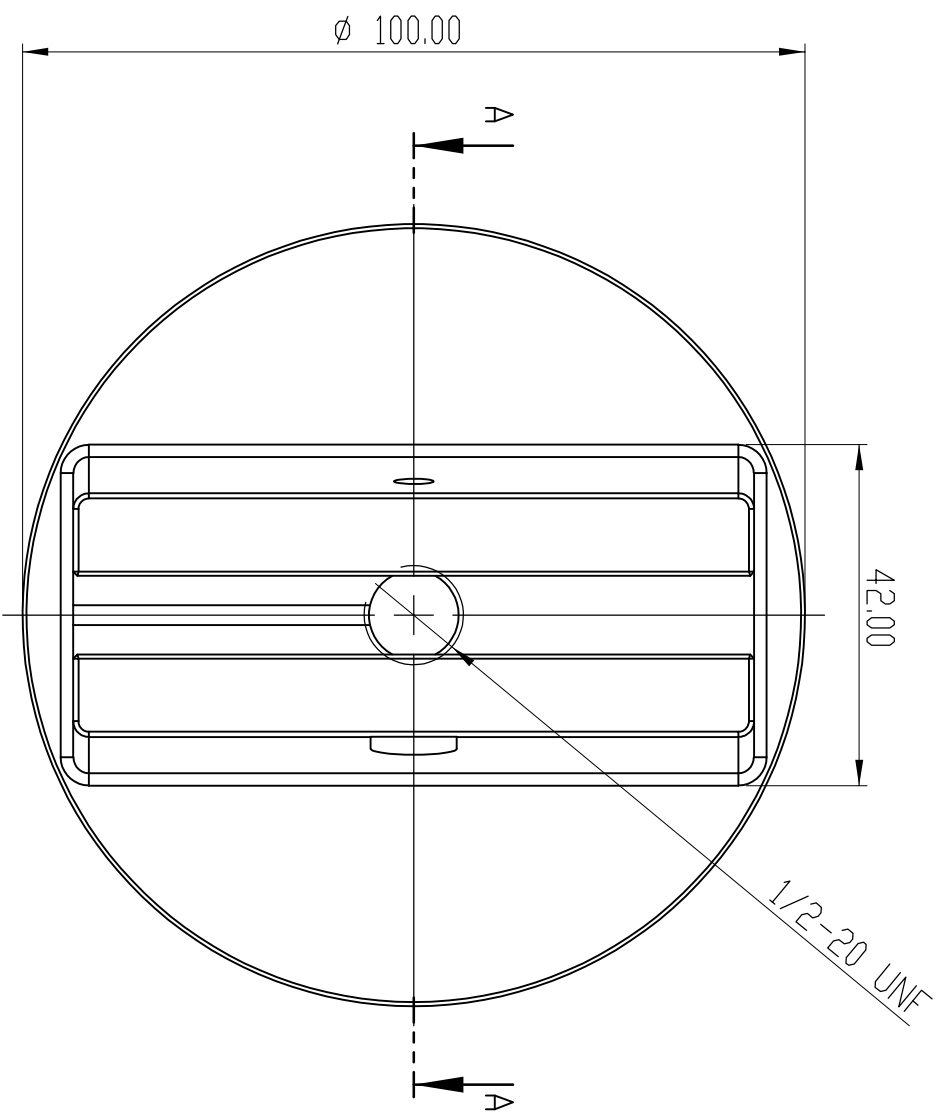
- Keeler, S. (1978). Forming limit criteria—sheets. In *Advances in deformation processing*, pages 127–157. Springer.
- Kurukuri, S. (2010). *Simulation of the thermally assisted forming of aluminum sheet*. Ipskamp Drukkers.
- Leotoing, L., Guines, D., Zidane, I., and Ragneau, E. (2013). Cruciform shape benefits for experimental and numerical evaluation of sheet metal formability. *Journal of Materials Processing Technology*, **213**(6), 856–863.
- Li, D. and Ghosh, A. (2003). Tensile deformation behavior of aluminum alloys at warm forming temperatures. *Materials Science and Engineering: A*, **352**(1-2), 279–286.
- MacKenzie, D. S. (2016a). Metallurgy of heat treatable aluminum alloys. In *ASM Handbook*, volume 4E, Heat Treating of Nonferrous Alloys, pages 114–136. ASM International.
- MacKenzie, D. S. (2016b). Metallurgy of heat treatable aluminum alloys. In *ASM Handbook*, volume 4E, Heat Treating of Nonferrous Alloys, pages 65–113. ASM International.
- Marciniak, Z. and Kuczyński, K. (1967). Limit strains in the processes of stretch-forming sheet metal. *International journal of mechanical sciences*, **9**(9), 609–620.
- Martínez-Donaire, A., García-Lomas, F., and Vallellano, C. (2014). New approaches to detect the onset of localised necking in sheets under through-thickness strain gradients. *Materials & Design*, **57**, 135–145.
- Min, J., Stoughton, T. B., Carsley, J. E., and Lin, J. (2016). Compensation for process-dependent effects in the determination of localized necking limits. *International Journal of Mechanical Sciences*, **117**, 115–134.
- Naka, T., Torikai, G., Hino, R., and Yoshida, F. (2001). The effects of temperature and forming speed on the forming limit diagram for type 5083

- aluminum–magnesium alloy sheet. *Journal of Materials Processing Technology*, **113**(1-3), 648–653.
- Nakazima, K., Kikuma, T., and Hasuka, K. (1968). Study on the formability of steel sheets. *YAWATA TECH REP, SEPT. 1968, -264-, 8517-8530*.
- Noder, J. and Butcher, C. (2019). A comparative investigation into the influence of the constitutive model on the prediction of in-plane formability for nakazima and marciniak tests. *International Journal of Mechanical Sciences*, **163**, 105138.
- Novotny, S. and Geiger, M. (2003). Process design for hydroforming of lightweight metal sheets at elevated temperatures. *Journal of Materials Processing Technology*, **138**(1-3), 594–599.
- Scallan, P. (2003). *Process planning: the design/manufacture interface*. Elsevier.
- Sotirov, N., Simon, P., Chimani, C., Uffelmann, D., and Melzer, C. (2012). Warm deep drawability of peak-aged 7075 aluminium sheet alloy. In *Key Engineering Materials*, volume 504, pages 955–960. Trans Tech Publ.
- Stoughton, T. B. and Yoon, J. W. (2011). Paradigm change: alternate approaches to constitutive and necking models for sheet metal forming. In *AIP conference proceedings*, volume 1383, pages 15–34. AIP.
- Stoughton, T. B. and Zhu, X. (2004). Review of theoretical models of the strain-based fld and their relevance to the stress-based fld. *International Journal of plasticity*, **20**(8-9), 1463–1486.
- Swift, H. (1952). Plastic instability under plane stress. *Journal of the Mechanics and Physics of Solids*, **1**(1), 1–18.
- Takata, K. (2013). Warm forming of aluminum alloys. *Nippon Steel Technical Report*, (103).
- Tharrett, M. R. and Stoughton, T. B. (2003). Stretch-bend forming limits of 1008 ak steel. Technical report, SAE Technical Paper.

- Tisza, M. and Czinege, I. (2018). Comparative study of the application of steels and aluminium in lightweight production of automotive parts. *International Journal of Lightweight Materials and Manufacture*, **1**(4), 229–238.
- van den Boogaard, A. (2002). *Thermally enhanced forming of aluminium sheet*. Ponsen & Looijen.
- van den Boogaard, A. H., Bolt, P., and Werkhoven, R. (2001). Aluminum sheet forming at elevated temperatures. *Simulation of Materials Processing: Theory, Method and Applications*, pages 819–824.
- Volk, W. and Hora, P. (2011). New algorithm for a robust user-independent evaluation of beginning instability for the experimental FLC determination. *International journal of material forming*, **4**(3), 339–346.
- Yoshida, M., Yoshida, F., Konishi, H., and Fukumoto, K. (2005). Fracture limits of sheet metals under stretch bending. *International Journal of Mechanical Sciences*, **47**(12), 1885–1896.
- Zhang, C., Chu, X., Guines, D., Leotoing, L., Ding, J., and Zhao, G. (2014). Effects of temperature and strain rate on the forming limit curves of AA5086 sheet. *Procedia Engineering*, **81**, 772–778.

Appendix A

Punch holder drawing



CHAMFERS: 0.5X 45°

DIMENSIONS ARE IN MILLIMETERS
 TOLERANCES:
 LINEAR: ± 0.2
 ANGULAR: ± 0.5°

SURFACE FINISH:
 √3.2

DO NOT SCALE DRAWING

REVISION

TITLE:

Punch holder

DATE: 2019-10-16

MATERIAL: STEEL

DWG NO:

A3

NAME

SIGNATURE

CHK'D

APPV'D

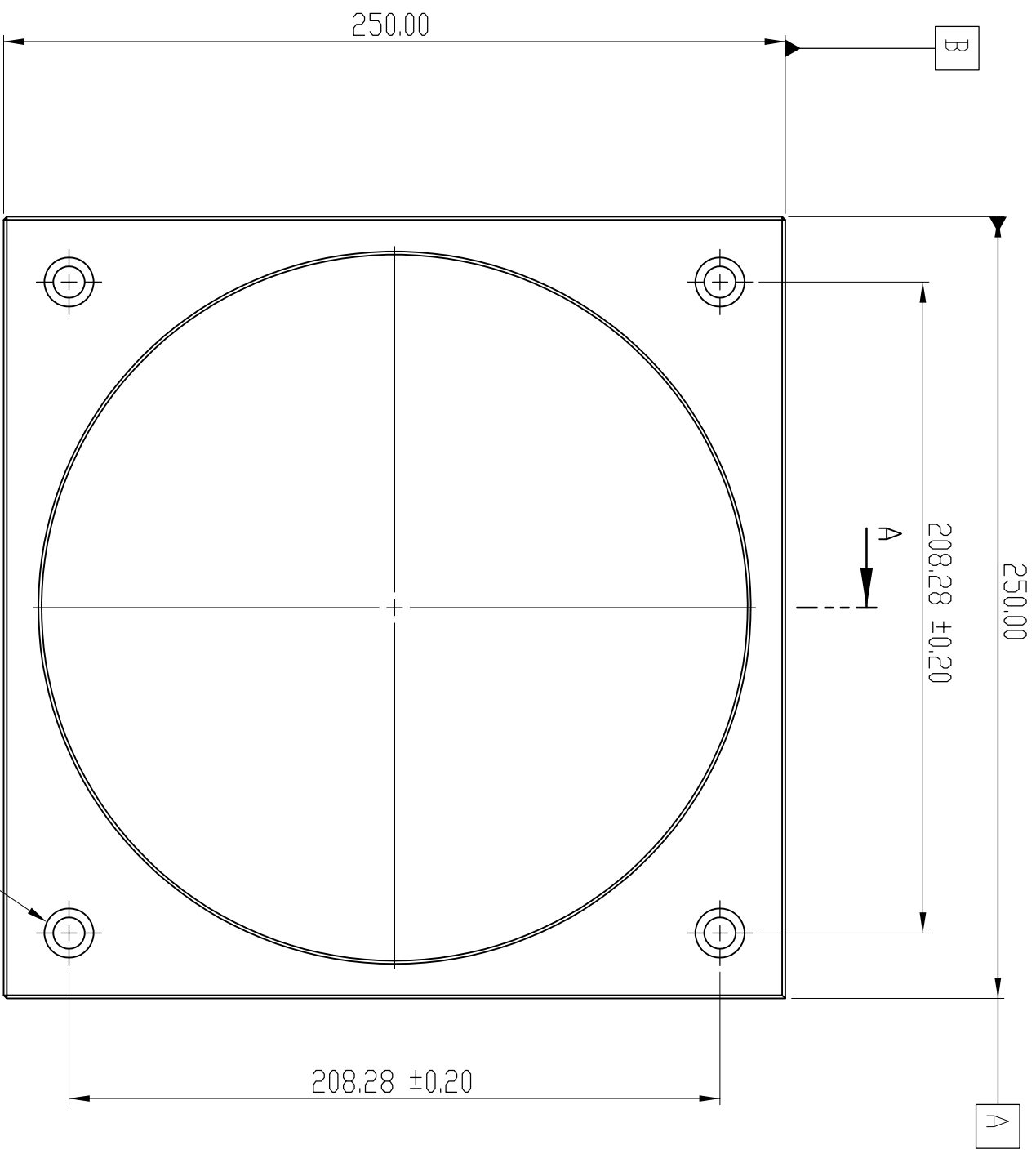
MFG

QA

SCALE:1:1

Appendix B

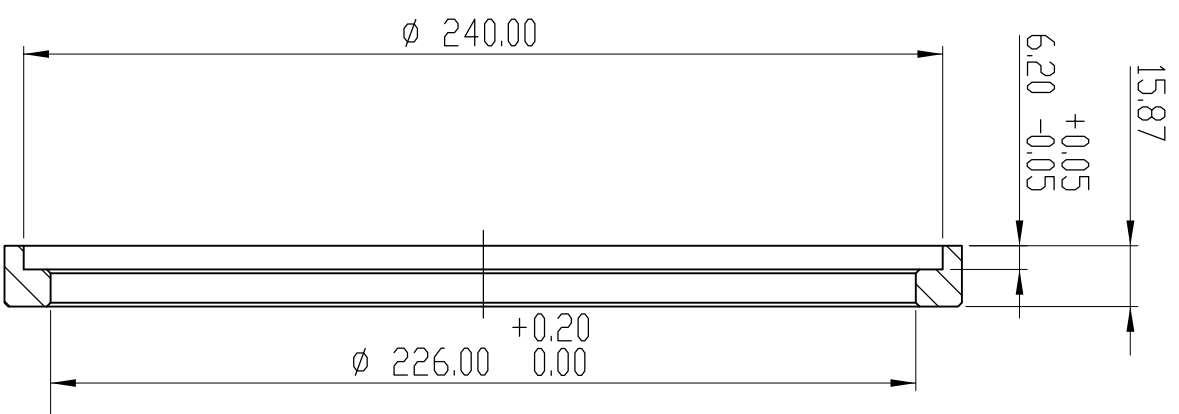
Clamping plate drawing



4 X ϕ 10.08 THRU ALL
 ϕ 15.88 ∇ 9.53

ϕ 0.2 A B

CHAMFERS: 1x45 °



ϕ 0.2 A B

SECTION A-A

DIMENSIONS ARE IN MILLIMETERS
 TOLERANCES:
 LINEAR: ± 0.5
 ANGULAR: $\pm 1^\circ$

SURFACE FINISH:
 $\sqrt{3.2}$

NAME	SIGNATURE	DATE
DRAWN		2019-10-16
CHK'D		
APPV'D		
MFG		
QA		

MATERIAL:
 COLD ROLLED STEEL

DO NOT SCALE DRAWING

REVISION

TITLE:
 Clamping ring

DWG NO. A3

SCALE: 1:2

Appendix C

MATLAB scripts

Curvature method:

```
clear all;
close all;
clc;

%% READ .xlsx FILE %%
cyy=zeros(2000,1);
e1=zeros(2000,1);
e2=zeros(2000,1);
time=zeros(2000,1);

fileName='AA5182-O-RD-Med-Gap-15mm-025mms-1_circ_1.xlsx';
xlRange='L3:L2000';
cyy=xlsread(fileName,xlRange); %principal curvature
xlRange='I3:I2000';
e1=xlsread(fileName,xlRange); %major strain
xlRange='J3:J2000';
e2=xlsread(fileName,xlRange); %minor strain
xlRange='Q3:Q2000';
time=xlsread(fileName,xlRange); %analog time

cyy(cyy==0)=[];
e1(e1==0)=[];
e2(e2==0)=[];

%% DATA AND PARAMETERS %%
N=1000; %number of points in linspace fitting range;
start=round(0.1*length(e1)+1,0); %offset of fitting interval
yDev=0.001; %y-value of right end point of s. line fitting range
greenDev=0.005; %deviation from straight line (green)
```

```

yellowDev=0.01; %deviation from straight line (yellow)
redDev=0.015; %deviation from straight line (red)
flag1=0; %plot graphic
flag2=0; %plot graphic
flag3=0; %plot graphic

%% CURVATURE ANALYSIS %%
slm1=slmengine (e1 (start:end), cyy (start:end), 'degree', 3, ...
    'knots', 10, 'ConcaveUp', 'on'); %fitting curvature
e1FitSpace=linspace (e1 (start), e1 (end), N);
curvatureFit=slmeval (e1FitSpace, slm1); %eval in linspace
curvFitOriginal=slmeval (e1 (start:end), slm1); %eval in e1 space

[minVal, minIn]=min (curvatureFit); %fitting straight line
[minVal0, minIn0]=min (curvFitOriginal); %find min e1 space index
temp=find (curvatureFit >= minVal + yDev) - minIn; %find yDev
temp (temp <= 0) = [];
maxIn = min (temp + minIn); %maximum in linspace index

temp=find (curvFitOriginal >= minVal0 + yDev) - minIn0; %find yDev
temp (temp <= 0) = [];
maxIn0 = min (temp + minIn0); %maximum in e1 index

slm2=slmengine (e1 (minIn0+start:maxIn0+start), ...
    cyy (minIn0+start:maxIn0+start), 'increasing', 'on', 'degree', ...
    1, 'knots', 2, 'extrapolation', 'linear'); %s. line fitting
straightLineFit=slmeval (e1FitSpace, slm2);
maxValy=curvatureFit (maxIn);
maxValx=e1FitSpace (maxIn);

deviation=curvatureFit-straightLineFit; %deviation curvature...
    straight line
%
[greenValue, greenIndex]=min (abs (deviation (maxIn:end) - greenDev));
[yellowValue, yellowIndex]=...
    min (abs (deviation (maxIn:end) - yellowDev));
[redValue, redIndex]=min (abs (deviation (maxIn:end) - redDev));

greenIndex=greenIndex+maxIn;
yellowIndex=yellowIndex+maxIn;
redIndex=redIndex+maxIn;

%% LIMIT STRAIN %%
% e1FitSpace (greenIndex), e1FitSpace (yellowIndex) and
% e1FitSpace (redIndex) represent the e1 value for the green,
% yellow, and red dots, respectively.

```

Time-dependent method:

```
%% READ .xlsx FILE %%
% All required data from curvature method script
%% DATA AND PARAMETERS %%
N=1000; %fitting space dot;
start=round(0.1*length(e1)+1,0); %start of fitting interval
RateInt=round(0.05*length(e1),0); %number of dots used for
%the linear fit of initial and final part of the curve
tVal=0.1; %interception tolerance

% TIME-DEPENDENT METHOD ANALYSIS
slm3=slmengine(time,e1,'degree',3,'knots',20,'increasing',...
    'on'); %strain fitting
timeSpace=linspace(time(1),time(end),N);
strainFit=slmeval(timeSpace,slm3); %strain evaluation
%over timeSpace
strainRate=diff(strainFit)./diff(timeSpace); %strain rate
slm4=slmengine(timeSpace(2:end),strainRate,'degree',3,'knots',...
    20,'increasing','on','ConcaveUp','on',...
    'extrapolation','linear'); %strain rate fit
strainRateFit=slmeval(timeSpace,slm4); %strain rate eval.
%over timeSpace
slm4=slmengine(timeSpace(1:RateInt),strainRateFit(1:RateInt),...
    'increasing','on','degree',1,'knots',2,'extrapolation',...
    'linear'); %straight line fit (beginning)
SrLineFit1=slmeval(timeSpace,slm4);
slm5=slmengine(timeSpace(end-RateInt:end),...
    strainRateFit(end-RateInt:end),'increasing','on',...
    'degree',1,'knots',2,'extrapolation',...
    'linear'); %straight line fit (end)
SrLineFit2=slmeval(timeSpace,slm5);
line1=[SrLineFit1; timeSpace];
line2=[SrLineFit2; timeSpace];
temp=InterX(line1,line2); %compute interception
t=abs(timeSpace-temp(2));
t(t>=tVal)=0;
IntInd=find(t,1);
interception=[timeSpace(IntInd), strainRateFit(IntInd)];
SrLineFit2(SrLineFit2<0)=[];

%% ONSET OF LOCALIZED NECKING %%
onsetTime=round(timeSpace(IntInd),0); %analog time
onsetStrain=round(strainFit(IntInd),3); %strain
onsetStrainRate=round(strainRateFit(IntInd),3); %strain rate
```